Millimeter wave radio channel characterization and site-specific simulation for 5G systems

Mamadou Dialounké Baldé

THÈSE / UNIVERSITÉ DE RENNES 1
sous le sceau de l'Université Européenne de Bretagne

pour le grade de

DOCTEUR DE L'UNIVERSITÉ DE RENNES 1

Mention : Télécommunications et Traitement du signal

École doctorale MathSTIC

présentée par

Mamadou Dialounké BALDE

préparée à l'unité de recherche IETR-UMR CNRS 6164
Institut d'Électronique et de Télécommunications de Rennes
(département Ondes & Signaux, Équipe Propagation, Localisation)

Millimeter-wave Radio Channel Characterization and Site-Specific Simulation for 5G Systems

Soutenue à Rennes
le 19 Décembre 2017

devant le jury composé de :

Martine LIENARD
Professeur à l'Université de Lille 1 / *Présidente*
Alain SIBILLE
Professeur à Télécom ParisTech / *Rapporteur*
Rodolphe VAUZELLE
Professeur à l'Université de Poitiers / *Rapporteur*
Katsuyuki HANEDA
Associate Professor at Aalto University / *Invité*
Heykel HOUAS
Ingénieur à l'ANFR / *Invité*
Bernard UGUEN
Professeur à l'Université de Rennes 1 / *Directeur de thèse*

Ki xam meunta jëf jëfi ki xamout

Acknowledgments

Tout d'abord, je tiens à adresser mes sincères remerciements à Monsieur Bernard UGUEN pour m'avoir donné l'opportunité de réaliser cette thèse sous sa direction. Ces trois années de thèse effectuées sous sa direction sont marquées par un qualité d'encadrement exceptionnel. Il a été d'une grande disponibilité, surtout quand il s'agit de discuter de science. Il m'a initié aux problématiques du canal de propagation tout en mettant l'accent sur la rigueur scientifique. Il a su conseillé, patienter et encourager au bon moment et ceci à plusieurs reprises. Je le remercie également pour avoir était d'une humilité sans précédente et d'avoir été humainement bien dans la relation doctorant-directeur de thèse. Et Merci de m'avoir fait découvrir Python pour les sciences!

Je remercie Messieurs Alain SIBILLE Professeur à Télécom ParisTech et Rodolphe VAUZELLE Professeur à l'université de Poitiers d'avoir bien voulu accepter la charge de rapporteur.

Je tiens également à remercier Madame Martine LIENARD Professeur à l'université de lille 1, une scientifique que j'ai déjà rencontré lors du meeting du COST en 2014 à Valence (Espagne), de m'avoir fait l'honneur de présider mon jury de thèse.

Je souhaite également remercier Dr. Heykel HOUAS, expert qualifié en spectre que j'ai connu par le biais de mon directeur de thèse, d'avoir accepté de juger ces travaux de thèse en tant qu'invité.

J'exprime ma reconnaissance à Monsieur Katsuyuki HANEDA associate Professor à l'université d'Aalto, Finland. Il m'a donné la grande opportunité de visiter son prestigieux group Antennas and propagation de l'université d'Aalto pendant 6 mois. Il a mis à sa disposition les équipements de sondeurs de canal ainsi que les ressources liés aux traitements de données. J'ai été très honoré d'avoir évoluer dans cet environnement de prestige et ses discussions pointues et rigoureux ont forgé ma manière de penser scientifique. Je tiens également à remercier son groupe qui m'a acceuilli chaleureusement et aidé

dans les campagnes de mesures et également pour leur discussions de haute factures. Je pense notamment à Dr. Aki Karttunen qui a partagé son code matlab pour la détection de pics, Dr. Jan Järveläinen, Mr. Usman T. Virk , Dr. Sinh L. H. Nguyen et Mr. Sathya Venkatasubramanian, Dr. Clemens Icheln et Mme. Mirjam Lappalainen.

Je remerciement infiniment Dr. Nicolas Amiot mon collègue de bureau. Il a su à de très nombreuses fois mis à ma disponibilité sa connaissance, sa patience et son savoir faire. Développeur expérimenté en Python, il a été d'un soutien sans précédent durant cette thèse.

Je remerciement également Madame Noëlle Le Ber, secretaire du département pour sa bonne humeur, sa gentillesse, sa disponibilité et sa qualité humaine. Je remercie également les personnes que j'ai eu à cotoyer durant cette expérience et je pense notamment à Dr. Stéphan Avrillon, Dr. Laura Pometcu, Sefofo.

Un grand jarama aux membres de DEFARSCI: Dr. Ba, Dr. Barro, Dr. Diallo, Dr. Diedhiou, Dr. Fall, Dr. Fam, Soda, Saly etc.

Mes très sincères remerciements vont à l'endroit de personnes qui me sont chères: Talla Sène, Mouhamadou Moustapha Ba, Ndèye, Safietou, Bamba.

Mes remerciements vont à l'endroit de ma famille qui sont en France: tonton mamady sa femme tata Niana et leur enfants, tata Diary, Ansa et sa famille, Yéro.

Mes très sincères remerciements pieuses vont à l'endroit de mes chouyouks et amoureux de Cheikh Ibrahima NIASS (rta) qui se sont associés spirituellement à moi durant ces trois années : Cheikh Mouhamadoul Mahy Cissé et sa famille, Cheikh Baba Lamine Niass et sa famille (particulièrement Ahmadou Sarr Niass), Cheikh Abdoul Malick Niass, Cheikh Said, Cheikh Mathias, Cheikh Moussa et sa femme, Cheikh Ousmane, Madihu rassul, Cheikh Sidati, Cheikh Ahmadou Fall et toute la dahira de Rennes, Cheikh Lamine, Cheikh Ibrahima Dubois, Ando Thi BAYE.

Je remercie chaleureusement mes parents qui ne cessent de prier pour moi et qui se sont déplacés pour assister à ma soutenance. A mon père pour avoir toujours cru en moi et donner toute l'éducation nécessaire pour ma réussite, à ma mère pour son amour, sa bienveillance, sa tendresse, ses prières, à mes frères et soeurs pour leur soutien et amour et prières et à ma femme et mon fils pour leur encouragement, leur patience, leur prière, leur tendresse et leur amour.

Alhamdoulilah

Contents

Acknowledgments I

Contents V

List of Abbreviations X

List of Symbols XV

1. General Introduction 1

General Introduction 1
1.1. Context . . . 1
1.2. Contribution of the thesis . . . 3
1.3. Organization of the thesis . . . 3

2. Review and Channel Characterization 6
2.1. Background . . . 6
2.1.1. Introduction . . . 6
2.2. Propagation Mechanisms . . . 7
2.2.1. LOS . . . 7
2.2.2. Electrical Material properties . . . 7
2.2.3. Transmission Mechanism . . . 8
2.2.4. Specular Reflection Mechanism . . . 9
2.2.5. Diffraction Mechanism . . . 10
2.2.6. Diffuse Scattering Mechanism . . . 12
2.3. Channel model: Review . . . 12
2.3.1. Stochastic Channel Models . . . 14
2.3.2. Site-Specific Techniques . . . 15
2.3.2.1. Finite Difference Time Domain . . . 15
2.3.2.2. Ray Tracing . . . 15

2.3.2.3. Point Cloud . . . 16
2.3.3. Standardized models . . . 17
2.3.3.1. 3GPP models . . . 17
2.3.3.2. WINNER models . . . 17
2.3.3.3. COST 2100 model . . . 18
2.3.3.4. METIS model . . . 19
2.3.3.5. MiWEBA . . . 20
2.3.3.6. IEEE802.11ad . . . 20
2.3.3.7. NYU channel model . . . 20
2.3.3.8. QuaDRiGa . . . 21
2.3.3.9. mmMagic . . . 21
2.4. Channel Characterization . . . 22
2.4.1. Channel Transfer function and Channel Impulse Response . . . 22
2.4.2. Power Angular Delay Profile . . . 23
2.4.3. Power Angular Profile and Power Delay Profile . . . 23
2.4.4. Large Scale Parameters . . . 24
2.4.4.1. Cross-Correlation Parameters . . . 24
2.4.4.2. Path-loss Model . . . 25
2.4.5. Fine Peak Search Method . . . 25
2.4.5.1. Rician K-factor . . . 26
2.4.5.2. Delay Spread . . . 27
2.4.5.3. Omni-directional path-loss . . . 27
2.4.5.4. Angular Azimuth Spread . . . 27
2.5. Summary . . . 28

3. Channel Measurements **30**
3.1. Motivations . . . 30
3.2. Directional Channel Sounding . . . 32
3.2.1. Mm-waves Frequency Bands . . . 32
3.2.2. Synthesized Omni-directional Antenna . . . 33
3.2.3. Calibration . . . 33
3.3. Mm-wave Channel Soundings . . . 33
3.3.1. Outdoor and InH Channel Soundings in Mobility . . . 34
3.3.1.1. *Meas*.0: Outdoor Mobility . . . 34
3.3.1.2. *Meas*.1: Description of the 28 GHz Channel Sounding . . . 36
3.3.1.3. *Meas*.1: Description of the Environment . . . 37
3.3.2. InH Mobile Measurements Data Analysis . . . 38
3.3.2.1. Data Analysis . . . 38
3.3.2.2. LSP analysis . . . 41
3.3.3. Multi-frequency Conference Room Synthesized Omni-Directional . . . 42
3.3.3.1. *Meas*.2: Multi-frequency Channel Soundings . . . 42
3.3.3.2. *Meas*.2: Description of the InH Conference Room . . . 44
3.3.4. Multi-frequency Conference Room Data Analysis . . . 45

3.3.5. UMi Synthesized Omni-Directional Characterization 48
3.3.5.1. *Meas.*3: 32 GHz Channel Sounding UMi 48
3.3.5.2. *Meas.*3: Description of the UMi environment 48
3.3.5.3. UMi Data Analysis 51
3.3.6. `back-projection`: Single Bounce Geometrical Transformation . . . 53
3.3.6.1. Problem Formulation 53
3.3.6.2. `back-projection`: Results 54
3.3.6.3. Discussion 54
3.4. Summary 56

4. RT vs Measurements: Comparisons **59**
4.1. Description of the Ray Tracing Tool 59
4.1.1. The Graph-Based Approach for Ray Tracing 59
4.1.2. Layout Description 59
4.1.3. Building Graphs Associated to the Layout 61
4.1.4. Determination of Signatures 64
4.1.5. Evaluation of PM Coefficients 65
4.1.5.1. Specular Reflection and Transmission Coefficients 65
4.1.5.2. Diffraction Coefficients 66
4.1.6. Sectoral Aperture Horn Antenna Pattern: Implementation 67
4.2. RT vs *Meas.*2 71
4.2.1. RT: Conference Room Environment Description 71
4.2.2. Conference Room Simulation 72
4.3. RT vs *Meas.*3 80
4.3.1. RT: UMi Environment Description 80
4.3.2. UMi Simulation 80
4.3.3. UMi: Antenna Gains 84
4.3.3.1. *Meas.*3: LSP Analysis 85
4.4. Summary 87

5. General Conclusion **90**
5.1. Summary 90
5.2. Perspectives 93

A. Espoo UMi measurements **95**

B. Path `back-projection` **110**

Personal Contributions **123**

Bibliography **135**

Résumé en Français **138**

List of Figures **146**

List of Tables **150**

List of Abbreviations

2G	Second Generation
3G	Third Generation
3GPP	Third generation partnership project
4G	Fourth Generation
5G	Fifth Generation
AAS	Azimuth Angular Spread
ABG	alpha beta gamma
AoA	Angle of Arrival
AoD	Angle of Departure
B2B	Back-to-back
BAN	Body Area Network
BS	Base Station
CDF	Cumulative distribution function
CI	Close in
CIF	Close in floating
CIR	Channel Impulse Response
CMOS	Complementary Metal Oxyde Semiconductor
COST	European Cooperation in Science and Technology

CTF Channel Transfer Function

DS Delay Spread

eMBB enhanced Mobile Broadband

EoD Elevation of Departure

FDTD Finite-difference time-domain

FS Free Space

FSPL Free Space Path-Loss

GO Geometrical Optic

GR Ground Reflection

GSCM Geometrical Stochastic Channel Model

HPBW Half Power Beam-Width

I2O Indoor to Outdoor

IEEE Institute of Electrical and Electronics Engineers

IF Intermediate Frequency

IFBW Intermediate Frequency Bandwidth

IMT2020 International Mobile Telecommunications for 2020

InH Indoor Hotspot

IoT Internet of Things

IT Information Technology

ITU-R International Telecommunication Union Radiocommunication

KED Knife Edge Diffraction

KF rician K-factor

LO Local Oscillator

LOS Line-of-Sight

LSP Large Scale Parameter

METIS Mobile and wireless communications Enablers for the Twenty-twenty Information Society

MiWEBA millimetre-Wave Evolution for Backhaul and Access

MIMO Multiple Input Multiple Output

MS Mobile Station

mmMAGIC Millimetre-wave based mobile radio access network

mm-wave Millimeter wave

MPC Multi-path Component

NLOS Non Line-of-Sight

NYU New York University

NYUSIM New York Simulator

OSM Open Street MAP

PADP Power angular delay profile

PAS Power angular spectrum

PC Point Cloud

PDP Power delay profile

PL Path-loss

PM Propagation Mechanism

QuaDRiGa Quasi deterministic radio channel generator

RAT Radio Access Technology

RF Radio Frequency

RMa Rural Macro-cell

RMS Root Mean Square

RSPG Radio Spectrum Policy Group

RT Ray Tracing

Rx Receiver

SCM Stochastic Channel Model

SF Shadowing factor

SR Specular reflection

TCSL Time Cluster and Spatial Lobes

Tx Transmitter

TRF Transfer Response Function

UMa Urban Macro-cell

UMi Urban Micro-cell

UMTS Universal Mobile Telecommunication System

UTD Uniform Theory of Diffraction

UWB Ultra-Wide Band

VNA Vector Network Analyzer

WiFi Wireless Fidelity

WINNER Wireless world initiative new radio

WRC World Radio Communication conference

XPR cross Polarization

List of Symbols

c	Speed of light
f	Range of frequency
f_c	Central frequency
H	Channel transfer response
h	Channel impulse response
l	index of the path
L_p	Number of path
N_f	Number of frequency points
P_l	Power of the l-path
λ	Wavelength
$\delta(.)$	Dirac function
ϵ	Complex relative permittivity
ϵ'	Real part of ϵ
ϵ''	Imaginary part of ϵ
η_0	Free space impedance
σ	Standard deviation value
μ	Mean of value
σ_c	Conductivity
ϕ	Azimuth angle
α	Distance dependency exponent
n	Path loss exponent
ρ	Cross-correlation
β	Floating offset
γ	Frequency dependency
ζ	Shadowing fading variance
S_ϕ	Azimuth spread
τ	Delay
$\mathscr{F}^{-1}$	Inverse Fourier transform
Δ	Sliding window

Chapter 1

General Introduction

1.1. Context

The field of wireless cellular communication system has continuously undergone deep mutations the last two decades. The trend was first initiated by the third generation of cellular communication system (3G) deployed at the beginning of the century with the global unified system known as Universal Mobile Telecommunication System (UMTS). The purpose of the UMTS was to help the scale-up of the multimedia services on the user's side by exploiting the spectrum resource over 2 GHz. However, since the initial purpose of the first and the second generation mobile cellular communication systems was dedicated to the voice, the 3G has experimented a significant change with the emergence of smart mobile devices that scaled up the traffic of the data. This trend is maintained and stimulated tremendously with the deployment of the fourth generation cellular communication system (4G) where the global generated data by the mobile network surpassed four times the traffic of 3G [1]. Moreover, the expansion of smart devices is expected to be sustainable in the near future and this can lead to an *abusive* use of wearable devices[1] ubiquitously communicating to each other through the existing internet infrastructure, better know as the Internet of everyThing (IoT). Hence, a definition of a new and heterogeneous wireless cellular communication system that potentially satisfy the strong requirements regarding the traffic data while interconnecting IoT systems is needed to fulfill the missing requirements of the current wireless cellular systems (e.g. 3G, 4G). Indeed, the purpose is to accompany the on-going data *tsunami* caused by the apparition of new applications such as virtual reality, augmented reality that are eager in terms of data rates (more than 1 Gbps is expected in 2020 [2]) as well as providing an appropriate network infrastructure for IoT systems. These are one of the main goals for the upcoming fifth generation of wireless cellular communication known as 5G. Technically speaking, the definition of the 5G has to go through an unified normalization which provides a

[1] Including smartphones, tablets, connected watch, connected car and so forth.

technical standard framework jointly agreed between academic, industrial and government actors. Moreover, before proposing any suitable wireless cellular system, technical issues related to the deployment feasibility as well as the design of the technology need to be addressed and especially deep insights about the understanding and the characterization of the radio channel propagation is fundamental. The radio channel propagation is the physical part of the global block scheme of the telecommunication system where the signal is transferred via the environment with the help of physical entities (antennas). The signal emitted from the Tx antenna is transferred via the radio channel propagation by interacting with the environment that incorporates naturally objects as people, cars, buildings for instance. Consequently, the environment causes a distortion of the signal and therefore impacting on the quality of the link radio. Accordingly, before making the 5G a reality, many technical issues regarding the radio channel propagation need to be addressed. Many works [3, 4, 5, 6] highlighted spectrum crunch due to the deployment of many systems in sub-6 GHz (e.g. 2G, 3G, 4G, WiFi etc.) yielding a spectrum scarcity in such frequency bands. This motivates strongly operators and industries[2] to turn their attention towards new frequency bands and especially millimeter-wave (mm-wave) bands that cover frequency between 30 and 300 GHz.

The potential use of the mm-wave in the wireless cellular radio access can be seen as disruptive since mm-wave bands are already used in satellite communications for instance. In the radio channel propagation point of view, the mm-wave suffers from high losses as the signal propagates in the environment. Furthermore, the high cost regarding the power consumption constitutes a limit when dealing with mm-wave bands in the access link. Therefore, these concerns had put mm-wave bands to be not a priority for a while regarding the access link roll-out.
However, the above vision did not include the major efforts that have been done in the advancement of CMOS technologies in terms of performances, power consumption and costs during the few past years [7, 8]. Furthermore, using a high antenna gain constitute a way to compensate attenuation that suffers the mm-wave signal. On the other hand, the available amount of spectrum, as well as the vacant unlicensed bands in mm-wave, motivate operators and industrials to turn their attention toward this solution and therefore to be probably a key component of the 5G technology.

Nonetheless, exploring new frequency band implies to have a suitable channel model and the traditional channel models were not designed to support higher frequency. Moreover, since the wavelength is becoming smaller in mm-wave, the nature of the signal is strongly affected when the signal is propagating through the radio channel. Consequently, the investigation and characterization of the radio channel propagation in mm-wave bands are challenging and constitute an essential step before going toward a global standardization of the 5G technology.

[2]Including tier 1, automobile industry, equipment vendors and so forth

1.2. Contribution of the thesis

In this thesis, an especial attention is devoted toward the mm-wave bands regarding the radio channel propagation. The main contribution of the present work is summarized in the following:

1. Contribution to the investigation of the radio channel propagation at centimeter- (cm-) and mm-wave bands. These investigations are performed by using radio channel sounding techniques and cover a large set of realistic indoor (InH) and urban small cell (UMi) propagation scenarios.
2. Providing insights about the variability and the scattering environment of the mm-wave radio channel.
3. Evaluating a site-specific tool based on graph theory approach. Measurements data obtained from the measurement campaigns are used as a ground truth for parameterizing the ray-tracing (RT) tool.

1.3. Organization of the thesis

The content of the present manuscript is structured in three main chapters as follows.

First, an overview of the propagation mechanism basics is provided in chapter 2. The radio channel propagation is monitored by electromagnetism laws where a communication between the base station (BS) and the mobile station (MS) is possible w.r.t the fundamental propagation mechanisms. A literature review of some relevant measurement campaigns performed in mm-wave bands for 5G purposes is discussed in this chapter. Furthermore, the review of channel models designed for sub-6 GHz and the ongoing channel models studies are also provided. A special attention is turned toward the stochastic, deterministic and standardized models as a classification. Moreover, a spatio-temporal characterization of the radio channel through propagation metrics is provided in this chapter.

Chapter 3 deals essentially with the cm- and mm-wave radio channel sounding techniques. The radio channel sounding is a technique which consists in collecting information through the radio channel propagation. Investigating the radio channel propagation in such a way is the proper and realistic manner to provide a comprehensive measurements database framework. A detailed description of the driving methodology by using radio channel soundings is presented. In this study, four measurement campaigns, addressing the variability and the effect of the scattering environments in mm-wave bands, were performed in various representative propagation scenarios (office room, library, conference room, campus area and UMi). The measurements covered different frequency bands that are within the scope of the International Telecommunication Union Radiocommunications (ITU-R). Furthermore, a detailed analysis of the measurements data gathered during the measurement campaigns is presented.

In chapter 4, the site-specific simulation tool used in this thesis is presented. The site-specific technique considered in this work is a RT simulation platform relied on a graph-based description of the radio channel and intending to reproduce channel properties and relevant propagation mechanisms (PMs) for any kind of environments. Moreover, the evaluation of the RT tool is given in the second part of this manuscript by comparing the measured data obtained in the previous chapter to the predicted data from the RT. The comparison between the measured and simulated data is done through various spatio-temporal metrics.

Finally, chapter 5 concludes the manuscript by summarizing the main contributions of this work. In addition, some perspectives for further studies are given as recommendations.

Chapter 2

Review and Channel Characterization

2.1. Background

2.1.1. Introduction

The drastic growth of the mobile traffic was highly scaled-up by the emerging of smart devices during the recent past years. The transfer of the data traffic is driven by the radio propagation channel which is a key part of the wireless communication infrastructure. The radio channel is an object monitored by electromagnetism laws where the signal interacts with the environment which naturally incorporates various kind of object as such people, building, car, tree, road-sign, lamp-post, furniture and other electrical objects. It is well known that the radio channel has a strong influence in the system performances since the physical environment is quite complex. The transfer of the signal over the radio channel requires antennas at the transmitter (Tx) and receiver (Rx) side of the link. Depending on the nature of the environment, the signal can be emitted from the Tx to the Rx without any obstacles standing for the line-of-sight (LOS) condition. This means that a direct path exists between the Tx and the Rx antennas that propagates via the air. On the other hand, the presence of obstacles may appear between the Tx and Rx antennas. Consequently, the transmitted signal reaches the receiver by propagating across obstacles which have electrical properties. Therefore, various multi-paths propagation, different from the LOS path, occur standing for non line-of-sight (NLOS) condition. The NLOS paths present usually an attenuated power level and appear late in the delay domain.

In the multipath propagation context, the interactions between waves and objects are modeled through different PMs. A detailed description of relevant PMs and their main properties are reviewed subsequently in the following.

2.2. Propagation Mechanisms

2.2.1. LOS

First, as discussed above, without any obstruction i.e. free space condition, it exists one direct path propagating from the Tx to the Rx antenna via the air: this is identified as the LOS path. Such a path is characterized in the delay domain by the shortest and the strongest one. In that case, the amplitude of the received field depends only on the distance d between the Tx and the Rx and the frequency. By assuming G_{Tx} and G_{Rx} as the gain of the Tx and the Rx antennas respectively, Friis established the relation between the received power (P_{Rx}) and the transmitted power (P_{Tx}) at a given carrier frequency f_c (in GHz) as follows

$$P_{\mathrm{Rx}}(d,\lambda) = P_{\mathrm{Tx}} G_{\mathrm{Tx}} G_{\mathrm{Rx}} (\frac{\lambda}{4\pi d})^2, \tag{2.1}$$

where $\lambda = \frac{c}{f_c}$ is the wavelength and c is the speed of light in the vacuum.

It is worth to notice that Eq. 2.1 is only valid under the far-field assumption i.e. the region beyond the Fraunhofer distance defined as

$$d_f = \frac{2D^2}{\lambda}, \tag{2.2}$$

where D is the largest dimension of the antenna [9].

The formula in Eq. 2.1 is well known as the free-space path loss (FSPL) where the term $(\frac{\lambda}{4\pi d})^2$ refer to the free space loss. It can be deduced that the FSPL is more severe when the frequency increases as well as the link distance.

In the mm-wave context, besides the LOS mechanism, two other aspects need to be considered: the absorption by gases and the rain. These two aspects are affecting negatively the amplitude and the phase of the signal.
At sub 6 GHz band where λ is greater than 5 cm, attenuations due to atmospheric as well as rain can be neglected. However, this assumption is not valid when dealing with mm-wave bands and as agreed e.g. in Fig. 2.1, the specific attenuation due to atmospheric gases yields a loss of about 15 dB/Km at 60 GHz. The same observation is valid in the rain context where the attenuation can exceed 12 dB/Km at 60 GHz in a heavy rain [10]. Such informations potentially indicate that the mm-wave bands should be used in wireless cellular communication at short range (a couple of hundred meters) as agreed in [11].

2.2.2. Electrical Material properties

Before discussing the multipath propagation, let first introduces material properties. We assume that the material where the interaction holds is conductive and having electrical

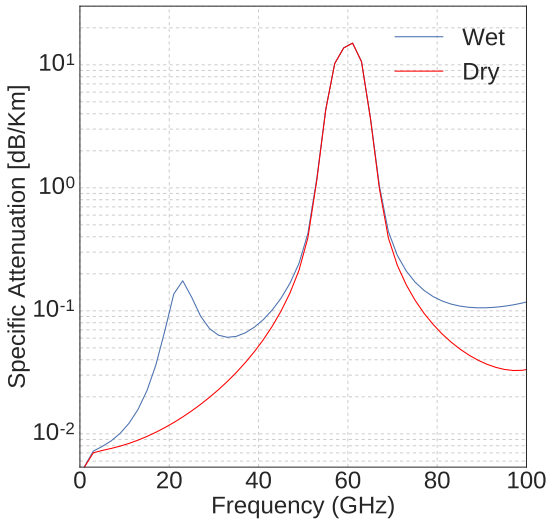

Figure 2.1.: Specific attenuation due to atmospheric gases from ITU-R P.676-11.

properties. Accordingly to the ITU-R P.2040-1 [12], the complex relative dielectric permittivity ϵ of the considered material is defined as

$$\epsilon = \epsilon' - j\epsilon'', \tag{2.3}$$

where ϵ' and ϵ'' are the real and imaginary parts defined as

$$\begin{cases} \epsilon' = \mathrm{a} f_c^{\mathrm{b}}, \\ \epsilon'' = \frac{\sigma_c}{2\pi f_c \epsilon_0}, \end{cases} \tag{2.4}$$

where ϵ_0 is the dielectric permittivity of the vacuum and $\sigma_c = \mathrm{c} f_c^{\mathrm{d}}$ is the conductivity of the material evaluated at the central frequency. a, b, c and d are constants characterizing the material. Notice that the conductivity is assumed to be frequency depended in the ITU-R P.2040-1.

2.2.3. Transmission Mechanism

The transmission mechanism results from the passage of the electromagnetic field through a material object (e.g. wall, glass) which is usually modeled as a mono or multi-layer slab.

The penetration of the path through a material implies a modification of the incident path direction w.r.t to the transmission Snell's law defined as

$$\sqrt{\epsilon_2} \sin\theta_{\mathrm{t}} = \sqrt{\epsilon_1} \sin\theta_{\mathrm{i}}, \tag{2.5}$$

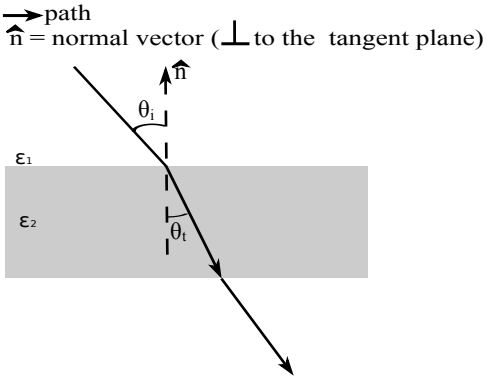

Figure 2.2.: Illustration of the transmission mechanism at the plane surface assuming a single interface.

where ϵ_1 and ϵ_2 are the complex relative permittivity of the medium 1 and 2 respectively and θ_i and θ_t are the incidence and the transmitted angles respectively. Fig 2.2 illustrates the transmission mechanism of a plane wave occurring on a plane surface. When the transmission mechanism occurs, the structure of the path is affected in a way that the phase is changed and the amplitude is attenuated accordingly to the transmission transversal electric (T_TE) and transmission transversal magnetic (T_TE) coefficients defined as

$$T_\mathrm{TE} = \frac{2\sqrt{\epsilon_1}\cos\theta_\mathrm{i}}{\sqrt{\epsilon_1}\cos\theta_\mathrm{i} + \sqrt{\epsilon_2}\cos\theta_\mathrm{t}}, T_\mathrm{TM} = \frac{2\sqrt{\epsilon_1}\cos\theta_\mathrm{i}}{\sqrt{\epsilon_2}\cos\theta_\mathrm{i} + \sqrt{\epsilon_1}\cos\theta_\mathrm{t}}. \tag{2.6}$$

Typically, the transmission mechanism is important since it gives information about the penetration loss of building materials that occurs often in practice for instance when the MS is located in InH and the BS is deployed in outdoor (indoor to outdoor (I2O) scenario).

2.2.4. Specular Reflection Mechanism

The specular reflection arises usually when the path interacts with smooth and large objects compared to λ. At the surface of the interaction, the path is reflected according to the Snell's law of reflection defined as

$$\theta_\mathrm{r} = \theta_\mathrm{i}. \tag{2.7}$$

Worthy mentioning that Eq. 2.7 is satisfied when considering a smooth surface as illustrated in Fig. 2.3. In the electromagnetism point of view, the path that experiments a specular reflection is characterized by the reflected transversal electric and magnetic coefficients (R_TE, R_TM respectively) expressed as

$$R_\mathrm{TE} = \frac{\sqrt{\epsilon_1}\cos\theta_\mathrm{i} - \sqrt{\epsilon_2}\cos\theta_\mathrm{t}}{\sqrt{\epsilon_1}\cos\theta_\mathrm{i} + \sqrt{\epsilon_2}\cos\theta_\mathrm{t}}, R_\mathrm{TM} = \frac{\sqrt{\epsilon_2}\cos\theta_\mathrm{i} - \sqrt{\epsilon_1}\cos\theta_\mathrm{t}}{\sqrt{\epsilon_2}\cos\theta_\mathrm{i} + \sqrt{\epsilon_1}\cos\theta_\mathrm{t}}. \tag{2.8}$$

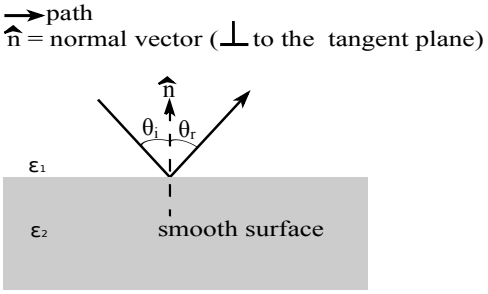

Figure 2.3.: Illustration of the specular reflection mechanism appearing on a single interface.

2.2.5. Diffraction Mechanism

The diffraction mechanism compensates geometrical optic discontinuities. Accordingly to the Huygens principle that considers each point of the wave-front as a source of secondary wavelets [9]. The paths are radiated around the area where the interaction held: paths appearing under the incidence shadow boundaries stand for diffracted paths. Usually, the diffraction mechanism is expected to appear on the corner edge of objects e.g. as illustrated in Fig. 2.4.

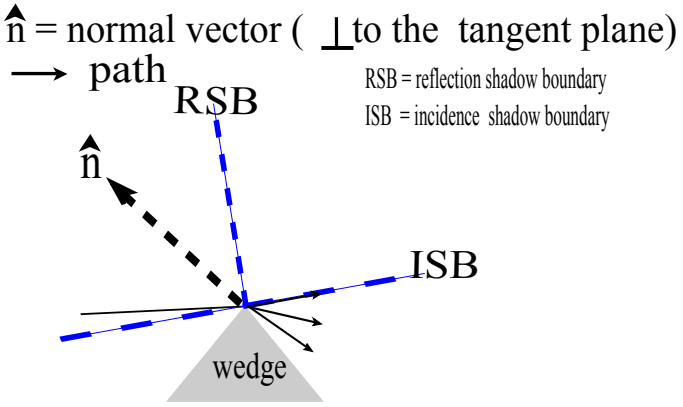

Figure 2.4.: Example of a diffraction mechanism over a wedge.

Commonly, the diffracted mechanism can be modeled by using the uniform theory of diffraction (UTD) [13] which is a generalization of the geometric optics. In practice, some projects e.g. the METIS project [14] and the 3GPP TR38.900 [15] implemented the diffraction mechanism (in indoor and outdoor cases) by following the UTD approach.

For urban UMi environment, Berg's model [16] can be used in a way that the model considers the street corner as a secondary source [14, 17] by assuming paths are propagating around the street corner and therefore ensure the continuity of the signal. Practically, since BSs are deployed over the rooftop of buildings and users are operating below rooftop, the propagation through roof-tops and street corner are generally modeled by the

diffraction mechanism. Hence, realistic prediction of path loss in UMi scenario requires integrating such a PM. However, those situations are expected to be less important in millimeter wave situation where LOS condition is always sought for.

Besides, the knife edge diffraction (KED) model can be used to model the shadowing or the blocking caused by humans. For instance, the 3GPP TR38.900 [15] and the METIS project [14] are using the KED to model the blocking objects. Fig. 2.5 illustrates an example of a blocking object modeled by the KED.

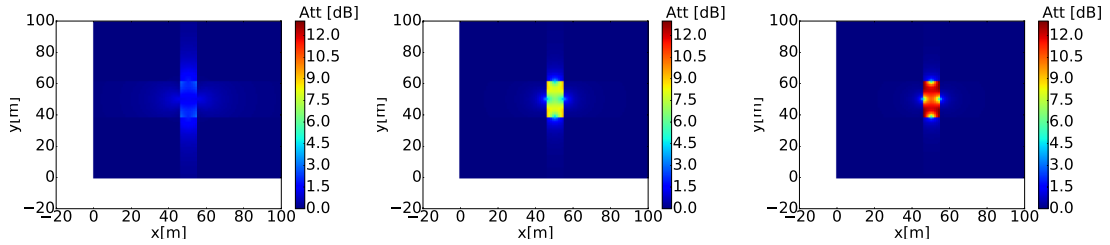

(a) Shadowing at 2.4 GHz (b) Shadowing at 28 GHz (c) Shadowing at 83 GHz

Figure 2.5.: METIS KED blockage model: blockage due to the shadowing effect.

The blockage effect displayed in Fig. 2.5 is implemented from the formula Eq. 6.5 of the METIS project [14] that assumes a simple shadowing screen. The considered screen in Fig. 2.5 is assumed to be a rectangular screen with a height of 0.75 m and a width of 0.3 m and placed in the middle of the Tx and Rx link. It can be observed that the effect of the shadowing modeled by the KED is more pronounced in higher frequency reaching an attenuation of 13 dB at 83 GHz compared to the frequency band of 2.4 GHz where the maximum attenuation is less than 3 dB.

Regarding the literature, plenty works reported the diffraction mechanism through measurement. For instance, works in [18, 19] with an interest of indoor scenario claimed the meaningless of the diffraction mechanism in mm-wave compared to the LOS and the specular reflection PMs. Moreover, works carried-out in indoor scenario [14, 20] demonstrated through measurement performed at 60 GHz the weakness of the diffraction mechanism in NLOS condition due to the corner edge with 15 dB of attenuation. However, authors in [20] claimed the dominance of the ceiling diffraction in a vertical plane when the link distance is becoming higher in indoor scenario. Furthermore, work performed in outdoor environment in mm-wave [21] suggested that the communication between the BS and the MS can be achieved by multipath propagation through diffraction mechanism for instance.

The general trend in the literature w.r.t measurements tends to converge that the diffraction mechanism is observed to be weak in mm-wave frequency bands.

2.2.6. Diffuse Scattering Mechanism

As illustrated in Fig. 2.6, when the incoming path interacts with a rough surface, the path is spread in all directions with different angles: paths that do not follow the specular direction stand for diffuse scattering. Explicitly, the amount of energy does not come from one single impact point but from multiple scattered points from the surface of the interaction.

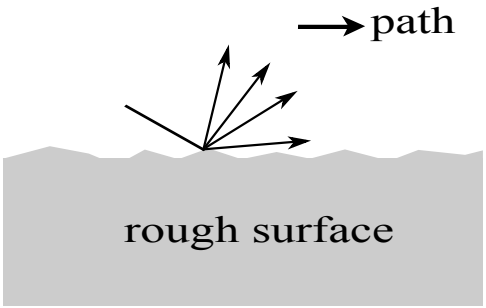

Figure 2.6.: 2D view of the diffuse scattering mechanism illustration appearing over a rough surface.

Practically, on the received signal side, the diffuse scattering mechanism can be seen as the residual component from the specular components that have been removed while the noise floor is being assumed lower. Such mechanisms are considered as non coherent compared to the specular reflection and characterized in the delay domain by a weaker and delayed power reaching the Rx [22, 23]. Furthermore, the diffuse scattering might present a long tail shape in delay domain and the appearance of such a mechanism can cause a depolarization of the field and consequently yielding a degradation of the link performance.

A non-exhaustive literature survey highlighting PMs in mm-wave bands is reported in Table 2.1 showing a scope of some measurement campaigns performed in realistic propagation scenarios. A general finding would be that PMs are evident in mm-wave bands and a frequency dependence of PMs w.r.t buildings materials is noticed.

2.3. Channel model: Review

Since the radio channel is stochastic by nature, it would be useful to have a tool that reproduces the reality of the channel as well as evaluating the performance system of the network: these are the main goal of a channel model. Usually, channel models are simulation tools aiming to reproduce physical properties of the radio channel in an accurate manner. In the literature, plenty of approaches were suggested and hereafter, an overview of physical channel models with a focus on stochastic, deterministic and

Table 2.1.: Literature survey of mm-wave measurement campaigns addressing PMs studies (transmission (Trans.), specular reflection (SR), diffraction (Diff.) and diffuse scattering (Scat.)).

PMs	Team	Scen.	Freq. (GHz)	Findings	Ref.
Trans.	Orange Labs	O2I	3, 10, 17, 60	Strong dependency between penetration losses and window material position.	[24]
Trans.	Ericsson	O2I	2.44, 5.8, 14.8, 58.68	Building penetration losses can reach 45 dB at 58.68 GHz.	[25]
Trans.	Rohde & Schwarz	O2I	17	Penetration losses are depending on material and severe in high frequency.	[26]
Trans.	NYU	InH,Out.	28 GHz	A brick penetration loss thorough a pillar can reach 28.3 dB in a densely urban environment.	[27]
Trans.	NYU	InH	73 GHz	Cross- and Co-polarized configurations exhibited the same losses for most materials	[28]
SR	NYU	UMi,UMa	28, 38, 60, 73	Specular reflections are dominant and lead mostly the propagation paths in NLOS case.	[29, 30, 31, 21, 27]
SR	Aalborg	InH	3, 15, 29 GHz	The specular reflections are dominant compared to the diffuse scattering.	[32]
Diff.	Aalborg	Out.,O2I	38	Diffracted paths exist but are attenuated rapidly with the increasing of the NLOS distances.	[33]
Diff.	NYU	InH	60 GHz	A ceil diffraction holding in vertical plane is found to be dominant when the Tx is far away from the Rx.	[20]
Diff.	NYU	Out.	-	A communication between the BS and the MS can be achieved by diffraction mechanism.	[21].
Scat.	NYU	UMi,UMa	-	The diffuse scattering might be predominant in mm-wave (specially at 73 GHz).	[30, 34, 29]
Scat.	Keysight	InH,Out.	60 GHz	Diffuse components exists.	[26, 35]
Scat.	Aalto	InH	60, 70 GHz	Higher losses from specular and diffuse components are observed at 70 GHz.	[36]
Scat.	NYU	InH & Out.	60 GHz	The diffuse scattering from lamp-posts, cars, is found to be dominant compared to the corner diffraction in Out. In addition, in InH scenario, the dominant contribution originated by the diffuse scattering mechanism is recorded in the horizontal plane.	[20, 37]

standardized models is provided.

2.3.1. Stochastic Channel Models

By stochastic channel model (SCM), it is stated that channel properties are determined in a stochastic manner in a way that scatterers and the realization of the set of channel impulse responses (CIRs) with statistical distributions are generated randomly. The starting point is the drive of large and various measurement campaigns that serve as a source for deriving parameters. Accordingly, evolving in such an approach allows reproducing relevant channel features accurately while keeping larger the number of realizations. Many efforts have been made for deriving SCMs in mm-wave bands. For instance, work in [38] carried out measurement campaigns in two hospital environments for real-time video streaming and ultrasonic imaging applications at 60 GHz. Authors proposed SCMs that were able to reproduce power delay profiles (PDPs) including both specular and diffuse components while angular characteristics were not considered. Another work performed at the same frequency band in a conference room including angular characteristics is presented in [39]. Authors derived a channel model by proposing an extension of the Saleh-Valenzuela model. Paper in [40] proposed a 3D mm-wave SCM aiming to reproduce CIR and 3D power angular spectra. The work is based on an extensive measurement campaign performed in New York City from 2011 to 2015 at 28, 38 and 73 GHz and temporal and spatial channel parameters were derived from measurements. The 3D SCM covers LOS and NLOS conditions and CIRs are modeled independently. Furthermore, the model supports arbitrary carrier frequency, antennas, polarization effects. Cross-polarization (XPR) is taken account and modeled as a Gaussian log-normal distribution.
Nonetheless in the SCM, an interest of preference resides in covering a large set of environments (flexibility) while keeping lower computational costs. Such a concern is overcame by the geometry-based stochastic channel model (GSCM) which can be seen as a combination of the deterministic and the stochastic approaches. The key idea is to describe the environment geometrically while scatterers referred with statistical distributions are stochastically positioned and channel properties are derived from such a configuration [41]. Regarding the literature, major efforts have been made to develop such a framework and plenty of models are following the stochastic methodology.

Besides, another category of a stochastic method based on propagation graph theory was proposed in [42]. The principle of the model is based on formulating the propagation environment by using a set of propagation graphs. Antennas and scatterers state for vertices and edges denote visibilities (multi-paths) between vertices. From that, edges are generated w.r.t the edge-occurrence probability and the edge transfer functions are computed. The CIR is obtained via inverse discrete Fourier transform. Such a procedure offers a flexible tool and dominant PMs are reproduced as well as the reverberation effect. Furthermore, such an approach offers an infinite number of bounces while keeping lower the computation cost. In addition, the model includes multiple input multiple output (MIMO) techniques as well as multi-link channels. However, channel characteristics such as polarization and moving scatterers are not included in the model to date. Further

stochastic channel model based on propagation graphs can be found in [23, 43, 44, 45, 46].

2.3.2. Site-Specific Techniques

In contrast to the SCM, there is the site-specific technique which follows a deterministic approach in a sense that environments are described deterministically by providing geographical footprint databases description of the environment and path interactions are calculated following the electromagnetism theory. The specification related to antennas are mentioned (e.g. frequency, bandwidth, polarization) and PMs, material properties and environment of interest can be controlled. Such techniques provide a direct access to the spatio-temporal characteristic of the radio channel since the environment and path interactions are under control. The pattern of antennas are implemented separately and can be embedded in the radio channel. An accurate deterministic channel model can be achieved with a detailed description of the environment as well as a good optimization w.r.t the material parameters. However, achieving such an accuracy is very cost regarding the computation time and memory. In mm-wave for instance where λ is small, the radio channel frequency is potentially subjected to the influence of any small objects. Therefore, the description of such an environment needs to incorporate small objects that are usually neglected in the sub 6-GHz. Omitting such kind of details may decrease the reliability of the site-specific techniques. As an application, deterministic techniques are preferred for prediction and coverage network purposes[47]. The next subsections provide more detail about the most encountered site-specific techniques.

2.3.2.1. Finite Difference Time Domain

The finite difference time domain (FDTD) is a method enabling to access a complete mapping of the electromagnetic field at all points of the propagation environment. The FDTD is a numerical technique modeling the electric and magnetic fields w.r.t Maxwell's equations. Many works addressing ultra-wide band (UWB) and body area network (BAN) purposes in indoor and sub-band 6 GHz are following the FDTD approach [48, 49, 50, 51]. Nonetheless, the FDTD method is facing to the high computational cost since the method is based on solving Maxwell's equations with building geometry as boundary conditions. Consequently, when going in a more complex propagation environment and addressing higher frequency band (where λ is smaller), the FDTD techniques become computational cost and might lead to a numerical instability.

2.3.2.2. Ray Tracing

In contrast to the exact method reviewed previously, the RT is a technique that models the radio channel relying on the image principal. The RT searches the propagation paths by assuming optical rays from the Tx to the Rx. Each scatterer of the propagation environment (e.g. wall, building, urban furniture and so forth) is described in detail and subsequently, a database is created incorporating materials associated with their electrical properties. Usually, convenient tools such as Google Earth [52], Open Street Map (OSM)

[53] or laser scanning technique exist for describing the propagation environments. After describing the propagation environment, all the potential and finite rays going from the Tx to the Rx are determined. The calculation of the propagation loss characteristics is performed for each path including polarization, delay and angular characteristics.
Majors efforts have been made in the last two decades for the development of ray tracing tools using various approaches. For instance, references [54, 55, 40, 56] presented a 3D RT based on image ray tracing approach and calibrated with measurements performed in InH and UMi environments at mm-wave bands. Works reported in [57, 58] proposed a RT tool based on propagation graphs.

However, RT techniques suffer from the heavy computational, especially when including diffuse scattering for instance. Furthermore, when targeting mm-wave channel propagation, small objects such as lamp-posts, road-signs and other metallic objects cannot be neglected. In addition, a rough approximation of material properties may provoke an under- or over-estimation of the RT prediction as agreed in [59].

2.3.2.3. Point Cloud

Another site-specific technique that gained increasing in consideration is the laser point cloud technique. The point cloud technique describes in an accurate and detailed way the environment by using a laser scanner technique. The principle is based on projecting the laser beam through the radio propagation environment from different locations. From that, each point of the point cloud can be seen as scatterers and paths can interact with them via PMs. The distance and the intensity of the backscattering laser are calculated and each reflection point of the radio propagation environment is stored as a set of point stated as a point cloud. The radio channel is evaluated as a combination of multi-path propagation. Such a methodology gives a representation of the radio propagation environment in 3D by capturing the roughness of objects with an accuracy of about millimeter [60]. Such an accuracy depends on the density of the point cloud and the denser the point cloud, the higher the accuracy. In addition, such an accuracy is suited when dealing for instance with dense multipath components caused by scattering in mm-wave bands. Works reported in [61, 62] proposed an indoor channel model at 60 GHz based on point cloud simulations and predictions show remarkable agreements w.r.t measurements. In addition, the proposed channel model incorporates classical PMs including the diffuse scattering and material parameters are optimized to fit with measurements. Another work presented in [63] proposed a specular reflection model based on point cloud technique and the parameterization of the model is performed over the reflection coefficient based on measurements.

Notwithstanding, the underestimation of the point cloud densities can yield an instability of the radio channel characteristics and sometimes can lead to a miss of PMs as discussed in [64]. Furthermore, as for the RT technique, the point cloud prediction tool is facing to the computation complexity as points are increasing.

2.3.3. Standardized models

So far, the purpose of channel model tools was to reproduce essential features of the radio channel in a realistic way. Such a definition and development frameworks are performed through standardized models. Converging toward standardized channel models is appreciated since efforts can be mutualized and channel models can serve as a public framework for system level simulations for instance. Many efforts have been made to propose standardized channel models validated through measurements and incorporating deterministic and stochastic approaches or a combination of both (hybrid approaches). Suitable standardized channel models that have been elaborated through projects are discussed next.

2.3.3.1. 3GPP models

The 3^{rd} Generation Partnership Project (3GPP) is an organization partner aiming to develop a public standard channel model for the need of cellular system evolution. Over the last two decades, the 3GPP has accompanied the deployment of cellular systems by proposing specifications and methodology for channel modeling through releases. Several channel models elaborated in sub-6 GHz band were conducted through the 3GPP. The 3GPP SCM [65] initially proposed in 2002 and incorporating MIMO systems is a 2D structure based on modeling scatterers stochastically. The design of the model is restricted for narrowband (5 MHz of bandwidth) at 2 GHz frequency band while covering outdoor scenarios (UMi, urban macro-cell (UMa) and sub-UMa scenarios). The channel is assumed constant over the single run snapshot and channel parameters are randomly generated. Such procedure is known as the *drop* concept introduced in the 3GPP SCM [66]. Several drops can be generated independently and the geometry of the environment, antennas structure, clusters, BSs and MSs are assigned in 2D. Therefore, channel properties including azimuth angular are generated independently and the spatial consistency of parameters is conserved making the model simple and computational costless. Standard as IEEE 802.20 dedicated for mobile broadband wireless access for instance and working for frequency band below 3.5 GHz has adopted the 3GPP SCM. However, the miss of elevation angle constitutes a lack and such issues are fulfilled in the 3GPP TR36.873 [67]. This latter feature is important to be considered in the 5G context for instance since for technology such as massive MIMO, it is expected that the BS allocates resources to several UEs at the same time by beamforming the signal in azimuth and elevation directions. This can be achieved by the use of an antenna array. Besides, the recent release of the 3GPP proposed in [15] includes important features such as spatial consistency, human blockage at mm-wave bands.

2.3.3.2. WINNER models

The channel models developed by the Wireless World Initiative for New Radio (WINNER) (WINNER I [68], WINNER II [69], WINNER + [70]) for beyond 3G systems are channel models based on GSCM approach and derived from the 3GPP SCM for link and

system simulation purposes. The double directional of the radio channel is conserved and the spatio-temporal channel parameters, as well as scattering objects, are determined stochastically from the map w.r.t their distributions. Therefore, contributions of multi-path components (MPCs) originated from PMs are summed yielding the channel realizations. In contrast to the 3GPP SCM, the WINNER model supports large propagation environments and scenarios while reproducing small and large-scale fading effects through frequency band ranged from 2 to 6 GHz with a bandwidth up to 100 MHz. The WINNER channel models are quite used and for instance, the MIMO framework in the 4G system is developed within the WINNER [71]. However, WINNER models are facing with some issues. As an example, despite the fact that geometric parameters are modeled in a stochastic way, WINNER models assume an ideal plane wave for simplicity as agreed in [72]. Regarding the 5G system, such assumption can be obsolete in the context of massive MIMO where the plane wave assumption is a concern as claimed in [73]. Furthermore, the approaches in WINNER models do not support mobility of device to device (D2D) links since the *drop* concept is applied meaning the channel parameters of two close links are independent. Therefore, multi-user MIMO in dense scenarios deployment with coexistence links and spatial consistency are not considered in WINNER models to date [74].

2.3.3.3. COST 2100 model

The COST 2100 model [75] is proposed through the European Cooperation in Science and Technology (COST) framework. The COST 2100 is a 3D channel model which relies on a GSCM and aiming to reproduce stochastic properties of distributed MIMO system: the BS containing multiple antenna is static while MS antennas can be in mobility situations. MPCs have spatio-temporal characteristics (e.g. delay, angle of departure (AoD), angle of arrival (AoA) and so forth) and those MPCs that have similar properties are grouping toward clusters. The general structure of the COST 2100 model is composed of three kinds of clusters expressly local, single bounce and multiple clusters. A visibility region concept is introduced stating for a region where the cluster is seeing the MS and as the MS is moving outside the visible region, the cluster can be turned off as explained in [75]. Since local clusters are located around antennas, those later are always visible while the single and multiple bounces are subjected to the visibility region. Assigning a visibility region uniformly to clusters that have static positions enable emulating the reality of the channel in a realistic manner and the time-varying of channel properties are reproduced by moving the MS while keeping the model sophisticated [22]. Various propagation scenarios are targeted in the COST 2100 model and frequency bands up to 5 GHz are covered.
Since the MS can be in mobility, the fixed position of the BS leads to a miss of the dual link mobility in the COST 2100 model. Moreover, the parameterization of clusters in the model constitutes another issue since the identification of clusters from measurements is not straightforward. Authors [76] presented the parameterization of the COST 2100 MIMO channel model but the work is restricted to indoor scenarios. Furthermore, authors in [77] performed a parameterization of the COST 2100 model through a meas-

urement campaign in an outdoor environment at 300 MHz and they suggested some modifications of the channel parameter distributions. Therefore, efforts need to be done in such a way to achieve a complete parameterization of the COST 2100 model.

2.3.3.4. METIS model

The Mobile and wireless communications Enablers for the Twenty-twenty Information Society (METIS) project started in 2012 for a duration of two years is run through the 7^{th} European framework programme by federating global tier 1 manufactures, operators and academics. The METIS project aims to provide realistic and relevant channel model for 5G purposes by supporting large requirements such as wide frequency bands, large bandwidth, large antenna arrays, full dual mobility, spatial consistency links for instance as detailed in [14]. A total of five scenarios and twelve test cases were selected from the end user perspective. Basically, the METIS channel model incorporates the METIS map-based model, the METIS stochastic model, and the METIS hybrid model. First, the METIS map-based model is following the ray tracing approach by using a simplified 3D description of the environment. The environment does not need accurate description in order to keep the map simple as possible and buildings and walls are modeled as rectangular uniform surfaces. Moreover, scattered objects are set randomly with a certain density. The METIS map-based model introduced a generic map namely Madrid-grid that is considered as representative of various scenarios. In contrast to the Manhattan map which is commonly used and presenting homogeneous urban environment, the environment considered in the Madrid-grid is an urban environment with relatively flat and inhomogeneous building heights. Streets present a regulated spacing and open squares are present in the Madrid-grid and therefore being more close to the reality. Physical effects, as well as large and small-scale propagation effects, are computed in a deterministic way. PMs are incorporated and diffuse scattering is taking account by dividing building surfaces into tiles and each center of tiles can yield a diffuse scattering mechanism. One benefit with this channel model is that not all propagation scenarios have to be validated and only physical PMs need to be validated as claimed in [78]. In this context, authors in [79] proposed a validation of the METIS map-based model in indoor scenario through measurements by validating significant paths originated from LOS, specular reflection, diffraction, and diffuse scattering mechanism while considering LOS, obstructed LOS (OLOS) and NLOS conditions.
The second channel model developed in the METIS project is the METIS stochastic model based on the GSCM approach where statistical parameters are derived from measurements. The METIS stochastic model adopts the WINNER modeling but the model does not cover the full frequency band above 6 GHz. The third channel model proposed in the METIS project is a combination of the map-based and stochastic models is proposed in the METIS project stating for the METIS hybrid model. As highlighted in [14], the path-loss (PL) and shadowing are computed in a deterministic way while scattering objects are generated stochastically.

However, so far, small efforts are noticed in the validation of the METIS models against measurements and therefore constituting a drawback as highlighted in [80].

2.3.3.5. MiWEBA

The Millimetre-Wave Evolution for Backhaul and Access (MiWEBA) model is a 3D quasi-deterministic channel model developed mainly for backhaul links at 60 GHz [81]. The quasi-deterministic nature of the MiWEBA channel model is due to the fact that the channel model combines deterministic and random rays. Since the channel model is developed for broadband small cell backhaul system evolving at 60 GHz, the MiWEBA model assumes the channel as a combination of deterministic rays (originated from dominant paths such as LOS, specular reflection) and random rays from other PMs. Therefore, deterministic rays are computed from the geometry of the environment while random rays are generated randomly from random scatterers. Such rays have a statistical distribution following a Poisson process with an exponential decaying profile. The MiWEBA channel model covers three scenarios: open-area, street canyon, and hotel lobby. Several measurement campaigns were performed through the MiWEBA project and some of them are reported in [82, 83, 84]. Since the MiWEBA channel model is developed for link system at 60 GHz, it is not suitable for other frequency bands. Moreover, the open-area scenario considered in the MiWEBA doesn't include surrounding walls.

2.3.3.6. IEEE802.11ad

Another standardized model designed for unlicensed band 60 GHz for local area network (LAN) and a high-speed system is the IEEE 802.11*ad* channel model [85]. The model was proposed by the group task AD of the IEEE 802.11 by covering channel modeling scenarios such as conference room, enterprise cubicle, and living room. The channel modeling approach proposed in the IEEE 802.11*ad* is a combination of a ray tracing and statistical modeling techniques as agreed in [86, 87]. Rays arriving closely and spaced in time and angular domain are grouped in a cluster w.r.t the excess delay and the power distribution. As stated in [86], five type of clusters with a number ranging from 1 to 8 were considered for the conference room: the LOS, the first order reflections from walls, the second order reflections from two walls the first order reflection from ceiling and the second order reflections from walls and ceiling . The IEEE 802.11*ad* is enabled to capture the spatio-temporal characteristics of the radio channel and features as beamforming (including steerable directional antennas) and polarization are incorporated. Moreover, The effect of motion people creating a time-dependence of the channel variation is incorporated and the CIR is provided as an output for the channel model. However, the IEEE 802.11*ad* channel model is only valid for the specified use case scenarios and does not support MIMO systems.

2.3.3.7. NYU channel model

The New York University (NYU) is one of the pioneers in the lead of measurement campaigns in mm-wave at the beginning of the decade for 5G radio channel purposes. The NYU simulator (NYUSIM) [88] is a statistical channel model based on extensive directional measurement campaigns covering frequency bands ranging from 0.5 to 73 GHz

and RF bandwidths up to 800 MHz. Both InH and outdoor scenarios including UMi, UMa, rural micro-cell (RMa) are covered. The NYUSIM channel models incorporate PL model, time cluster and spatial lobes (TCSL) for modeling CIRs w.r.t the angular directions and as an output realistic temporal and spatial CIR are generated. Regarding the PL model, NYU has published many works based on measurement campaigns where they suggested to use the 1 m space close-in (CI) / CI frequency (CIF) reference to approximate accurately the PL instead of the traditional α,β,γ (ABG) PL model [89, 90, 34, 91, 92, 93]. For instance in [90], they claimed that the proper choice of the PL model in an urban macro-cell (UMa) scenario is the CI/CIF model that exhibits small and stable shadowing factor compared to the ABG model. Such observation is highlighted in [94] where authors demonstrated that using the ABG PL model outside the scenario of interests can lead to a lack of robustness and to a higher shadowing fading standard deviation compared to the CI PL model.

2.3.3.8. QuaDRiGa

The Quasi Deterministic Radio Channel Generator (QuaDRiGa) [95] developed by the Fraunhofer Heinrich Hertz Institute is a 3D GSCM channel model based on the WINNER models aiming for modeling MIMO radio channels. Carrier frequency bands from 0.5 GHz up to 100 GHz and bandwidth of 100 MHz are covering. Features such as scattering clusters, 3D antenna modeling as well as transitions between varying propagation scenarios are provided while terrestrial and satellite scenarios are covered. The exact description of the environment is not necessary and scatterers are distributed stochastically. Typically, the QuaDRiGa channel model assumes 8 to up to 20 clusters for a given scenario. Spatial parameters of the radio channel (e.g. AoA, AoD) are derived from each path and a continuous time evolution of the channel coefficients is satisfied. The polarization is calculated following the geometric approach (geometric polarization) and the spatial correlation of the channel properties is derived from the map since two close MSs are assumed to experiment similar propagation conditions.

2.3.3.9. mmMagic

The Millimetre-Wave Based Mobile Radio Access Network for Fifth Generation Integrated Communications (mmMagic) channel model [26] is developed through the work package 2 of the mmMagic project and aiming to develop channel model for mobile radio access technology (RAT) at frequency band above 6 GHz. The channel modeling approach in the mmMagic is relied on the 3D GSCM by following the 3GPP-3D and the QuaDRiGa approaches where relevant channel properties are captured. Propagations paths are fully generated in a stochastic way while scattering clusters are based on large scale parameters (LSPs) and depending on the location, the MIMO CIRs per user link are generated as an output. The LSPs are assumed to follow the log-normal distribution. Modeling features such as single ground reflection is modeled following the delay, power, departure and arrival angles and polarization. Furthermore, the spatial consistency is guaranteed in the mmMagic channel model. Moreover, an enhancement of the simplified

blockage model existing in the METIS channel models is proposed in the mmMagic based on a two dimensional KED by taking account the fast fading when summing the complex amplitude of paths diffracted by the edges of the rectangular screen. Eight propagation scenarios including both InH and outdoor scenarios are covered in the mmMagic channel model and around twenty measurements campaigns were performed. The significant efforts realized in conducting measurement campaigns in mmMagic project are provided in [96].

2.4. Channel Characterization

2.4.1. Channel Transfer function and Channel Impulse Response

First, we consider a time-invariant radio channel. We assume an omni-directional antenna at the Tx side and a directional horn antenna at the Rx side rotated over the azimuth plane[1], corresponding to one of the practical setup that we have considered in our measurement campaigns that will be present in the next chapter. Let $\mathbf{h}_f^i$ be the channel transfer function (CTF) over the addressed frequency band of bandwidth W obtained by pointing the horn antenna in the direction ϕ_i where i refers to the index of the azimuth rotation angle. Assuming a finite number paths ($1 \leq l \leq L_\mathrm{p}$ with L_p the maximum number of paths) in the radio channel, a simplified expression (without the polarization) of $\mathbf{h}_f^i$ including the scalar effect of the horn antenna for each path l can be given as

$$\mathbf{h}_f^i = \sum_{l}^{L_p} \sqrt{G(\phi_l - \phi_i)}\alpha_l e^{-2j\pi f \tau_l}, \tag{2.9}$$

$$\mathbf{h}_f^i = [h_0^i, ..., h_{Nf-1}^i], \tag{2.10}$$

where N_f denotes the number of frequency points and $G(.)$ is the horn antenna gain weighting the energy of the path coming from the direction ϕ_i. α_l and τ_l denote respectively the complex amplitude and the delay of the lth-path. The collection of the CTF obtained from a large set of azimuth directions and an addressed band is a $N_a \times N_f$ complex matrix $\mathbf{H}_f$ expressed as

$$\mathbf{H}_f = \begin{bmatrix} \mathbf{h}_f^0 \\ ... \\ \mathbf{h}_f^i \\ ... \\ \mathbf{h}_f^{Na-1} \end{bmatrix}, \tag{2.11}$$

where N_a denotes the number of discrete angular acquisitions. $\mathbf{H}_f$ is the stacking of each acquisition in the frequency and angular domain.

[1]Since a horn antenna is used in mm-wave bands, rotating the horn antenna over the azimuth plane enables to capture the signal arriving from the all azimuth direction. Refer to section 3.2.2 for further details.

From Eq. 2.9, the expression of the CIR in the delay domain for the ith pointing angle without applying a windowing is given as

$$\mathbf{h}_{\tau}^{i} = \mathcal{F}^{-1}[\mathbf{h}_{f}^{i}] = \sum_{l}^{L_p} \sqrt{G(\phi_l - \phi_i)}\alpha_l \text{sinc}[\text{W}(\tau - \tau_l)], \tag{2.12}$$

where sinc[.] is the cardinal sine function. Equivalently, the expression of Eq. 2.11 in the delay domain is expressed as

$$\mathbf{H}_{\tau} = \begin{bmatrix} \mathbf{h}_{\tau}^{0} \\ ... \\ \mathbf{h}_{\tau}^{i} \\ ... \\ \mathbf{h}_{\tau}^{Na-1} \end{bmatrix}. \tag{2.13}$$

2.4.2. Power Angular Delay Profile

The power angular delay profile (PADP) is defined as the squared magnitude of the CIR as follows

$$\mathbf{PADP}_{\tau}[i,k] = |\mathbf{H}_{\tau}|^2 = \begin{bmatrix} |\mathbf{h}_{\tau}^{0}|^2 \\ ... \\ |\mathbf{h}_{\tau}^{i}|^2 \\ ... \\ |\mathbf{h}_{\tau}^{Na-1}|^2 \end{bmatrix}, \tag{2.14}$$

where integer index i and k are refering to angle (row) and delay (column), with:

$$|\mathbf{h}_{\tau}^{i}|^2 = \sum_{l}^{L_p} G(\phi_l - \phi_i)\alpha_l^2 \text{sinc}^2[\text{W}(\tau - \tau_l)]. \tag{2.15}$$

As it can be observed from Eq. 2.15, applying a squared magnitude of the CIR provides an information about the power that arrives from a specific angle and delay.

2.4.3. Power Angular Profile and Power Delay Profile

The power angular profile (PAP) refers to the integrated power (over the frequency) of the PADP that arrives for a given angle. It can be defined as in [97]

$$\mathbf{PAP}_{\phi}[i] = \sum_{k} \mathbf{PADP}_{\tau}[i,k]. \tag{2.16}$$

Besides, the power delay profile (PDP) characterizes the intensity of the power integrated over all azimuth angles arriving with a specific delay. The derivation of the PDP

from the PADP is given in following

$$\mathbf{PDP}_{\tau}[k] = \sum_{i} \mathbf{PADP}_{\tau}[i,k]. \tag{2.17}$$

Notice that those definitions of PDP and PAP may differ from the literature where it is also encountered an averaging instead of an integration [36, 98]. Those 2 definitions differ only by a scaling factor which is of no effect as long as the PAP and PDP are used as a power distribution for calculating the power spread in angular or delay domain. When one wants the level of those quantities to be meaningful one has to compensate for the fact that the same contribution is seen several times by the antenna pointing toward adjacent directions. This is known as the antenna de-embedding problem, the scaling factor to apply is different for both definitions.

By exploiting the sparsity[2] of the outdoor millimeter wave channel it is possible to integrate only over the indices which carry a significant amount of energy. This procedure is to limit the effect of integrating the noise level.

$$\mathbf{PAP}_{\phi,q}[i] = \sum_{q[k,i]} \mathbf{PADP}_{\tau}[i, q[k,i]], \tag{2.18}$$

$$\mathbf{PDP}_{\tau,q}[i] = \sum_{q[i,k]} \mathbf{PADP}_{\tau}[q[i,k], k], \tag{2.19}$$

where $q[k,i]$ and $q[i,k]$ are the restriction of the index set which corresponds to a certain quantile of the PADP power on a given row (respectively column). A good choice is to select a quantile at 75% meaning that only the indices which correspond to the 25% of the energy in each row (respectively columns) are summed for the projection.
A set of channel properties can be derived from the PDP and PAP and metrics based on LSPs are detailed subsequently in the following.

2.4.4. Large Scale Parameters

The second order characteristics of the radio channel known as LSPs are extracted based on the PDP and the PAP. Channel characterization metrics such as cross-correlation, omni-directional PL, K-factor, delay spread will be discussed next.

2.4.4.1. Cross-Correlation Parameters

The mutual dependency between the LSPs are usually described by the cross-correlation coefficient defined as in [70]

$$\rho(x,y) = \frac{\sum_{i=1}^{N}[x(i)-x_{\mu}][y(i)-y_{\mu}]}{\sqrt{\sum_{i=1}^{N}[x(i)-x_{\mu}]^2 \sum_{i=1}^{N}[y(i)-y_{\mu}]^2}}, \tag{2.20}$$

[2] In the literature, the word sparsity in mm-wave is used to refer the existence of only a few couples of significant paths in the mm-wave radio channel.

where N is the number of the snapshots, x and y denote any parameters of the LSPs and x_μ and y_μ are the mean of the LSPs x and y respectively. By definition, the cross-correlation between the LSP x and y ($\rho_{x,y}$) is defined between $[-1;1]$ where a value of zero means no correlation between LSPs x and y. When $\rho_{x,y}$ take a value of -1 or $+1$, this denotes that LSPs x and y are highly negative or highly positive correlated respectively.

2.4.4.2. Path-loss Model

The PL is a metric measuring the received power attenuated by the radio channel. In the literature, two path loss models for multi-frequency bands are identified [34, 99]: The CI free space reference and the ABG path loss model. The CI PL model is defined as

$$PL^{\mathrm{CI}}(f,d)[\mathrm{dB}] = \mathrm{FSPL}(f, 1\ \mathrm{m}) + 10n\log_{10}(d) + \zeta^{\mathrm{CI}}, \tag{2.21}$$

where $\mathrm{FSPL}(f, 1\ \mathrm{m})$ is the FSPL at 1 m, n the path loss exponent and ζ^{CI} is the shadowing fading (SF) of the CI PL model. d is in m while f is in GHz.

On the other side, the ABG PL model is based on the floating intercept expressed as

$$PL^{\mathrm{ABG}}(f,d)[\mathrm{dB}] = 10\alpha\log_{10}(d) + \beta + 10\gamma\log_{10}(f) + \zeta^{\mathrm{ABG}}, \tag{2.22}$$

where α, β, γ denote respectively the distance dependency exponent, the floating offset, and the frequency dependency exponent. ζ^{ABG} is the shadowing factor of the ABG PL model.
The characteristic of the CI PL model is the 1 m anchor point compared to the float intercept method that uses the least square fits of α, β and γ parameters. For both of them, the optimal parameters are found by minimizing the SF.

2.4.5. Fine Peak Search Method

Let first introduce the propagation path notion. By propagation path, we refer to paths that are discernible in the PADP and having physical meaning. The goal is to detect only significant paths from the measured data for LSPs studies. To this end, the fine peak search is considered[3] and presented in a similar way as in [36, 100, 101, 102]. First, we assume that only single peak (or path) is contained in one delay bin[4]. First, peaks indices are found in the delay domain by doing a local maxima peak search on the CIR

[3]The method is applicable for links in LOS conditions.
[4]This assumption makes sense when addressing large bandwidth.

and only peaks that satisfied the following conditions are considered

$$\begin{cases} CIR(\tau) > CIR(\tau - 1), \\ CIR(\tau) > CIR(\tau + 1), \\ CIR(\tau) > CIR_{th}^{meas} + th^{cst}, \\ CIR(\tau) \geq T_{th}(\tau);\ T_{th}(\tau) = \frac{1}{\Delta} \int_{\tau + \frac{\Delta}{2}}^{\tau + \frac{\Delta}{2}} CIR(t)\, dt, \end{cases} \tag{2.23}$$

where CIR_{th}^{meas} in dB denotes the measured noise level on the CIR, th^{cst} in dB is an additional threshold that can be set based on visual inspection of the CIRs in order to detect only meaningful peaks and $T_{th}(\tau)$ is a noise threshold obtained by a sliding window (Δ) average of the near-by delay bins. After that, a mapping between the founded delay and the maximum amplitude of the PADP is performed to find the associated azimuth angle. Finally, since the radiation pattern is recorded during the measurement and knowing the peak-normalized gain pattern, the maximum peak related to a specific delay and angle found in the previous step is estimated in the same delay and angular bins. At the end, the propagation path can be expressed as

$$\mathcal{P} = \{\tau_l, \phi_l, P_l\}_{l=1}^{Lp}, \tag{2.24}$$

where the detected peaks are characterized by a set of parameters $\mathcal{P}$ constituted by the estimated propagation delay (τ_l), the azimuth angle (ϕ_l) at the BS antenna and the power level P_l including the gain of antennas. From the fine peak detection, LSPs such as the rician K-factor, the DS, the omni-directional PL and the azimuth angular spread can be derived as in following.

2.4.5.1. Rician K-factor

It is well known that the envelope of the small-scale fading follows the Rician distribution in LOS case [103]. The Rician distribution is commonly characterized by the K-factor, which can be defined as the ratio between the strongest peak and the remaining power from MPCs

$$KF = \frac{P_{\text{LOS}}}{\left(\sum_{l=1}^{L_\text{p}} P_l\right) - P_{\text{LOS}}}, \tag{2.25}$$

where P_{LOS} is the power of the LOS component and $\sum_{l=1}^{L_\text{p}} P_l$ is the total power obtained by summing the contribution of the all detected MPCs. Notice that the highest the K-factor, the smallest the contribution of MPCs in the radio channel.

2.4.5.2. Delay Spread

The delay spread (DS) expresses the delay dispersion of the radio channel. Herein, the root mean square (RMS) DS is computed in the same way as, e.g., in [9, 103],

$$\tau_{RMS} = \sqrt{\frac{\sum_{l=1}^{L_\mathrm{p}} P_l \tau_l^2}{\sum_{l=1}^{L_\mathrm{p}} P_l} - (\overline{\tau})^2}, \tag{2.26}$$

where $\overline{\tau}$ denotes the mean excess delay defined as

$$\overline{\tau} = \frac{\sum_{l=1}^{L_\mathrm{p}} P_l \tau_l}{\sum_{l=1}^{L_\mathrm{p}} P_l}, \tag{2.27}$$

Typically, The RMS DS is a characterization of how much the power is spread around the mean w.r.t the propagation delay. A higher dispersion of the delay originated from the radio channel causes delay selective fading and interferences and consequently impacting strongly on the choice of a proper wave-front for upper-layer radio systems.

2.4.5.3. Omni-directional path-loss

Since the horn antenna is assumed to rotate effectively like an omni-directional antenna, the omni-directional PL can be estimated as

$$PL_{\mathrm{omni}}[\mathrm{dB}] = G_{\mathrm{ant}} - 10\log_{10} \sum_{l=1}^{L_\mathrm{p}} P_l, \tag{2.28}$$

where G_{ant} in dB is the maximum combined broadside antennas gain of the Tx and Rx antennas. The omni-directional PL presented in Eq. 2.28 considers the effect of the significant path contributions from the radio channel.

2.4.5.4. Angular Azimuth Spread

By assuming that paths are coming from the horizontal plane, the azimuth spread at the Rx side (AAS) can be computed as

$$S_\phi = \sqrt{\frac{\sum_{l=1}^{L_\mathrm{p}} |\exp(j\phi_l) - \mu_\phi|^2 P_l}{\sum_{l=1}^{L_\mathrm{p}} P_l}}, \tag{2.29}$$

where μ_ϕ is the mean azimuth angle defined as:

$$\mu_\phi = \frac{\sum_{l=1}^{L_\mathrm{p}} \exp(j\phi) P_l}{\sum_{l=1}^{P_\mathrm{p}} P_l}. \tag{2.30}$$

Similarly to the delay spread, the angular spread is important to considerer in the design of the system since impacting on the choice of the beam-former: the smaller the AAS, the simplest the beam-former.

2.5. Summary

In this chapter, fundamental concepts of the radio channel basis have been presented as well as a detailed review of existing channel modeling activities in the mm-wave context. The general trend in mm-wave is going toward a small and dense cells deployment since mm-waves are experimenting high attenuation which leads to sparse channels. Several measurement campaigns conducted in mm-wave bands and reported in the literature revealed the dominance of the LOS and the specular reflection compared to the diffraction and the diffuse scattering mechanisms. Furthermore, a various characterization of channel properties, that will be used in the next chapter, is presented in this part. The review of the current and ongoing channel models highlight the need of providing mm-wave measurements database for a better description of the mm-wave channel model. Furthermore, calibrating the site-specific techniques that are gaining an increase in consideration through measurements are essential. Next, measurement campaigns conducted in cm- and mm-waves and covering various realistic propagation scenarios are addressed.

Chapter 3

Channel Measurements

The radio channel is a critical component of the cellular system and especially when it comes to fulfil strong requirements from the 5G technology. As highlighted in the previous chapter, it is still necessary to increase the knowledge about the mm-wave channel through measurements. Furthermore, performing channel sounding remains important when it comes to calibrate site-specific tool as the one that we have used in this work.

However, channel sounding is known to be time-consuming as well as the post-processing. Conducting radio channel sounding is not only about recording the measured data. Usually, the channel sounder equipment is not compact in the sense that cables, electrical power, and other RF equipment need to be connected to each other. Furthermore, equipment needs to be packaged, transported before the measurement from the laboratory to the measurement site. Human resources for helping for the packaging/unpackaging equipments as well as moving the receiver location during measurements are highly needed. On the other hand, depending on the type of the addressed measurements and the parameters setup, the measurement time for recording data can be rapidly very large. Moreover, administrative authorizations from local authorities are sometimes necessary to perform measurement and especially when it comes to address UMi and UMa scenarios for instance.

In this chapter, we present the measurement campaigns performed in different frequency bands by using several mm-waves wideband radio channel sounding. The description of the investigated scenarios is also presented as well as the discussion about the measured data is provided.

3.1. Motivations

Besides gathering insight about mm-wave channel measurements, the main purposes of the measurement campaigns presented in this thesis are classified as follows:

- Purpose 1: investigating the time variability of the mm-wave radio channel. Meas-

urements were performed by assuming a static position of the Rx while the Tx was moving along routes simulating a trajectory. A horn antenna designed in vertical polarization and pointing in the Tx direction was used on the Rx side while a biconical antenna designed in vertical polarization was used at the Tx side.

- Purpose 2: investigating the scattering environment and evaluating the performance of the RT tool. Measurements were conducted in a situation where the Tx and the Rx were in a fixed position. A horn antenna designed in vertical polarization and rotated in the azimuth plane was used in the Rx while a biconical antenna designed in vertical polarization was used at the Tx.

A total of four extensive measurements covering various representatives InH and outdoor scenarios were conducted in different frequency bands as reported in Table 3.1.

Table 3.1.: Overview of the measurement campaigns.

Spec.	**Scena.**	**Freq.** (GHz)	**W** (GHz)	**# links**	**comments**	**purpose**
Meas.0	Out.: LOS & NLOS	28	0.8	1000	Tx: Mobile; Rx: static with no rotation.	1
Meas.1	InH: LOS & OLOS	28	2	2900	Tx: Mobile; Rx: static with no rotation.	1
Meas.2	InH: LOS & NLOS	15, 28, 83	3	60	Tx: static; Rx: static with rotation	1 & 2
Meas.3	Umi: LOS & NLOS	32.6	1.6	16	Tx: static; Rx: static with rotation	2

Meas.0 and *Meas*.1 are performed through the purpose 1. These measurements consist of mobile measurements performed at 28 GHz in outdoor and indoor scenarios respectively. The dynamic channel at 28 GHz was investigated in a way that the Rx antenna was in a fixed position at a height of 1.82 m and the Tx antenna with the same height was moving along several routes covering both LOS, obstructed LOS (OLOS) and NLOS configurations. Data acquired in such configurations are analyzed and subjected to statistical studies.

Meas.2 is in the scope of the purpose 1 and 2. It consists of an intensive measurement campaign performed in cm- and mm-waves frequency bands at 15, 28 and 83 GHz. The multi-frequency measurements were performed in a typical conference room including indoor furniture. A total of 60 links separated with a distance of 50 cm were investigated

at the three frequency bands. For a fair comparison, a same bandwidth (W) of 2 GHz and a same number of frequency point N_f of 2001 were set for the three channel sounders. Measurements data are first analyzed in this chapter and compared to the RT simulation in chapter 4.

*Meas.*3 is in line with the purpose 2. *Meas.*3 is an UMi measurement campaign performed at 32 GHz. 16 links were investigated: 13 in LOS and 3 in NLOS conditions with a link distance ranging from 15 m to 80 m. The analysis of the mm-wave UMi scattering environment is provided in this chapter and a comparison between the measurement data and the RT simulation is provided in chapter 4.

3.2. Directional Channel Sounding

One of the advantage when dealing with mm-wave is the possibility to access a large bandwidth (easily over 1 GHz). Performing measurement campaigns with a large bandwidth allows to resolve more paths without ambiguity by offering a fine delay resolution. Technically, achieving this kind of measurements can be done by using a vector analyzer network (VNA) stating for a frequency domain channel sounding technique. The principle of the frequency domain channel sounding technique is to divide the addressed band in a finite number of frequency points (Nf). A narrowband signal is transmitted at a single frequency point over an intermediate frequency bandwidth (IFBW) and swept over the all addressed band. Then, the amplitude and the phase of the attenuated transmitted signal traveling through the radio propagation environment is measured at the Rx side. In the remainder, wideband channel sounders based on VNA will be used.

3.2.1. Mm-waves Frequency Bands

In the 5G context, it is expected to have an ubiquitous connectivity of a massive number of devices represented by the machine type communications and an ultra-reliable with a very small latency communications. These requirements are expected to be achieved in service for IMT2020 systems below 6 GHz to meet the wide coverage requirements. On the other hand, enhanced mobile broadband (eMBB) applications in UMi scenario would target frequency ranges above 24.25 GHz. More specifically, the portion of the frequency range between 24.25 GHz and 86 GHz under consideration for a future identification of these systems, are: $24.25 - 27.5$ GHz, $37 - 43.5$ GHz, $45.5 - 50.2$ GHz, $50.4 - 52.6$ GHz, $66 - 76$ GHz and $81 - 86$ GHz as illustrated in Fig. 3.1.

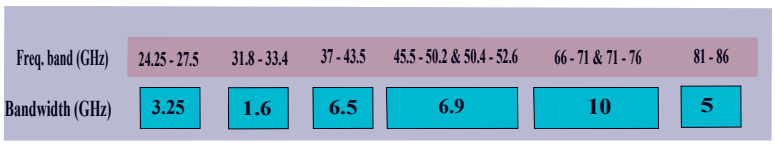

Figure 3.1.: Mm-wave frequencies identified at by the ITU at the WRC-15.

More specifically, radio spectrum policy group (RSPG) focused its consideration to identify the 5G band in Europe above 24 GHz, i.e., 24.25−27.5, 31.8−33.2 and 40.5−43.5 GHz [104]. Indeed these bands could potentially provide sufficient outdoor deployment with indoor coverage, mainly due to the presence of the LOS and the specular reflection (SR) components along with some capability of beamforming in the infrastructure and the MS. Moreover, some countries such as USA and Korea expressed their interests for an early deployment around 28 GHz [105, 106] supported with academic researchers investigating the propagation characteristics at the band, e.g. [30, 80, 101, 107]. Therefore, the above mentioned bands motivate us to cope four specific frequency bands in our study i.e.: $14-15$ GHz, $27-30$ GHz, $31.8-33.2$ GHz and $82-84$ GHz.

3.2.2. Synthesized Omni-directional Antenna

The mm-waves suffer from strong losses due to the small wavelength. Accordingly, to be able to catch the signal in mm-wave with reasonable dynamic range, the use of directional antennas is fundamental. For our measurements, a horn antenna that offers a high gain while being directive have been used for compensating losses[1]. Since the horn antenna presents a directive pattern while having a narrow beam-width, achieving a full sectorization of the azimuthal plane is possible by rotating the horn antenna in the azimuth plane. Indeed, the idea is to repeat the measurements for different pointing angles in order to cover synthetically all channel directions. Such a procedure is stated for synthesized omnidirectional channel sounding technique. Using such a procedure allows capturing significant paths projected in the azimuth plane as would almost do an omni-directional antenna. For instance, plenty of works follow this principle to perform measurement campaigns in the literature [21, 101, 102, 108, 109].

3.2.3. Calibration

The calibration consists of removing the effects brought by the channel sounder itself. Since the channel sounder incorporates RF components and other cables, such effects need to be removed from the measurement data to avoid any errors and to make the data trustable and usable. To this end, before any measurement campaigns, a full back-to-back (B2B) calibration is performed by directly connecting the end cables of the Tx and the Rx antennas. The transfer response function (TRF) of the B2B calibration is measured, stored and used in the processing step.

3.3. Mm-wave Channel Soundings

The measurement campaigns performed in *Meas.*0, *Meas.*1, *Meas.*2 and *Meas.*3 were done by using the frequency domain channel sounder from Aalto University. It relies on a VNA that measures the CTF of the radio channel as shown in Fig. 3.2.

[1] Notice that in a practical 5G scenario, it is expected to use steerable antenna arrays.

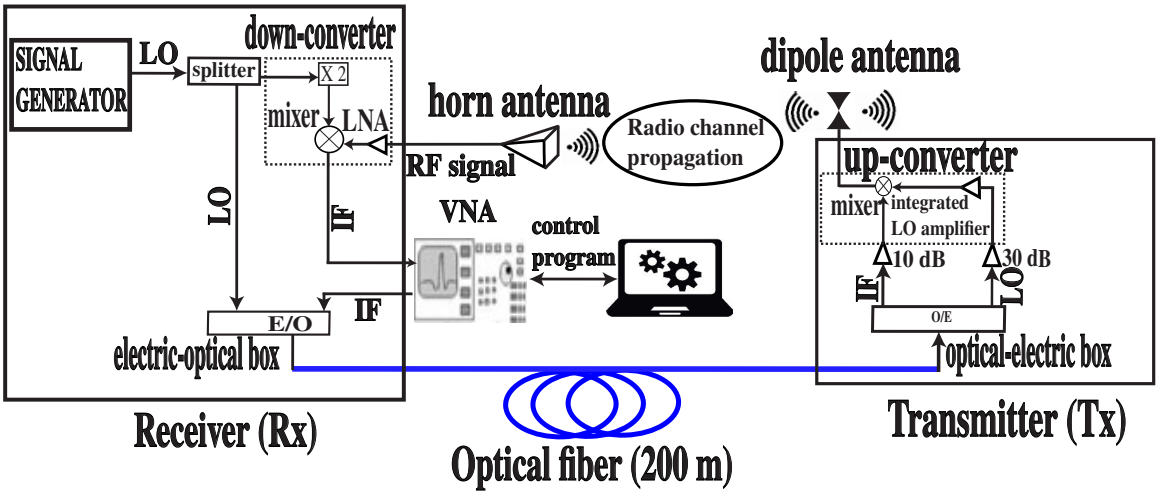

Figure 3.2.: Block diagram of the mm-wave wideband Aalto's channel sounder (at 28 GHz).

The Rx part is made of the horn antenna preceded by the down-converter integrating the low noise amplifier (LNA) and an internal frequency fed by the splitter of the local oscillator (LO) of the signal generator. An optical cable working up to 18 GHz was used to make possible the separation between the Rx and Tx up to 200 m while reducing losses as shown in Fig. 3.2. On the other side, the Tx consists of the biconical antenna fed by the up-converter integrating a mixer and a LO amplifier. Depending on the targeted frequency band, up- and down-converters with a doubler or sixfold internal frequency can be used. Furthermore, depending on the purpose of the measurement, the horn antenna can be mounted on a fixed rotational system in order to perform an azimuth scan while the Tx is in a fixed position (e.g. *Meas.*2 and *Meas.*3). On the other hand, the Tx antenna can be mounted on a trolley and moved manually while the Rx antenna is in a fixed position without rotation (e.g. *Meas.*0, *Meas.*1). A single laptop is used to manage the VNA and the rotational system (if used). In the remainder, we will use BS and MS to refer the Rx and the Tx antennas respectively.

3.3.1. Outdoor and InH Channel Soundings in Mobility

3.3.1.1. *Meas.*0: Outdoor Mobility

The details of the parameter settings used in *Meas.*0 are listed in Table 3.2.
Carrying-out a dynamic measurement by using a VNA is quite challenging due to the slow frequency sweep acquisition mode. This rigorously would imply to assume that the channel is not changing during the sweep time which is a strong assumption. This method which is intrinsically biased should be interpreted carefully and need to find a good trade-off between having a fast acquisition while ensuring a reasonable dynamic range (at least 20 dB for capturing significant paths). To this end, a small number of

Table 3.2.: Parameter settings of the channel sounder used in *Meas*.0

VNA	LO	Antennas
Freq. : $0.75 - 1.25$ GHz	14 GHz	$28.75 - 29.25$ GHz
Power : -15 dBm	7 dBm	MS: {Biconical (2 dBi), HPBW: 60° el., height: 1.75 m}
Sweep points : 801	-	BS: {Horn (19 dBi), HPBW: 10° az. & 40° el., height: 1.75 m}
IFBW : 10 KHz	-	-

sweep points (801) and an IFBW of 10 KHz were set in the VNA parameters.

Meas.0 was conducted in the area campus of Aalto University[2] and the layout of the measurement environment is shown in Fig. 3.3.

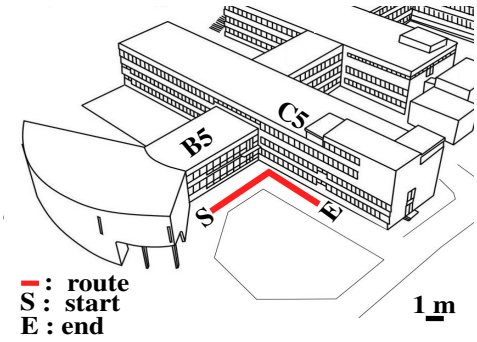

Figure 3.3.: Map of the measurement environment *Meas*.0. Bikes, trees, bushes, and lamp-posts were present in the measurement site but are not represented in the map.

The aperture of horn antenna (BS antenna) was pointing in the direction of building C5. The BS antenna was fixed approximately at 15 meters from the building C5 while the MS antenna mounted on a trolley, was moved manually while keeping a low and constant speed along the sidewalk route. Both BS and MS antennas have the same height of 1.75 m. The sidewalk route presented a quite smooth and flat ground and the sidewalk is bordered by buildings B5 and C5. As shown in Fig 3.3, the chosen route includes both LOS (route parallel to B5) and NLOS (route parallel to C5) configurations. Walls of buildings B5 and C5 are mostly constituted by brick and windows are made of double glass surfaces. No pedestrians were present during the measurement. A total of 1000 snapshots was recorded over a traveling duration of 191 s that yields a snapshot separation of 3 cm. Worthy notice that no paths were detected above 125 s, corresponding to the moment where the MS antenna was going outside the horn antenna radiation. Fig 3.4 illustrates the time-variant CIR extracted from *Meas*.0.

The channel is observed to be sparse and exhibiting only four strong spatially consistent contributions. The LOS component (path #1) and the 1^{st} order SR path over building C5 (path #3) can be clearly observed from Fig 3.4. Two other paths namely path #2

[2]Latitude (Lat) and Longitude (Long) of the BS: Lat: 60.188881° Long: 24.83034°

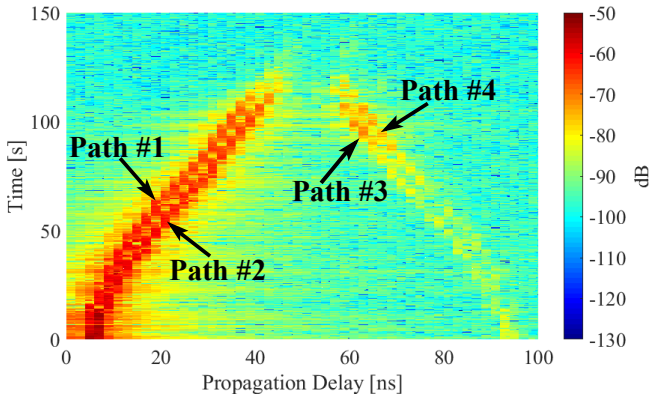

Figure 3.4.: Illustration of the measurement error ($Meas.0$): example of CIR obtained by applying the inverse Fourier transform ($\mathcal{F}^{-1}$) to the of $Meas.0$.

and path #4 are also observed. At first sight, path #1 and path #2 could be interpreted as the LOS and the ground reflection (GR) paths. However, the absolute value of the separation between the two paths and the constant separation as the time evolves is not compatible with this hypothesis.

At second sight, one hypothesis would be the presence of a strong reflector at about 1 m from the MS antenna since the intensity of the path #2 is quite the same as the power of the LOS path. However, according to the procedure of the measurement, no object or metal was near antenna at the distance of around 1 m except the operator body that was pushing the trolley. Geometrically, attributing path #2 to a single reflection from the operator body and path #4 as a double reflection (from the operator body and the building C5) would make sense if we look at only the delay information. However, from the electromagnetism laws point of view, it is quite impossible that the operator body produces a stable reflection for different reflected angles. Such a hypothesis means that the Snell's law of reflection is always fulfilled across different locations of the MS, which does not make sense.

Finally, after a careful analysis, path #2 and path #4 have been attributed to coming from the measurement setup error. Indeed, the source of such paths may come from to a bad isolation or a bad tightening of connectors and therefore yielding a ringing of the signal that cannot be removed during the B2B calibration step.

3.3.1.2. $Meas.1$: Description of the 28 GHz Channel Sounding

The modus operandi consisting in evolving a trolley in $Meas.1$ was the same as in $Meas.0$ except the parameter settings and the horn antenna as detailed in Table 3.3. The same antenna height of 1.83 m was set for both the BS and MS antennas.

Table 3.3.: Parameter settings of the 28 GHz channel sounding used in *Meas*.1

VNA	LO	Antennas
Freq: $1-4$ GHz	13 GHz	$27-30$ GHz
Power: -15 dBm	12 dBm	fc: 28.5 GHz
Sweep points: 10001	-	MS: {Biconical (2 dBi), HPBW (60° el.), height: 1.83 m}
IFBW: 20 KHz	-	BS: {Horn (19 dBi), HPBW (40° az. 10° el.), height: 1.83 m}

3.3.1.3. *Meas*.1: Description of the Environment

Meas.1 was conducted in two different indoor environments while investigating six trajectory routes as listed in Table 3.4. A normal office (I1) and a library (I2) were investigated as shown in Fig. 3.5.

I1 is a small indoor office room with a size of $6.9 \times 4.4 \times 4$ m^3. Windows are made of double glasses and two bookshelves with a size of $1.65 \times 0.5 \times 1.7$ m^3 were present and placed in the middle of the room while some small objects were present on the top of the bookshelves. Two short routes in LOS conditions were addressed in I1: I1-R11 and I1-R12. I1-R11 (dashed black line in Fig. 3.5.a) was aligned in the direction of the illuminated horn antenna in bore-sight while I1-R12 was in a crossing situation (dashed red line in Fig. 3.5.a).

I2 is a library environment where computers, artificial trees, chairs and other furniture were present but not represented in the layout in Fig. 3.5. Twelve bookshelves with a size of $3.74 \times 0.54 \times 2.165$ m^3 were present and distributed as shown in Fig. 3.5b. They are mostly made of wood and bookshelves were filled with books. Four routes were explored: the longest one (I2-R21) in LOS situation that covered the direction of the radiated horn antenna and three short routes in a crossing situation (I2-R22, I2-R23 and I2-R24) as illustrated in Fig. 3.5b. Notice that the library is like an atrium where the height of the ceil was about 15 m.

Table 3.4.: Characteristic of the investigated routes of *Meas*.1.

env.	route	#samples	dist.(m)
I1	I1-R11 (LOS)	300	3.08
I1	I1-R12 (LOS)	200	1.66
I2	I2-R21 (LOS)	1200	16.35
I2	I2-R22 (OLOS-LOS-OLOS)	500	4.6
I2	I2-R23 (OLOS-LOS)	300	2.34
I2	I2-R24 (OLOS-LOS)	300	2.09

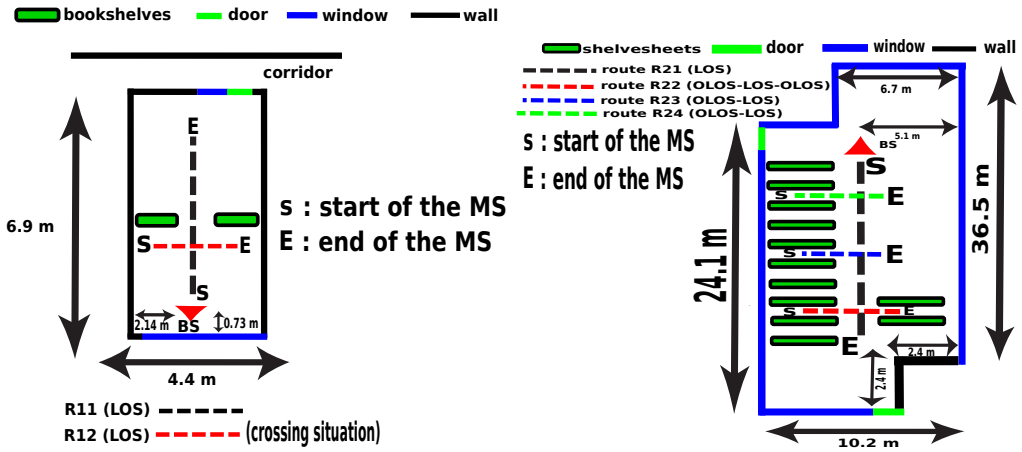

(a) (b)

Figure 3.5.: Layouts of the InH environments: On the left (a) the normal office (I1) and the library (I2) on the right (b).

All the routes presented a flat and smooth ground floor. No pedestrians were present during the measurement and photos of the measurement site of *Meas.*1 are given in Fig. 3.6.

(a) (b)

Figure 3.6.: Photos of the measurement site: the normal office in (a) and the library in (b).

3.3.2. InH Mobile Measurements Data Analysis

3.3.2.1. Data Analysis

The CIR time-variant is derived from the measurement dataset by applying an inverse Fourier transform. The mm-wave dynamic CIRs of the InH office room of I1-R11 and I1-R12 are displayed in Fig. 3.7. The varying CIRs in both cases exhibit significant and

consistent paths as the MS is moving. Focusing on Fig. 3.7.a and from the geometry of the environment, we can identify the LOS component which is the strongest one and the 1^{st} order of SR from the front of the wall appearing around 36 ns at the beginning of the movement. This latter path is characterized by a decrease of the propagation delay as the MS was moving far from the BS antenna and becoming closer to the front of the wall. Similarly, four other paths appearing at the beginning of the movement at around 52, 82, 97, and 143 ns are respectively identified as the 2^{nd}, 3^{rd}, 4^{th}, and 5^{th} order SR from the front of wall and the window on the opposite side. The same observation is valid for the crossing situation illustrated in Fig. 3.7.b.

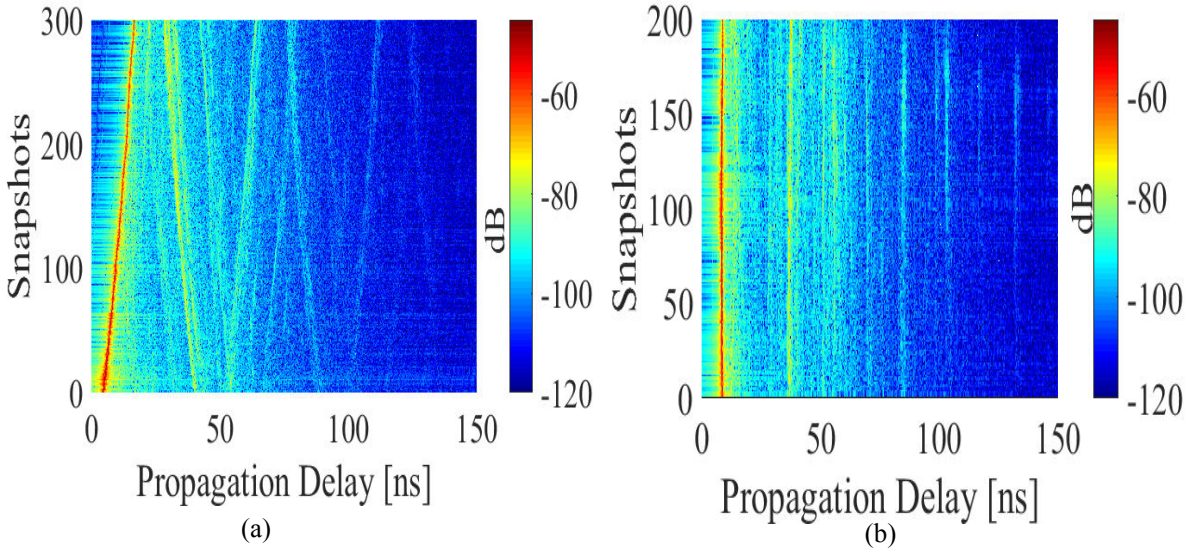

Figure 3.7.: Dynamic radio channel of I1-R11 (a) and I1-R12 (b).

Fig. 3.8 shows the dynamic radio channel of the library environment. The spatial channel variation of the trajectory I2-R21 depicted in Fig. 3.8.a exhibits significant consistent MPCs. The amplitude of the LOS path is smoothly decreasing as the MS moves and the distance of the LOS component increases from 2 m to 16.7 m. The MPCs remain remarkably stable as the Tx is moving. In addition, the MPCs are observed to be quite correlated and spatially distributed as in the indoor office room in the sense that the paths are mirrored in the delay domain and presenting quite the same slope indicating the presence of multiple SRs.

In Fig. 3.8.b, Fig. 3.8.c and Fig. 3.8.d illustrating the crossing route (OLOS and LOS trajectories), we can notice that some MPCs are appearing to be strong corresponding to the instant where the MS antenna is going from the OLOS situation to the LOS situation. For instance, in Fig. 3.8.b, some MPCs are appearing with a higher amplitude between the 100^{th} and around the 410^{th} snapshots corresponding to the LOS situation. Similarly, some MPCs appear with a higher level of power when the MS is entering in the LOS configuration.

Furthermore, the three crossing route situations in the library environment revealed an always existing direct path thank to the transmission mechanism while the MS was in OLOS configuration. The transmission mechanism through bookshelves filled by books has two effects: a 15 dB attenuation and a delayed direct path. This means that in a particular context as the library which has been addressed, the direct path is maintained due to probably the sufficient transparency of bookshelves at 28 GHz.

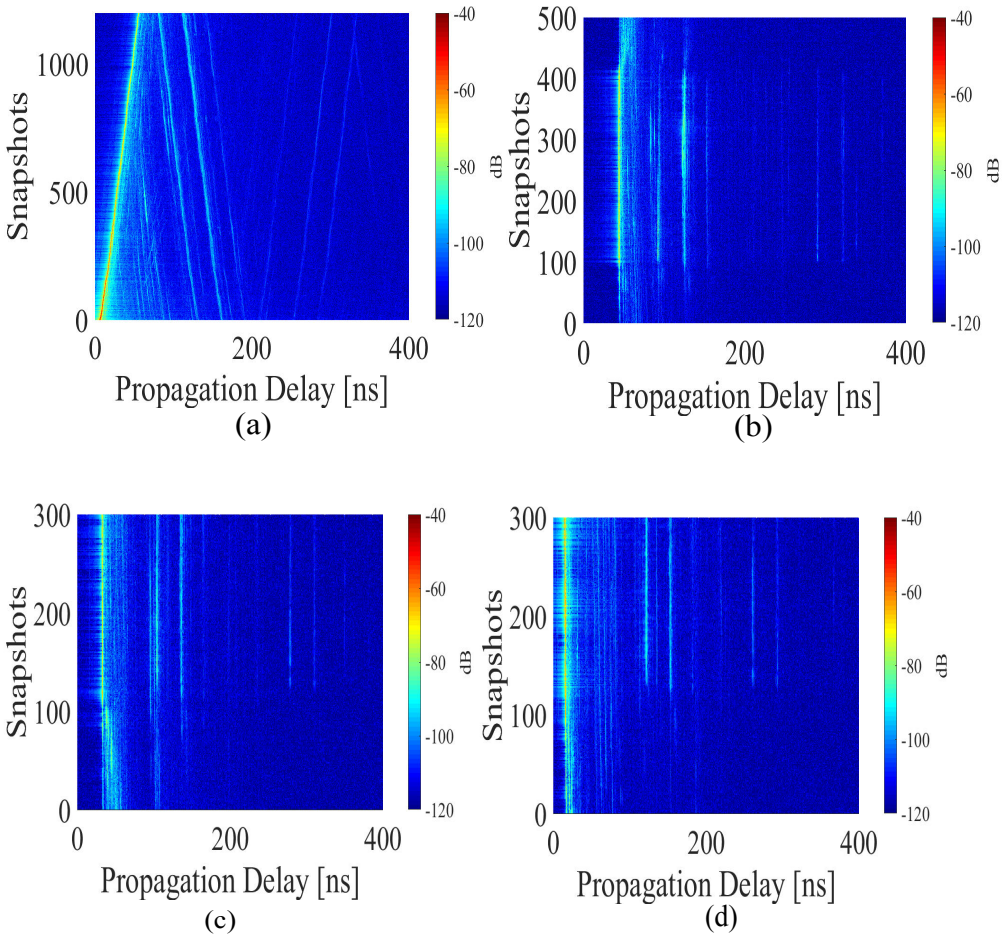

Figure 3.8.: Dynamic radio channel of I2-R21, I2-R22, I2-R23 and I2-R24.

The most noticeable observation is when comparing Fig. 3.7.a and Fig. 3.8.a showing the time-variant CIR of I1-R11 and I2-R21 respectively. We can observe that MPCs in the office room are more rich and dense compared to those in the library. This observation may be explained in the electromagnetism reverberation point of view. First, the volume of the office room is much smaller by a factor of 40 meaning that the office room is potentially much more reverberant than the library environment. When the environment

is getting larger, the reverberation is becoming negligible. Furthermore, the material of the walls in the office room that are mostly made of concrete are different from those in the library that are made of window glasses. On the modelling point of view, this may suggest that for small environment, the reverberation should be added while for the voluminous environment, this may be useless.

3.3.2.2. LSP analysis

The LSPs extracted in the measured data were derived from the fine peak detection method presented in the previous chapter. A value of 8 dB was set for the th^{cst} to avoid possible detection of noisy peaks while a sliding window (Δ) length of 1 ns was considered in the fine peak detection. Table 3.5 provides statistical parameters of the LSPs for I1-R11 and I2-R21 and also makes a comparison against those reported in [15] at 28.5 GHz in InH scenario.

Table 3.5.: Summary of the LSPs comparison obtained from I1-R11 and I2-R21 at $f_c =$ 28.5 GHz against those reported in the 3GPP channel model [15] applicable into mm-wave radio frequencies and covering the LOS InH office.

	InH		
Spec.	$I1$-R11	$I2$-R21	3GPP
DS [ns]			
μ(log10([s]))	-8.2	-8	-7.8
σ(log10([s]))	0.1	0.3	0.3
KF [dB]			
μ_{KF}	11.8	10.7	3.4
σ_{KF}	3.7	4.7	5.3
cross-correlations			
DS vs KF	-0.9	-0.6	-0.5

Generally, the computed values derived from $Meas.1$ are in line with those reported in the 3GPP [15] except the KF values in $Meas.1$ presenting high values compared to those in the 3GPP. The difference could be explained by the fact that, in contrast to the 3GPP, we are using in our measurements a selective antenna (horn antenna) at the BS side and hence we are not capturing paths from the all radio channel directions justifying potentially the observed difference.

The inter-dependency between the DSvsKF is found to be highly negatively correlated in the office room, the library and the 3GPP. Since the LOS condition is considered and accordingly to the small addressed distance, a highest KF can be attributed to a dominance of the LOS component and therefore lead to a small DS and then justifying the strong negative cross-correlation between the DS and the KF. Such reported values

would be useful for 28 GHz indoor radio channel simulation and system design for the parameterization of the 3GPP channel models.

3.3.3. Multi-frequency Conference Room Synthesized Omni-Directional

3.3.3.1. *Meas.*2: Multi-frequency Channel Soundings

The multi-frequency wideband channel sounding used at 15, 28 and 83 GHz presents all the same configuration but differing slightly in the parameters setup and the use of the up- and down-converters. In 15 GHz channel sounding, no up- and down-converters were used since the VNA and the optical fibre were able to cover a frequency band up to 24 GHz and 18 GHz respectively. Up- and down converters having a double internal frequency were used for the 28 channel sounding while up- and down-converters with a sixfold internal frequency were used for the 83 GHz channel sounding. Moreover, two extra wave-guides (WR-12) were used for the 83 GHz channel sounding. Furthermore, for a fair comparison, the different horn antennas at the three frequency bands are designed for having the same HPBW of 10° in azimuth and 40° in elevation. The parameter settings used for the channel sounders at 15, 28 and 83 GHz are summarized in Table 3.6 and photos of the antennas used in *Meas.*2 are depicted in Fig. 3.9.

Table 3.6.: Summary of the parameter settings of the mm-wave synthetized omni-directional channel sounders.

Description	**15 GHz**	**28 GHz**	**32 GHz**	**83 GHz**
RF signal (GHz)	$14-16$	$27-29$	$31.8-33.4$	$82-84$
W (GHz)	2 GHz		1.6 GHz	2 GHz
Sweep points	2001		10001	2001
IF signal (GHz)	$14-16$	$1-3$	$0.8-2.4$	$1-3$
LO signal (GHz)	n/a	13	15.5	13.5
internal frequency	n/a	$\times 2$		$\times 6$
VNA transmit power (dBm)	-15			
MS antenna	biconical (2 dBi), HPBW: 60° (el.), omni-directional (az.)			
BS antenna	horn (19 dBi), HPBW: 40° (el.),10° (az.)			
Rx configuration	Rotational ($0° : 5° : 360°$)		Rotational ($45° : 5° : 270°$)	Rotational ($0° : 5° : 360°$)
MS antenna height (m)	1.65			
BS antenna height (m)	1.65		6	1.65
B2B calibration: attenuator (dB)	20			30

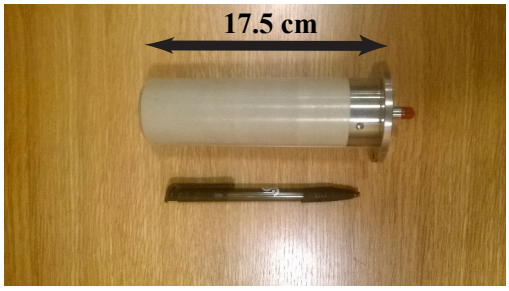

(a)

(b) Biconical antenna at 15 GHz.

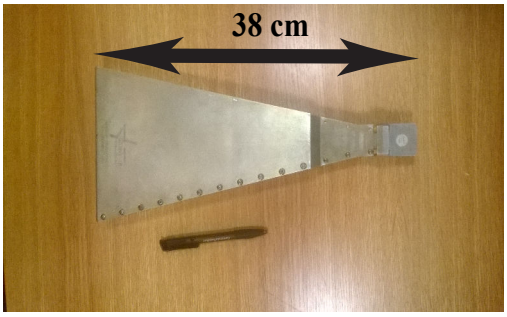

(c)

(d) Horn antenna at 15 GHz.

(e) Biconical antenna at 28 GHz.

(f)

(g) Horn antenna at 28 GHz.

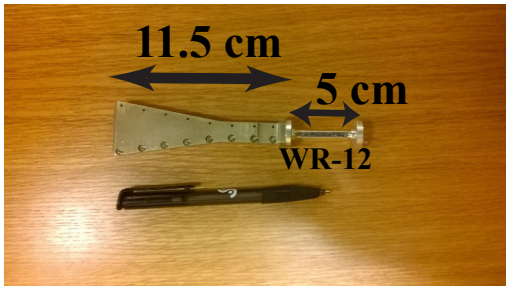

(h) Horn antenna at 83 GHz.

Figure 3.9.: Pictures of the biconical and the horn antennas used in *Meas.*2.

Worthily mentioning that the measurement time for one single location including the full rotation of the BS antenna in *Meas.*2 was about 2.5 minutes.

3.3.3.2. *Meas.*2: Description of the InH Conference Room

The radio propagation environment of *Meas.*2 is a typical indoor conference room. Walls are mostly made of concrete, windows are double glasses and some woods furniture were present in the measurement room (R1) as shown in Fig. 3.10. A cupboard made essentially in wood was present to cover the board. A long table at a height of 1 m from the ground level and chairs were present in the middle of the room but are not represented

in Fig. 3.10. The BS antenna was located inside the room R1 at a height of 1.65 m from the ground while the MS antenna with the same height was placed successively inside the room R1 and on the corridor with a MS separation of 0.5 m as illustrated in Fig. 3.10. The MS positions were chosen for emulating a trajectory route covering both LOS and NLOS conditions.

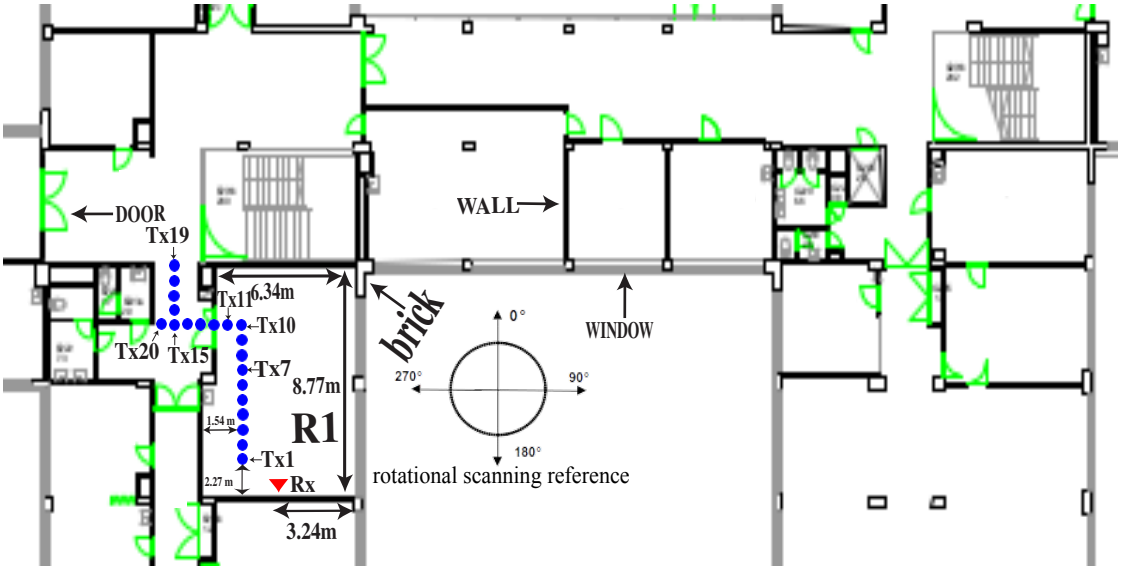

Figure 3.10.: Layout map of the conference room.

In summary, 20 links per frequency band were recorded yielding a total of 60 CTFs. Among the 20 links, 13 were in LOS conditions (MS1, MS2, MS3, MS4, MS5, MS6, MS7, MS8, MS9, MS10, MS11, MS12 and MS19) and 7 in NLOS conditions (MS13, MS14, MS15, MS16, MS17, MS18 and MS20). Measurements were conducted during off-peak hours and measurements were performed in a static environment. Fig. 3.11 depicts some photos of the investigated conference room.

3.3.4. Multi-frequency Conference Room Data Analysis

First, Fig 3.12 displays an example of the PDP derived for the link BS-MS1 and BS-MS7. A rectangular window was applied to the measured data.

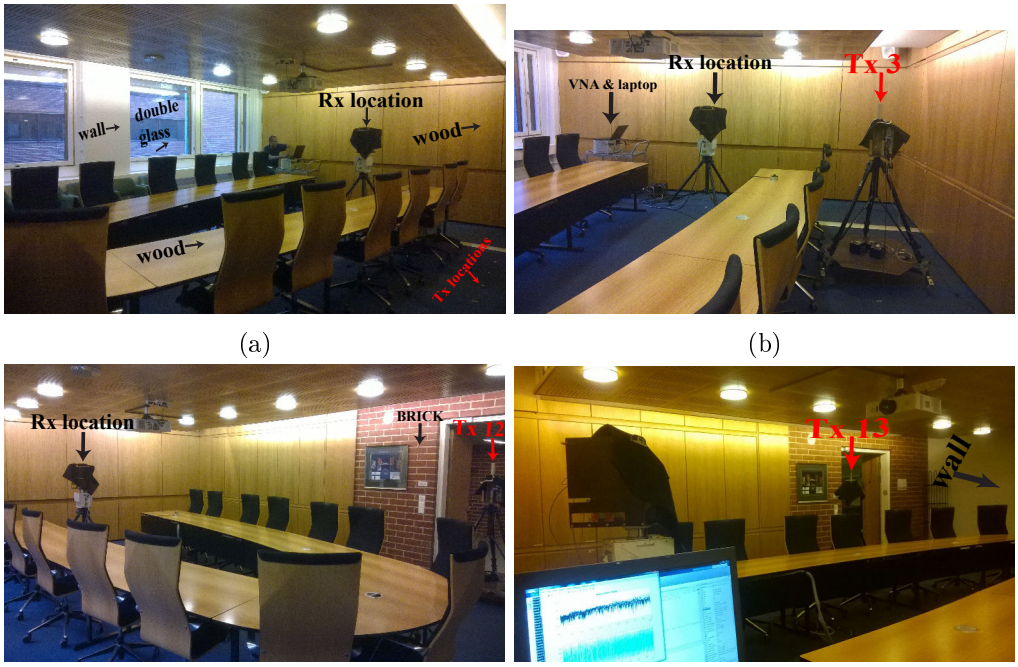

(a) (b)

(c) (d)

Figure 3.11.: Photos of the conference room measurement site.

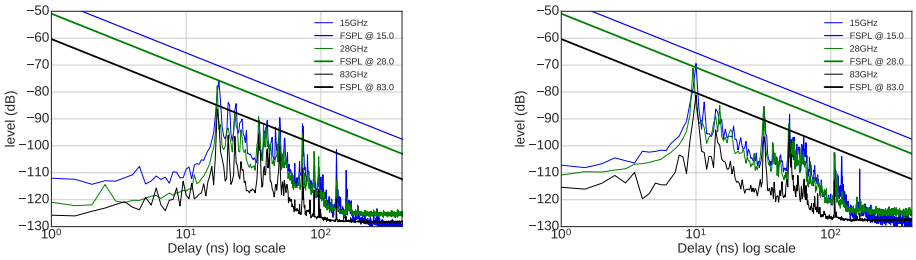

(a) BS-MS7. (b) BS-MS1.

Figure 3.12.: Example of PDPs derived for the links BS-MS1 and BS-MS7.

First, the amplitude of the LOS component at 15 GHz is observed to be attenuated when comparing it to the FSPL. This is attributed to a mismatch between the RF cable and the BS antenna port for the 15 GHz channel sounder yielding a leak of a power. Furthermore, as illustrated in Fig 3.12, the measured PDP at the three frequency bands present the quite same profile and the dominant paths (mostly coming from the 1^{st}, 2^{nd} and 3^{rd} order SR paths over walls, ceil, ground, windows) are retrieved at the three frequency bands while the level of the power is becoming smaller at 83 GHz compared to the 15 GHz frequency band.

Second, Fig 3.13 and Fig 3.14 show the evolution of the PDP and the PAP along

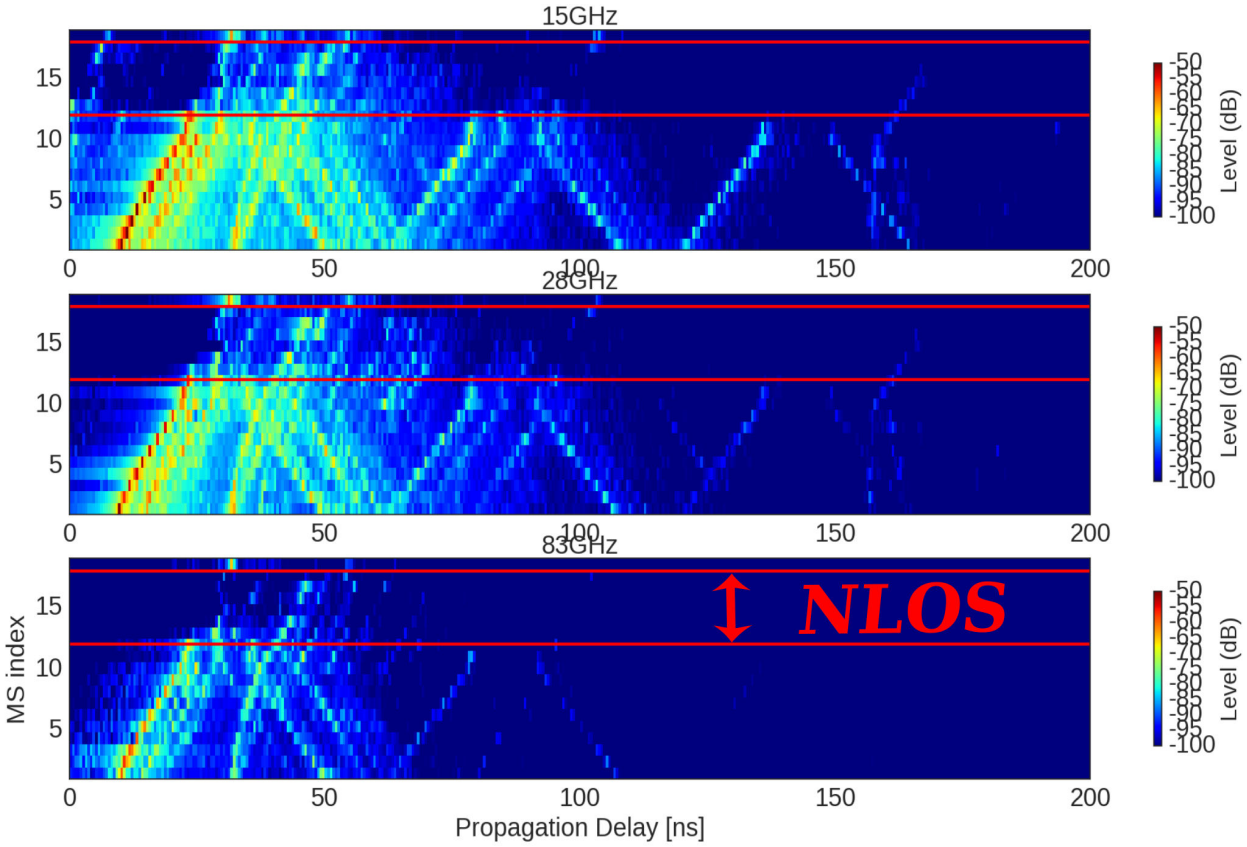

Figure 3.13.: Evolution of the PDP over the trajectory.

the synthetic route (LOS/NLOS/LOS)[3] at 15, 28 and 83 GHz. The horizontal red line indicates the transition between LOS and NLOS conditions. It can be observed that the structure of the channel is spatially consistence and relatively invariant as the frequency is changing over a large range as illustrated in Fig 3.13 and Fig 3.14. Furthermore, the dense structure of the channel seems to decrease when going in higher frequency. However, since the dynamic range is not the same at the three channel sounders, no relevant conclusion cannot be made on the sparsity of the radio channel or the presence of the diffuse scattering mechanism when dealing with higher frequency. Further careful analysis need to be done toward such investigations.

This measurement dataset will be used in the next chapter for comparison purposes against the RT simulation.

[3]Excluding the position of the MS20.

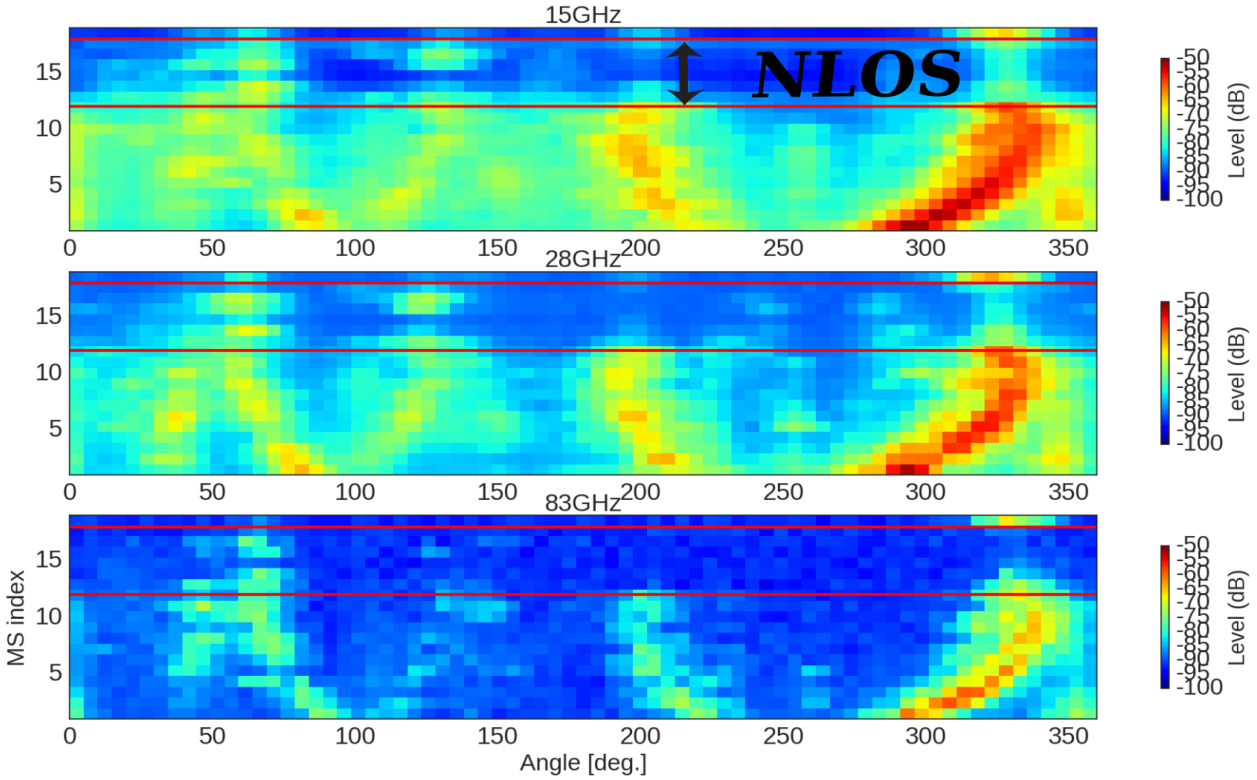

Figure 3.14.: Evolution of the PAP over the trajectory.

3.3.5. UMi Synthesized Omni-Directional Characterization

3.3.5.1. *Meas.*3: 32 GHz Channel Sounding UMi

The 32 GHz channel sounding used to perform measurement campaign in *Meas.*3 is the same as the one used at 28 GHz in *Meas.*2 with a difference residing in the parameter settings as agreed in the previous big Table 3.6. In addition, an elevation down-tilt of 10° was applied to the BS antenna. Furthermore, a small IFBW and a large number of frequency points were chosen to improve the dynamic range of the measurement. However, we were facing a bad dynamic range characterizing to a high noise level. We attributed this effect to the channel sounder and especially to the use of a long length of cable (10 m of cables) that connected the up-converter mounted on the rotator system located at a height of 6 m to the VNA located on the ground level.

The measurement time for measuring one single link location was about 8 minutes.

3.3.5.2. *Meas.*3: Description of the UMi environment

The measurement campaign of *Meas.*3 was carried out in the city of Espoo, Finland. The coordinates of the BS position are: latitude 60.204409° and longitude 24.659568°. The measurements were conducted during working hours while pedestrians, cars, trucks and

public transportation including buses and taxis were present in the measurement site. The considered environment represents a typical UMi scenario where the BS antenna was deployed near the facade of a building R as shown in Fig. 3.15. The height of the BS antenna was set to 6 m above the ground level by using a lift, whereas the height of the MS was set at a pedestrian height of 1.65 m. Some lamp-posts, road signs, and other urban furniture were distributed along the route while some cars and basketball signs were present on the parking area. The surrounding buildings are residential and commercial and they are mostly made of cement block, tiles and glass surfaces. Furthermore, one small electrical box made of cement and located near the MS1 and MS2 has a height of around 2 m while another one which is a parking bike made of cement block with a height of around 3 m was located near the building A and C.

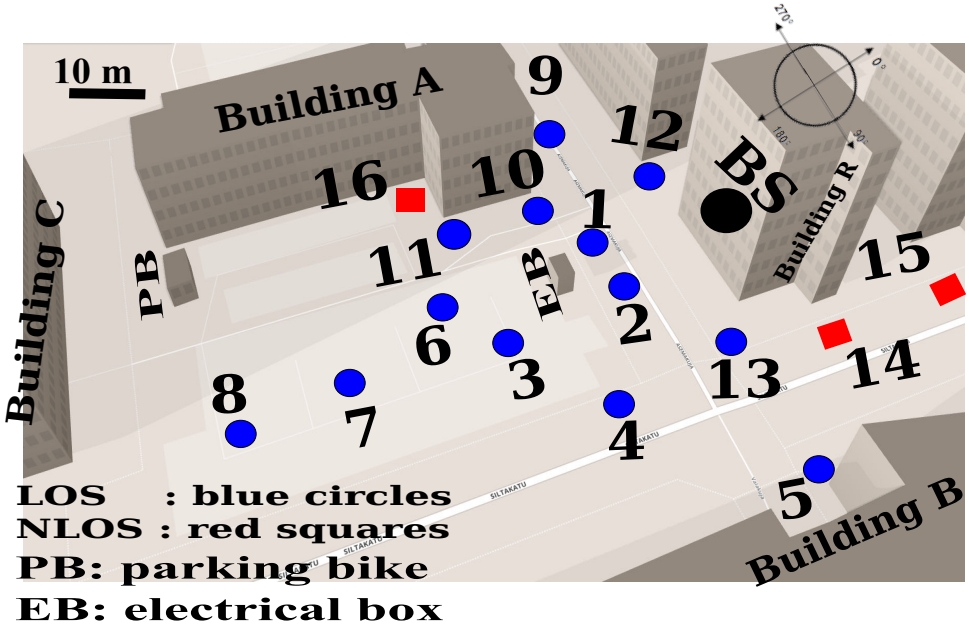

Figure 3.15.: Map of the UMi obtained from Open Street Map building (https://osmbuildings.org). Cars, pedestrians, trees, pillars and lamp-posts are not presented here. The blue circles and red squares are MS positions.

The heights of the surrounded buildings are in the range of 11 and 34 m. A rotation scan of the BS antenna over 225° (from 45° to 270° defined within clockwise convention) with a step of 5° in azimuth at the BS side was performed while a down-tilt of 10° was set corresponding to a typical UMi deployment. We can observe that the considered UMi environment presents key similarities with the reference environment of the METIS map-based model, so-called the Madrid grid [14]. Both the UMi and the Madrid grid are urban environments and relatively flat and inhomogeneous building heights. Furthermore, regularly spaced buildings and a flat parking area are features of both measurement sites.

Table 3.7.: Rough description of the MS location in LOS configurations in *Meas.*3.

MS	[**Lat.**; **Lon.**] [m]	**Observations**
MS1	[60.204447; 24.659151]	Placed near the small building box. Some road-signs were near the MS location.
MS2	[60.204337; 24.659247]	Placed near the small building box where a lamp-post was near the MS location.
MS3	[60.204305; 24.658927]	Placed on the open parking where cars, metallic basketball panels and road-signs were surrounded the MS location.
MS4	[60.204152; 24.659152]	Placed on the street way where trees, road-signs and lamp-post were near the MS location.
MS5	[60.204062; 24.659786]	Placed near the window of building B where one road-sign and lamp-post were near the MS location.
MS6	[60.204342; 24.658725]	Placed on the open parking where cars, metallic basketball panels and road-signs were surrounded the MS location.
MS7	[60.204257; 24.658537]	Placed on the open parking where cars, metallic basketball panels, and road-signs were surrounded the MS location.
MS8	[60.204161; 24.658241]	The farest LOS link. The MS was placed on the open parking area where cars, metallic basketball panels, and road-signs were surrounded the MS location.
MS9	[60.204601; 24.659071]	Placed near the wall of building A where some bushes and lamp-post were near the MS location.
MS10	[60.204534; 24.658993]	Placed near the wall of building A at around 1.5 m. Some road-signs and lamp-posts were near the MS location.
MS11	[60.204473; 24.658694]	Placed near the wall of building A at around 1.5 m. Some road-signs and lamp-posts were near the MS location.
MS12	[60.204593; 24.659296]	Placed near the building R were some bushes, lamp-posts and cars were present.
MS13	[60.204293; 24.659650]	The shortest LOS link. The MS was placed near the building R and a lamp-post and road-signs were near the MS location.

A total of 16 BS-MS links was measured; 13 in LOS conditions and 3 in NLOS with a link distance ranging from 15 m to 80 m. One outage position[4], MS16 which was located behind the corner of Building A. Table 3.7 provides a rough description of the MS locations and some photos of the are shown in Fig. 3.16.

[4]Meaning no signal was recorded.

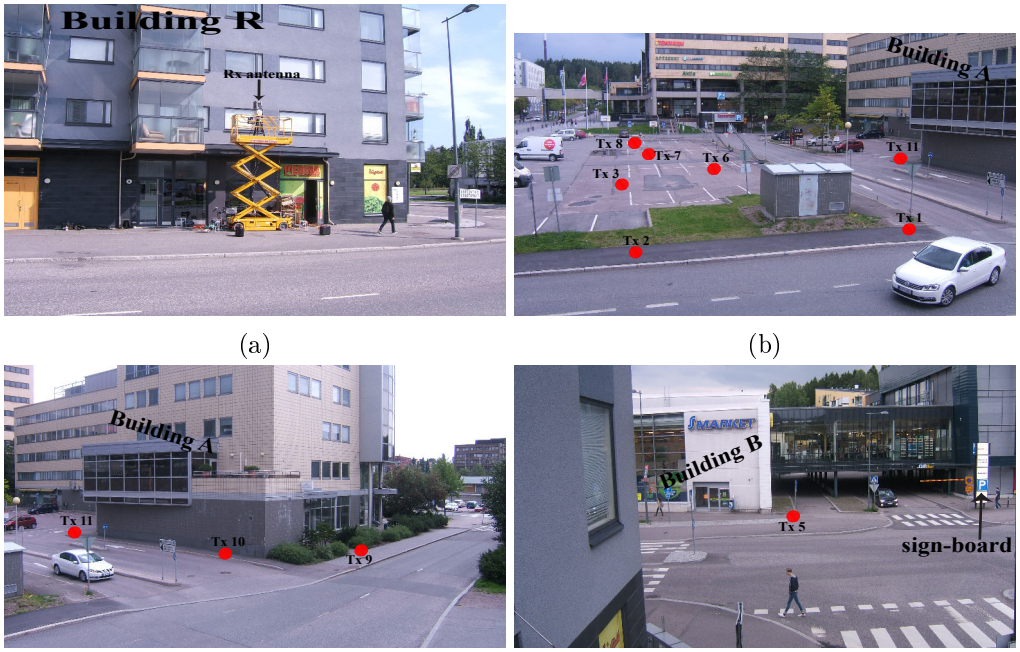

Figure 3.16.: Photos of the measurement site of the UMi. In (a), the position of the BS antenna mounted on the lift at a height of 6 m above the ground and located near the building R made mostly by cement block with a rough surface and windows glass. (a), (b) and (c) shows the overview of the investigated measurement. Some positions of the MS antennas are illustrated with the parking area, lamp-posts, road-signs, cars, people, trees, bushes. Building A is made essentially with tiles, while building B is constituted by rough wall and windows glasses are shown in (d).

3.3.5.3. UMi Data Analysis

In this study, only LOS situations are addressed. An example of the fine peak detection applied to the link BS-MS9 where twenty of them were found is shown in Fig. 3.17. A sliding window length of 5 ns, meaning more than 8 times compared to the delay resolution of the channel sounder, was considered in the fine peak search while an additional th^{cst} of 5 dB chosen from the visual inspection of the CIR were considered in the fine peak search detection. When looking Fig. 3.17 and Fig. 3.18 that shows the CIR for the all link, one common observation is the presence of only a few discrete components (in both delay and angular domain) that are significant at 32.6 GHz in UMi. This observation is in line with the literature [34, 110, 111].

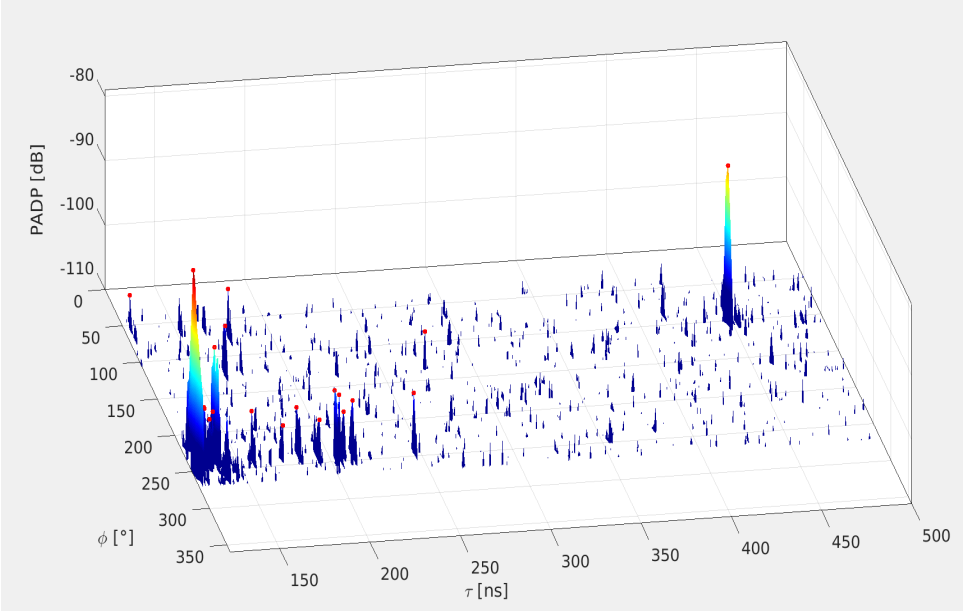

Figure 3.17.: Illustration of the fine peak search detection applied to the link BS-MS9. The detected peaks are in red dots

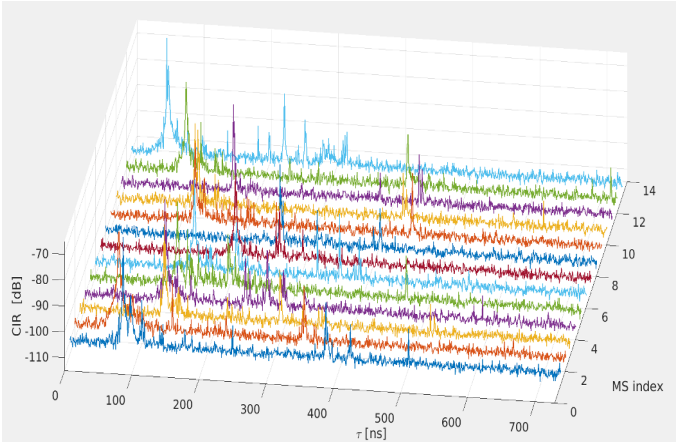

Figure 3.18.: Illustration of the sparsity of the 32 GHz: the all LOS links are plotted.

Furthermore, we observed that the all measured PDPs did not contain a clear diffuse scattering. A possible explanation would be the limited dynamic range of the channel sounder which does not allow to reveal the diffusion scattering effect from the scattering environment. Next, a method to investigate the scattering environment is presented.

3.3.6. `back-projection`: Single Bounce Geometrical Transformation

In order to make visible the effects of scatterers in the UMi from the estimated data which has been derived from the fine peak search detection, we propose a simple geometrical transformation which establishes an one-to-one mapping between the estimated delay and azimuth angle and a given point in the 2D coordinate system. The original problem is three dimensional but the mapping is performed in two dimensional because of the single azimuth angular axis available at the BS side.

3.3.6.1. Problem Formulation

Let

$$\mathbf{p}_{MS} = [x_{MS}, y_{MS}, z_{MS}]^T$$
$$\mathbf{p}_{BS} = [x_{BS}, y_{BS}, z_{BS}]^T$$
$$\mathbf{p}_l = [x_l, y_l]^T$$

denoting respectively the positions of the MS, the BS and a given scatterer expressed in the global reference frame of the scene that we want to determine. Notice that $\mathbf{p}_{MS}$ and $\mathbf{p}_{BS}$ are known from the measurement site and $\mathbf{p}_l$ is the position of the l^{th}scatterer. We consider the single bounce assumption meaning that the path is resulting from the 1^{st} order SR from the scatterer localized in position $\mathbf{p}_l$ and assumed in fixed position as shown in Fig. 3.19.

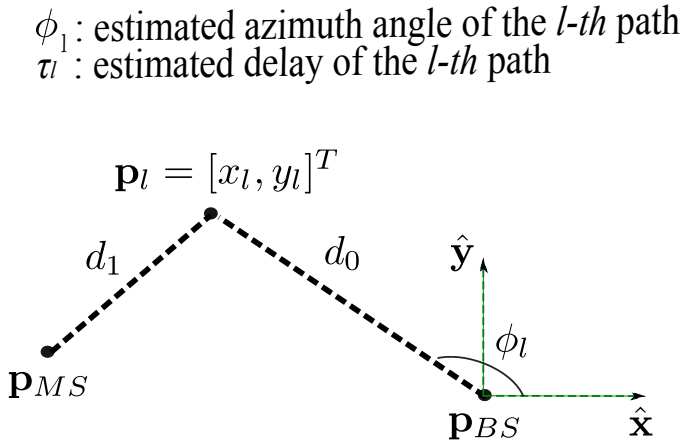

Figure 3.19.: `back-projection`: single bounce assumption.

The assumption of the single bounce is simple but makes sense in mm-wave since assuming that most of the energy comes from the LOS and 1^{st} order SR.

The idea is to have a rough estimation of $\mathbf{p}_l$ that places the energy in the 2D map of the propagation environment by relating the paths characterized in angle and delay information to the map geometry. Since the delay and the azimuth angle for each path

are derived from the fine peak search, the `back-projection` method consists of mapping the estimated set of (τ_l, ϕ_l) with the (x_l, y_l) by minimizing the Eq. 3.1

$$x_l, y_l = \min_{x,y}(||d_0(x,y) + d_1(x,y) - c\tau_l||_2 + ||\phi(x,y) - \phi_l||_2) \tag{3.1}$$

with,

$$\mathbf{p} = [x, y]^T$$
$$d_0(x,y) = ||\mathbf{p} - \mathbf{p}_{BS}||_2$$
$$d_1(x,y) = ||\mathbf{p}_{MS} - \mathbf{p}||_2$$
$$\phi(x,y) = \text{atan2}\left((\mathbf{p} - \mathbf{p}_{BS}).\hat{\mathbf{y}}, (\mathbf{p} - \mathbf{p}_{BS}).\hat{\mathbf{x}}\right)$$

where where $||.||_2$ denotes the Euclidean distance, d_0 and d_1 are respectively the distance between the MS and the scatterer and the distance between the scatterer and the BS.

3.3.6.2. `back-projection`: Results

Fig. 3.20 and Fig. 3.21 displays the output of the `back-projection` method applied to links BS-MS10 and BS-MS3. The color-scale of circles represents the intensity of the MPCs level power.

Fig. 3.20 and Fig. 3.21 demonstrate that the most of the energy comes from the wall and the window of the surrounded buildings. For instance, Fig. 3.20 shows a strong 1^{st} order SR from the wall of the building A. This is expected since the MS10 was placed around 1.2 m. Furthermore, the window of building B is observed to deliver significant energy as well as the publicity-board located near the window of the building B as shown in Fig. 3.21.

Besides the buildings, ground-floor and the publicity-board that are found to be important, we found that the energy was delivered by metallic lamp-post and sign-road. Indeed, by exploiting the photos of the measurement site and relating them to the `back-projection` method, we noticed that some paths were coming from to some road-sign and lamp-post as shown Fig. 3.20 and Fig. 3.21, showing the non negligible contribution from such metallic scatterers. Notice that a large representation of the `back-projection` results applied to the all links is given in Appendix B.

3.3.6.3. Discussion

The `back-projection` method shows that paths with the significant energy are originated from big scatterers (building wall, building window) but also from urban furniture distributed uniformly around the UMi environment. Some of such scatterers reflect a strong energy to a MS located far from the BS by SR mechanism. Such paths arrived late in the delay domain with a strong power level. The observed phenomenon can be explained as follow. Assuming a planar reflector object, its effective cross section is proportional to the inverse of the square of the wavelength: the smallest the wavelength, the largest the

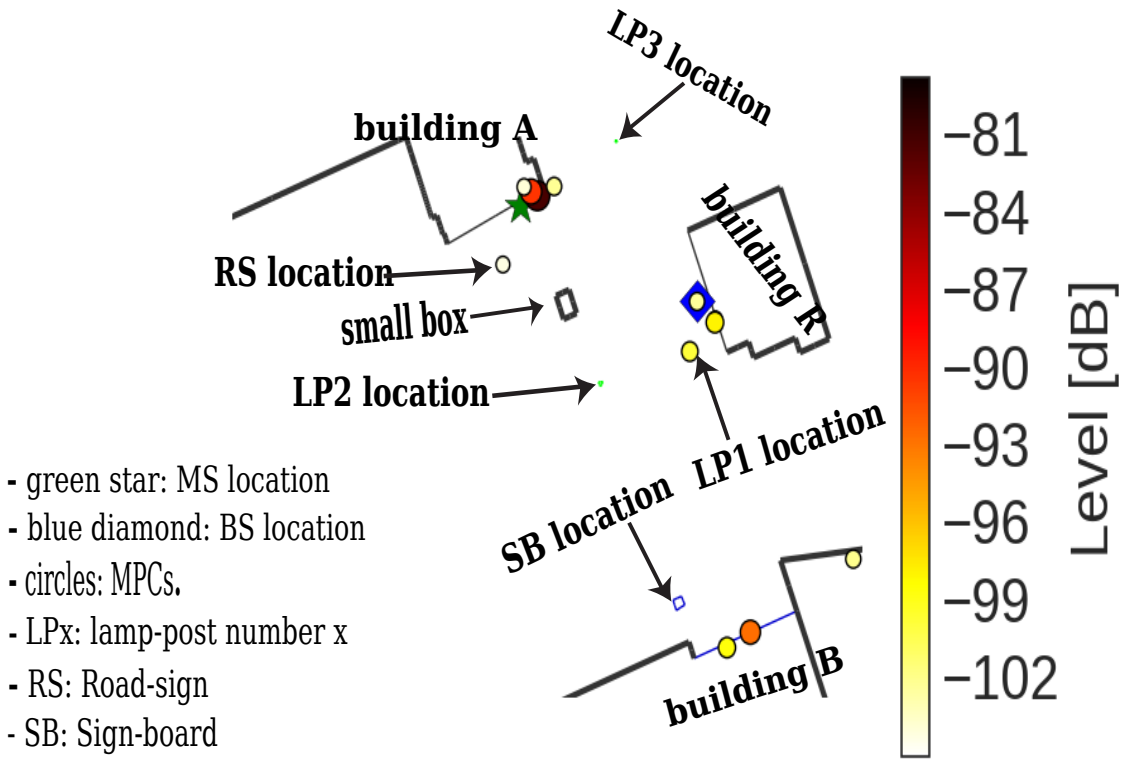

Figure 3.20.: `back-projection` applied to link BS-MS10

effective cross-section. Considering the mm-wave situation where the wavelength is small and considering a short propagation distance, the effective cross-section can be large even with relatively small objects. Therefore, such a planar surface can *flash* the energy in a very directive manner and hence probably explaining the observed phenomenon.

Practically, considering the downlink case, having such an effect could constitute a benefit since in a case where the LOS is obstructed, the BS could communicate with the MS through an alternative path. Moreover, the capacity of the user can be increased by taking advantage the diversity of the channel produced by the scatterers. Furthermore, in the localization point of view, this may improve the robustness of algorithms by including the effect of the scatterers. In addition if we think about an user located in NLOS position meaning there is no visibility between the BS and the MS. In such case, the operator can save money by exploiting existing urban furniture as a relay to serve such an user without investing more money in deploying another BS.

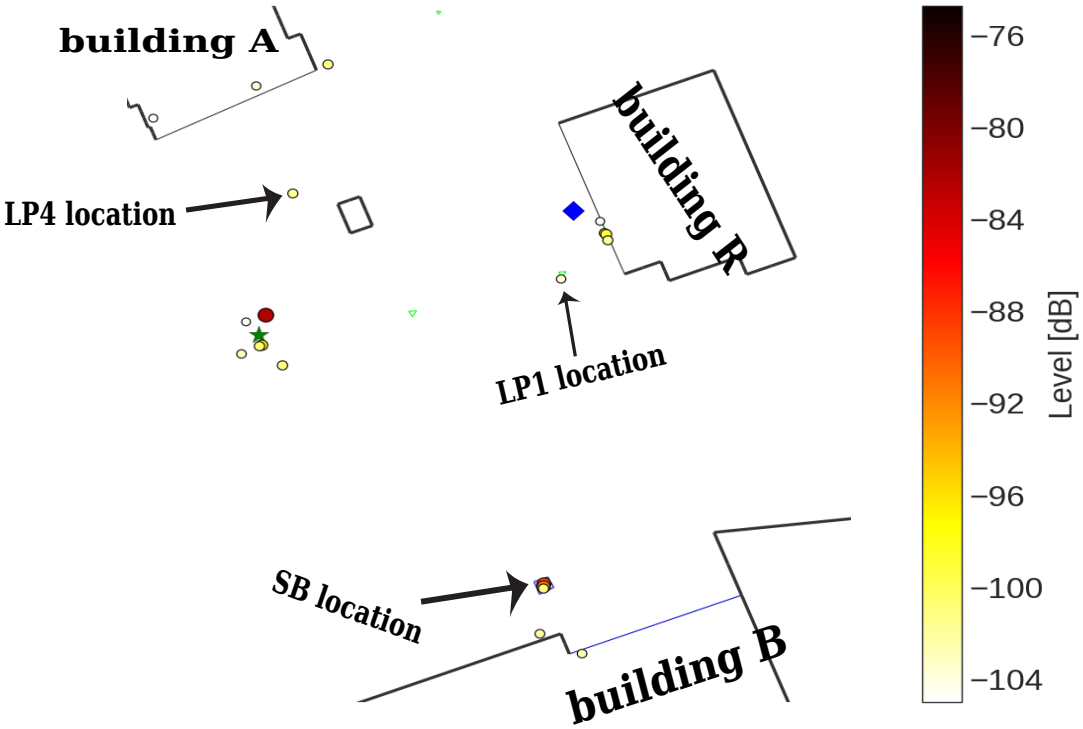

Figure 3.21.: `back-projection` applied to link BS-MS3

3.4. Summary

Providing accurate and repeatable results are required in the development of the channel model framework. This challenge can be tackled by performing a radio channel sounding that captures the reality of the radio channel constituting the starting point. An overview of the radio channel sounding approaches in cm- and mm-wave is presented in this chapter. The main motivations for conducting measurements were to study the time variability and the scattering environment effect in the mm-wave radio channel. A total of four measurement campaigns carried-out in various representative propagation scenarios covering InH and outdoor scenarios and performed at different frequency bands were described. *Meas*.0 and *Meas*.1 were performed in an outdoor and InH scenarios at 28 GHz. The mobility configuration is investigated in a way that the BS was in a fixed position while the MS was moving across different trajectory. *Meas*.2 performed in multi-frequency (15, 28 and 83 GHz) in a conference room and *Meas*.3 conducted in an UMi environment at 32.6 GHz were addressed in a configuration where the BS and the MS antennas were in a static position.

Meas.0 was considered as a failure due to the measurement error. *Meas*.1 was successfully conducted and the 28 GHz dynamic channels in InH scenario were presented. The channel time-variant at this band was found to be rich by exhibiting coherent MPCs mostly led by SR mechanism. In addition, the observed time-variant channel in the office

room was found to contain more dense MPCs compared to the one in the library. This effect was attributed to the reverberation effect which is more pronounced in the office room presenting a small volume compared to the library. Furthermore, an analysis of the LSPs was provided and a dependency between LSPs is noticed.

The dissemination of $Meas.2$ revealed the consistency of the channel as the MS is moving and the frequency is changing.

The analysis of $Meas.3$ does not highlight a clear effect of the diffuse scattering while the LOS and the SR mechanism were found be significant. Moreover, a method to investigate the effect of the scatterers in the UMi environment was proposed. The proposed method shows that the significant contributions were mostly originated from the window building and the publicity-board. Furthermore, urban furniture such as metallic lamp-posts, road-signs were found to deliver non negligible energy. The data gathered in $Meas.2$ and $Meas.3$ will be used in the next chapter for comparison purposes against the RT.

Chapter 4

RT vs Measurements: Comparisons

The measurements data acquired in the previous chapter and which have been presented so far was to calibrate our own site-specific ray tracing simulator in order to make it suitable for further communication and localization mm-wave simulation networks. Among the pending questions was the capability of the ray tracer to provide close reproduction of the measured channel in mimicking as realistically as possible the measurement protocol used for the data acquisition. Furthermore, measured data are used to identify what is missing and what should be added in the later version of the tool for improving its prediction capabilities.

4.1. Description of the Ray Tracing Tool

The RT tool used in this thesis namely PyLayers was developed in [112, 57, 113]. The RT is a radio propagation open source simulation platform implemented in Python computer language. The RT is exploiting an original graph-based description of the environment which facilitate the time consuming task of finding rays for each radio link. The modeling approach of the RT tool is discussed next.

4.1.1. The Graph-Based Approach for Ray Tracing

4.1.2. Layout Description

The first step consists in creating the radio propagation environment. This can be done via a dedicated editor or from the Open Street Map database `OSM` [114]. `OSM` is an open project aiming to gather a free geographical database of the world based on crowd-sourcing principles. The gathered data are coming from a collaborative effort from the community that can review and improve the accuracy of the data. The information related to the height, profile, nature of the buildings can be extracted. The RT supports `OSM` format file and a Java editor for `OSM` (`josm`) is used for editing the layout. In the

measurement campaign point of view, using such a tool might be useful since database can be updated and measurement site can be also improved by filling directly the OSM database with the collected information. From the OSM file where points coordinates are georeferenced and expressed with their latitude and longitude, this data is transformed in a more suitable file format which is specific to the RT tool where points are expressed in a metric system. As an illustration an extraction of the layout description file used in the RT for a description of the UMi environment is listed below.

```
[info]
format = cart
version = 1.3
type = outdoor

[points]
-2 = (19.728, 175.537)
-274 = (261.676, 191.27)
-273 = (264.003, 192.186)
-272 = (264.886, 189.944)

....

[segments]
1 = {'name': 'WALL', 'connect': [-58, -57], 'z': [0, 11.32]}
2 = {'name': 'WALL', 'connect': [-56, -57], 'z': [0, 11.32]}
3 = {'name': 'WALL', 'connect': [-60, -59], 'z': [0, 11.32]}
4 = {'name': 'WALL', 'connect': [-59, -58], 'z': [0, 11.32]}
5 = {'name': 'WALL', 'connect': [-62, -61], 'z': [0, 11.32]}

...

[slabs]
WALL = {'color': 'grey20', 'linewidth': 3, 'lthick': [0.5], 'lmatname': ['CONCRETE_ITU']}
WINDOW_GLASS = {'color': 'blue3', 'linewidth': 1, 'lthick': [0.01], 'lmatname': ['GLASS_ITU']}
AIR = {'color': 'white', 'linewidth': 1, 'lthick': [0.1], 'lmatname': ['AIR']}
FLOOR = {'color': 'grey40', 'linewidth': 1, 'lthick': [0.7], 'lmatname': ['CONCRETE_ITU']}
...


[materials]
CONCRETE_ITU = {'mur': (1+0j), 'epr': (5.31 + 0j), 'roughness': 0.0, 'sigma': 0.5472}
AIR = {'mur': (1+0j), 'epr': (1+0j), 'roughness': 0.0, 'sigma': 0.0}
GLASS_ITU = {'mur': (1+0j), 'epr': (6.27 - 0.0j), 'roughness': 0.0, 'sigma': 0.2741}

...

[latlon]
llcrnrlon = 24.655478712
llcrnrlat = 60.2027508052
urcrnrlon = 24.661677531
```

```
urcrnrlat = 60.2054631924
```

The layout description is made of 5 main sections. The first section `info` provides information about the current file format and type of simulation (indoor or outdoor scenario). The `points` section is a list of points and their coordinates in the plane are expressed in meters. The `segment` section provides the connection information between points and also information about slab nature and height of the segment (z_{min},z_{max}). The two remaining sections enumerates the slabs and the materials used for this environment. The important information about the slab is the multilayers structure in terms of thickness `lthick` and materials `lmatname`. The `latlon` section saves the latitude and longitude of the region for being able to go back and force from metric to latitude longitude coordinates system through the specified geographic projection, also precise in this section. Basically, walls are assumed to be regular and flat with an associated material properties and thickness.

4.1.3. Building Graphs Associated to the Layout

Second, a chain of four graphs characterized by a set of vertex ($\mathscr{V}$) and edge ($\mathscr{E}$) is derived from the previous layout:

- the graph of structure ($\mathscr{G}_s(\mathscr{V}_s,\mathscr{E}_s)$),
- the graph of convex cycles ($\mathscr{G}_t(\mathscr{V}_t,\mathscr{E}_t)$),
- the graph of visibility ($\mathscr{G}_v(\mathscr{V}_v,\mathscr{E}_v)$),
- the graph of interactions ($\mathscr{G}_i(\mathscr{V}_i,\mathscr{E}_i)$).

$\mathscr{G}_s(\mathscr{V}_s,\mathscr{E}_s)$ and $\mathscr{G}_t(\mathscr{V}_t,\mathscr{E}_t)$ are dedicated for the description of the environment while $\mathscr{G}_v(\mathscr{V}_v,\mathscr{E}_v)$ and $\mathscr{G}_i(\mathscr{V}_i,\mathscr{E}_i)$ are dedicated for the search of the ray `signatures`[1]. For simplicity, the set of vertices and edges will be omitted in the writing of the graphs. $\mathscr{G}_s$, $\mathscr{G}_t$ and $\mathscr{G}_v$ are non oriented graphs while $\mathscr{G}_i$ is an oriented graph.
$\mathscr{G}_s$ describes the structure of the layout by delimiting the simulated area of the environment characterized by the set of nodes representing the `segment nodes` or vertex points (`point nodes`) and the edges stating for the link connection between two vertex points. A node is considered as a `point nodes` if the index value is negative while it is considered as `segment nodes` if the index value is positive.
$\mathscr{G}_t$ defines the graph of convex cycles built from $\mathscr{G}_t$. $\mathscr{G}_t$ introduces the `convex cycle` notion referring to a convex closed circuit[2] connecting different `points`. `Convex cycles` are obtained after a Delaunay triangulation where triangles are merged until the resulting region remains convex. Convexity is a useful property which guarantees that all entities of the cycles *see* every one else.

[1] Accordingly to [112] a `signature` is defined as a sequence of interactions (associated to a PM) which allows to build a ray once Tx and Rx position are known

[2] i.e. starting and ending at the same point.

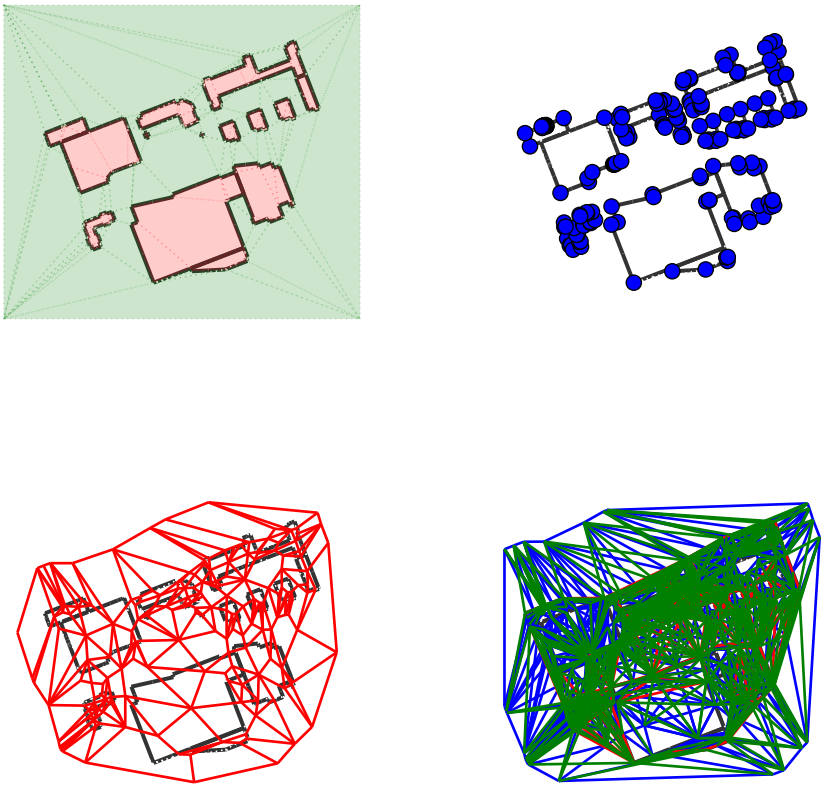

Figure 4.1.: Illustration of $\mathscr{G}_s$ (upper left corner), Diffraction points in outdoor (upper right figure), $\mathscr{G}_t$ (lower left figure) red lines are connection between `convex cycles`, $\mathscr{G}_v$ (lower right figure) encoding visibility between points and segments

Fig. 4.1 shows an example of a layout illustrating $\mathscr{G}_s$ and $\mathscr{G}_t$. The white circles with a positive value denote the `segment nodes` while the grey circle with negative values are the `vertex nodes` of $\mathscr{G}_s$ and each of nodes is linked by the edges stating for a `segment`. In the red square the cycle from $\mathscr{G}_t$. In this example, the cycles represent a room containing the coordinate position system of the MS and the BS while `segments` are walls having electrical properties with a thickness. $\mathscr{G}_v$ is the first step to describe the electromagnetic pathways. $\mathscr{G}_v$ describes the all possible visible nodes (`segment nodes`, `point nodes`) of $\mathscr{G}_s$ in a way that each node see each other. Introducing $\mathscr{G}_v$ by exploiting the convexity of $\mathscr{G}_t$ nodes takes advantage of the graph sparsity and therefore reducing the combinator exploration of the graph.

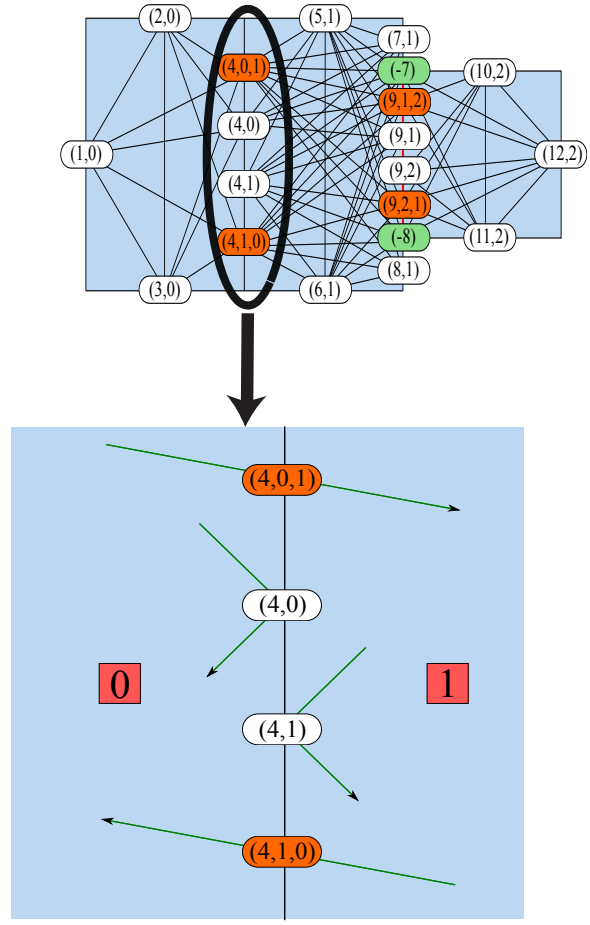

Figure 4.2.: Illustration of $\mathscr{G}_i$ from [113].

$\mathscr{G}_i$ is a graph of interactions[3] which captures all the possible transition between each interaction. As an example, Fig. 4.2 illustrates $\mathscr{G}_i$[4]. In Fig. 4.2, the white ellipses with two values state for a `segment nodes` yielding a SR mechanism. The orange ellipses with three values denote a `segment nodes` yielding a transmission mechanism and the green ellipses with one negative value state for a `segment node` that originates a diffraction mechanism and the edges between nodes state for the pathway of the `interactions`. The bottom figure of Fig. 4.2 is a zoom of the `segment node` number 4 illustrating the four possible existing `interactions` associated to segment $\mathscr{G}_i$: the transmission over the `segment node` number 4 originated from the cycle number 0 and going to the cycle number 1 ((4,0,1)) , the SR over the `segment node` number 4 originated from the cycle number 0, ((4,0)), the SR over the `segment node` number 4 originated from the cycle number 1 ((4,1)) and the transmission over the `segment node` number 4 originated from

[3]By interactions, we refer transmission, reflection and diffraction mechanisms
[4]Including $\mathscr{G}_s$ and $\mathscr{G}_t$

the cycle number 1 and going to the cycle number 0 ((4,1,0)).

4.1.4. Determination of Signatures

Once the `convex cycles` of the Tx and Rx are known, an exhaustive search of the all potential pathways going from the MS's cycle to BS's cycle is performed. The output of the exhaustive search state for `signatures`. `Signatures` give information about where the paths come from by providing information about the number of `segments`, the type of the `interaction` and the associated materials. From that, a search of the associated interaction node is performed from the source cycle where the MS is located to the targeted cycle where the BS is placed. Therefore, all the couple of interactions connecting the MS and the BS are found in $\mathscr{G}_i$. To limit the combinatoric explosion of the $\mathscr{G}_i$ exploration during the exhaustive search of `signatures`, a verification of the geometry feasibility of the interaction sequence is checked in updating the illumination cone as the graph exploration of the graph moves forward. The parameter γ_{RT} which is a ratio between the angle formed by the apex and the N^{th}-`segment` (α_2) and the one formed by the apex and the $N-1^{th}$-`segment` (α_1) is maintained all along the graph exploration as illustrated in Fig. 4.3. If this quantity is 0 it means that the interaction is not possible accordingly to the geometry and if the quantity is equal to one then the current interaction is fully illuminated by the cone and therefore maintaining. If $0 < \gamma_{RT} < 1$, the segment can potentially be illuminated but with a certain probability. Therefore, a threshold can be specified to accelerate the search of paths and only path fulfilling $\gamma_{RT} > \gamma_{th}$ are kept.

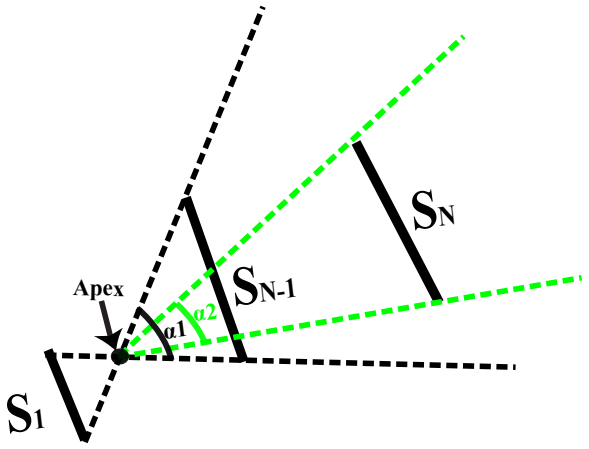

Figure 4.3.: Illustration of the γ_{RT}'s determination in the RT tool. The apex of the cone is constructed between the first `segment` (S_1) and the $N-1^{th}$-`segment` (S_{N-1}).

As the `signatures` contain all the geometrical information for the defining sequence of `interaction`, the 2D ray from the MS belonging to the starting cycle to the BS belonging to the ending cycle is calculated accordingly to the image principle method.

Since no floor and ceil are taken into account in the determination of the 2D ray, the

2D ray is extended to a 3D ray as follows. First, the extension is performed by founding the relative position of the impact point when the ray interacts with the material of the floor or ceil in the frame coordinate (O, z, s). The output of the 3D ray is a set of parameters including the type of the interaction, the evolved material, the DoD and DoA. The interactions obtained by the SR mechanisms are determined based on the geometrical optic principle, the diffraction interaction are modeled with the UTD model. After deriving the 3D ray, rays presenting the same interaction are treated as a data block and interaction coefficients and losses are computed and applied to the data block at once.

4.1.5. Evaluation of PM Coefficients

4.1.5.1. Specular Reflection and Transmission Coefficients

The coefficients of the transmitted and reflected field modeled in the RT are following the multilayer dielectric structure implementations in [115]. Fig 4.4 shows an example of the reflected and transmitted coefficient when considering an air-glass interface. The evaluation was done at 32.6 GHz and the material properties of the glass are following the recommendation of the ITU-R P.2040-1.

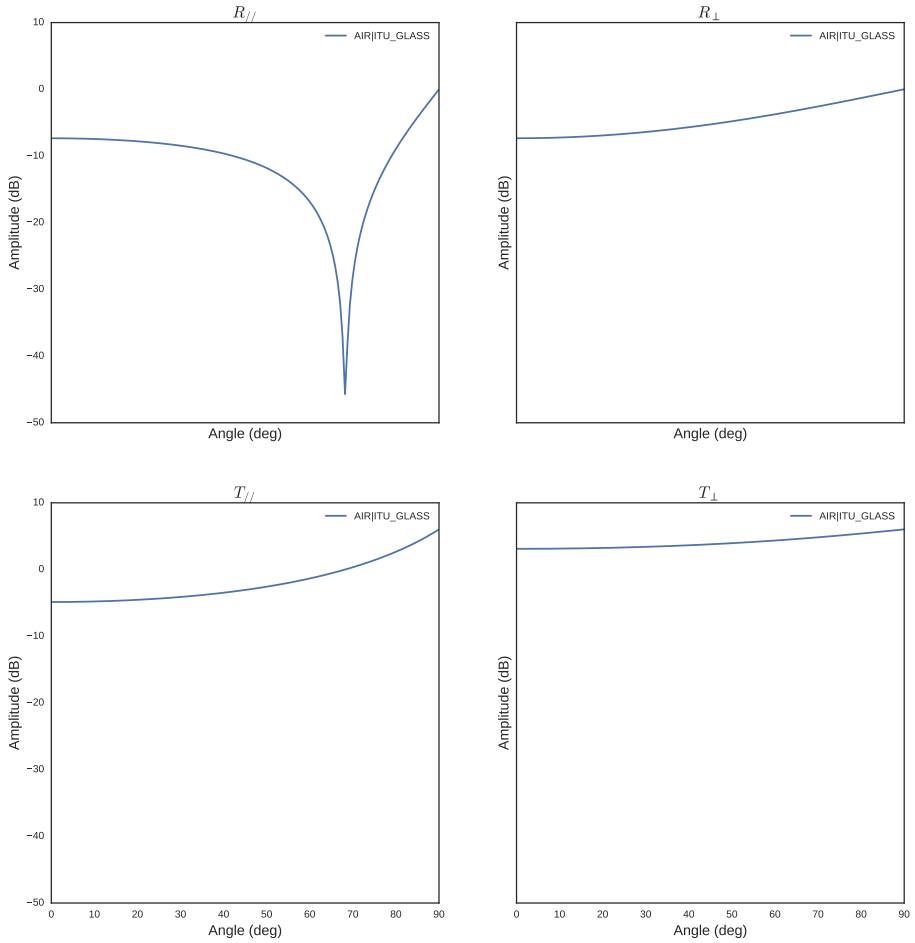

Figure 4.4.: Reflected and transmitted coefficients evaluated by PyLayers at 32.6 GHz.

4.1.5.2. Diffraction Coefficients

The diffraction mechanism considered in the RT is using the two dimensional UTD diffraction coefficients reported in [116]. As an example, the output of a metal diffraction evaluated by PyLayers at 2.4 and 32.6 GHz are displayed in Fig. 4.5.

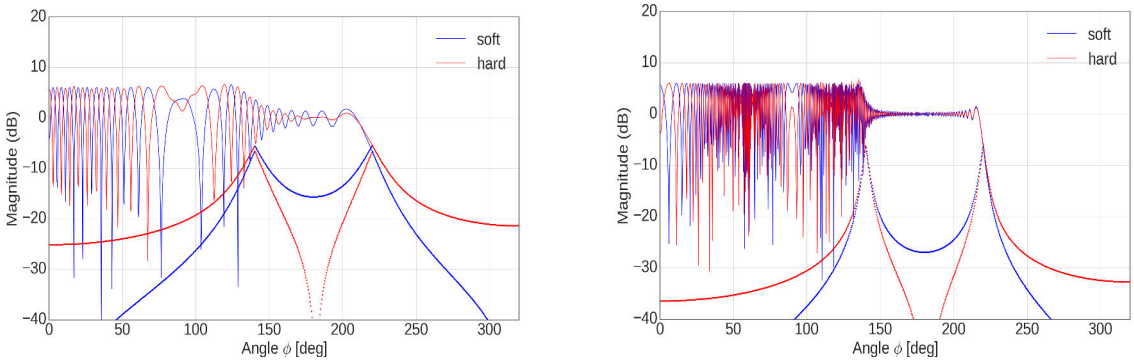

(a) RT: diffraction mechanism evaluated at 2.4 GHz (b) RT: diffraction mechanism evaluated at 32.6 GHz

Figure 4.5.: RT implementation illustration of the diffraction over a metal provided by the RT evaluated at 2.4 and 32.6 GHz.

It can be observed that the slope of the hard diffraction curve (red line) in the incidence shadow boundary region (after 220°) is strongly decreasing when going in higher frequency while the attenuation can reach up to 32 dB.

4.1.6. Sectoral Aperture Horn Antenna Pattern: Implementation

The horn antennas used in *Meas.*2 and *Meas.*3 are implemented in the RT. The considered antenna is a horizontal plane sectoral aperture horn implemented from [117]. Assuming the horn as a radial wave-guide and designed in vertical polarization, the electrical aperture field can be approximated as

$$E_y = \cos(\frac{\pi X}{a_1}) exp.[\frac{-j}{2} k(\frac{X^2+Y^2}{\rho_1})], \tag{4.1}$$

where $k = \frac{2\pi}{\lambda}$ and $X = [\frac{-a_1}{2} : \frac{a_1}{N_x - 1} : \frac{a_1}{2}]$ and $Y = [\frac{-b_1}{2} : \frac{b_1}{N_x - 1} : \frac{b_1}{2}]$ are the aperture range points over where the antenna is defined and N_x and N_y are constants. The equivalent current density can be derived as

$$J_y = \frac{E_y}{\epsilon_0}, \tag{4.2}$$

with $\epsilon_0 = 377\ \Omega$ denotes the free space impedance. From that, the radiated field antennas in the elevation and azimuth planes can be expressed as

$$E_\theta = -(L_\phi + \epsilon_0 N_\theta),\ E_\phi = L_\theta - \epsilon_0 N_\phi, \tag{4.3}$$

where

$$\begin{cases} N_\theta = \int_{N_x} \int_{N_y} [J_y \cos\theta \sin\phi] exp.(jk(X \sin\theta \cos\phi + Y \sin\theta \sin\phi))\, dN_x dN_y, \\ N_\phi = \int_{N_x} \int_{N_y} [J_y \cos\phi] exp.(jk(X \sin\theta \cos\phi + Y \sin\theta \sin\phi))\, dN_x dN_y, \\ L_\theta = \int_{N_x} \int_{N_y} [E_y \cos\theta \sin\phi] exp.(jk(X \sin\theta \cos\phi + Y \sin\theta \sin\phi))\, dN_x dN_y, \\ L_\phi = \int_{N_x} \int_{N_y} [E_y \cos\phi] exp.(jk(X \sin\theta \cos\phi + Y \sin\theta \sin\phi))\, dN_x dN_y. \end{cases} \tag{4.4}$$

Worthy recall that Eq. 4.3 and Eq. 4.4 are derived from the Balanis book's [117]. Table 4.1 summarizes the dimensions of the implemented antennas at 15, 28 and 83 GHz where ρ, a and b are respectively the sectoral radius and the rectangular dimensions ($a > b$) of the horn antenna. The electrical parameters of the aperture horn antenna provided by the manufacturer allow to have the same HPBW for the all frequency bands while having the same antenna gain of 19 dB.

	ρ_1 [m]	a_1 [m]	b_1 [m]
15 GHz	0.41	0.16	0.024
28 GHz	0.198	0.088	0.0126
83 GHz	0.0717	0.0264	0.0044

Table 4.1.: Horn dimensions

Furthermore, Fig. 4.6 illustrates the results of the radiation patterns implemented in PyLayers. The antenna patterns were implemented for a values of $N_x = N_y = 100$.

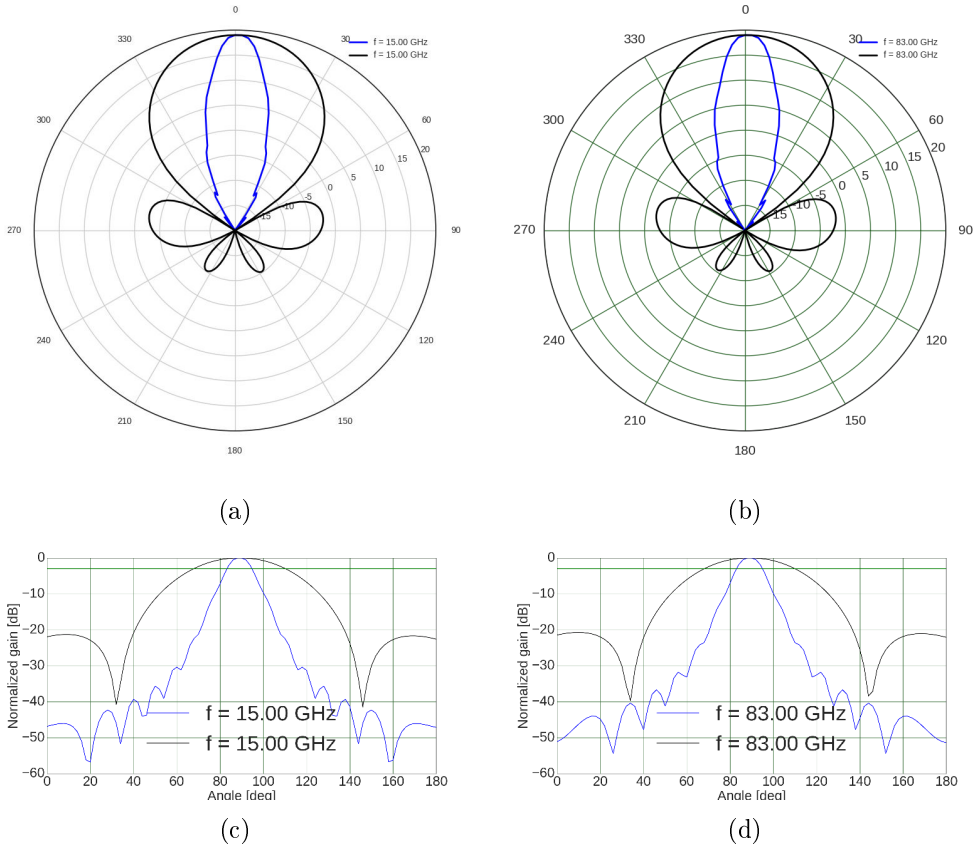

Figure 4.6.: Illustration of the radiation pattern of the horn antenna implemented in PyLayers. The blue line denotes the azimuth plane while the black line represents the elevation plane.

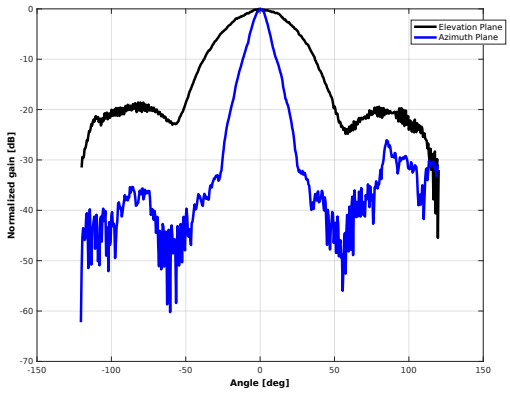

Figure 4.7.: Azimuth and elevation plane measured at 27.5 GHz by the manufacturer.

A perfect matching w.r.t the radiation patterns is obtained at the three frequencies. The comparison between the implemented antenna pattern and the measured antenna by the manufacturer at 27.5 GHz given in Fig. 4.7 GHz revealed a good agreement.

About the biconical antennas used during measurements, since an exact description of the biconical antenna was not provided, an omni-directional antenna with 2 dB of gain was used in PyLayers for the comparison purposes.

After evaluating rays and PM coefficients, the transfer response function of the radio channel can be computed by weighting ray by the antennas. In following, a simple demonstration of the RT use in four lines is provided.

```
from pylayers.simul.link import * # importing packages.
DL = DLink(L='defstr.lay')        # Building graphs, set parameter settings.
DL.eval()                         # Running the RT
DL                                # Informations about the deterministic link (DLink)

Link Parameters :
------- --------
Layout : defstr.lay

Node a
------
position : [ 7.5  2.5  1.2]  in cycle 5
Antenna : Omni
Rotation matrice :
 [[ 1.  0.  0.]
 [ 0.  1.  0.]
 [ 0.  0.  1.]]

Node b
------
position : [ 2.5  2.5  1.2] in cycle 2
Antenna : Omni
Rotation matrice :
 [[ 1.  0.  0.]
 [ 0.  1.  0.]
 [ 0.  0.  1.]]

Link evaluation information :
-----------------------------
distance :  5.000 m
delay : 16.667 ns
azimuth (a | b ) : 180.0 deg  | 0.0 deg
elevation (a | b ) : 90.0 deg |  90.0 deg
tilt (a |  b ) : 0.0 deg  | 0.0 deg
fmin (fGHz) : 2.4
fmax (fGHz) : 2.4
```

```
fstep (fGHz) : 0.0
Nf : 1
 Algorithm information :
------------------------------
cutoff : 1
threshold :0.8

DL._show3()                          # showing the 3D result the RT simulation
```

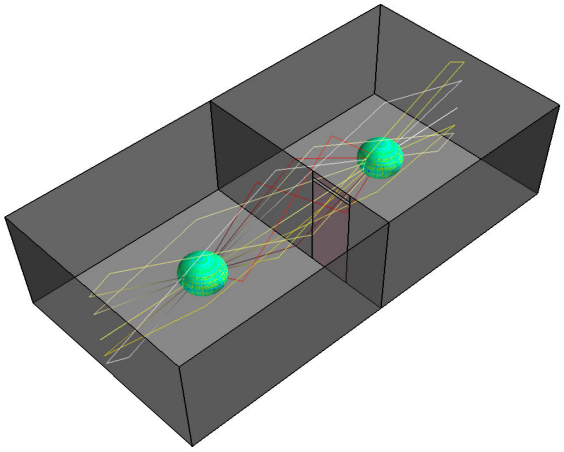

Figure 4.8.: Example of the RT simulation performed in InH at 2.4 GHz. Two omni-directional antennas were used.

As a summary, modeling the radio channel propagation by using the theory of graphs ensure to keep the RT robust while being efficient. However, the diffuse scattering mechanism is not supported in PyLayers to date.

The evaluation of the RT tool through *Meas.*2 and *Meas.*3 is discussed next.

4.2. RT vs *Meas.*2

4.2.1. RT: Conference Room Environment Description

A rough description of the conference room radio propagation environment is considered in the RT simulator. Indoor furniture such as chairs and table are not taken account in the RT. Walls and ground floor were considered as flat and were assigned as a concrete. Windows are assumed to be double glasses (glass-air-glass) while the ceil and doors were considered as a plasterboard and wood respectively. Table 4.2a, Table 4.2b and Table 4.2c report the electrical properties of the material considered in the RT.

	ϵ	σ_c [S/m]	Thick. [m]
wall	5.31	0.29	0.07
wood	1.99	0.087	0.04
floor	5.31	0.292	0.1
ceil	1.5	0.0117	0.1
door	1.99	0.087	0.04
window	6.27	0.107	0.01

(a) Material properties at 15 GHz.

	ϵ	σ_c [S/m]	Thick. [m]
wall	5.31	0.484	0.07
wood	1.99	0.167	0.04
floor	5.31	0.484	0.1
ceil	1.5	0.0241	0.1
wood	1.99	0.167	0.04
window	6.27	0.836	0.01

(b) Material properties at 28 GHz.

	ϵ	σ_c [S/m]	Thick. [m]
wall	5.31	1.167	0.07
wood	1.99	0.536	0.04
floor	5.31	1.166	0.1
ceil	1.5	0.085	0.1
door	1.99	0.536	0.04
window	6.27	0.836	0.01

(c) Material properties at 83 GHz.

Table 4.2.: Considered material properties of the conference room environment in the RT at the three frequency bands.

Notice that each material has a thickness and the estimated values of the relative permittivity and the conductivity are following the recommendation ITU-R P.2040-1.

4.2.2. Conference Room Simulation

Fig. 4.9 shows screen-shot examples of the RT performed in the conference room. Fig. 4.9a displays the 3D rays view while Fig. 4.9b illustrates the paths leaded through SR mechanism by the RT. The number of rays was reduced in Fig. 4.9b for plot visibility. The diffraction was turned off and the simulation time was around 10 seconds[5]. Furthermore, no noise was introduced in the processing of the simulated data.

[5] A HP Intel Core I7 with 32 Gb of RAM was used.

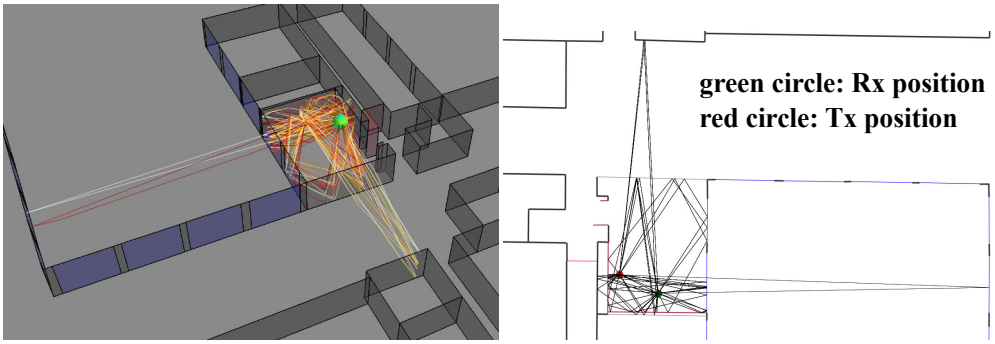

(a) BS-MS1: 3D rays view. (b) BS-MS1: 2D rays view.

Figure 4.9.: Screen-shots of the RT performed in the conference room. Only the LOS and the SR mechanisms are turned on.

Fig. 4.10, Fig. 4.11 and Fig. 4.12 show the comparison between the measured and the simulated data of the link BS-MS7 w.r.t the PADP and the PAP metrics at the 15, 28 and 83 GHz while the results of the comparison for the link BS-MS1 are provided in Fig. 4.13, Fig. 4.14 and Fig. 4.15.

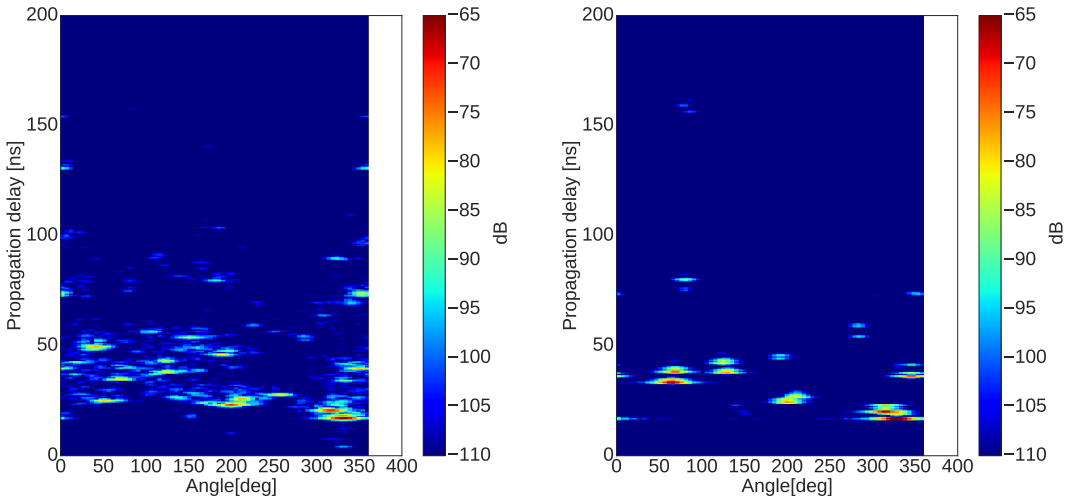

(a) BS-MS7: measured PADP at 15 GHz.

(b) BS-MS7: simulated PADP at 15 GHz.

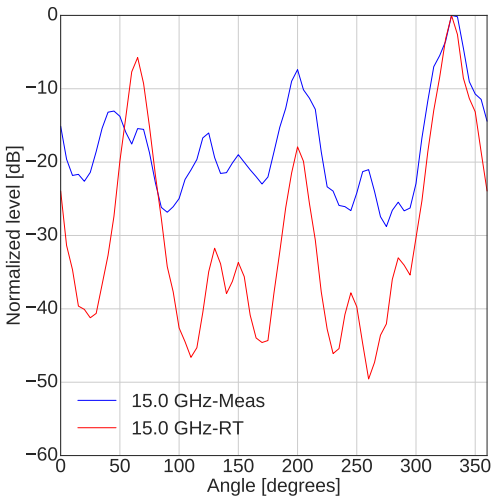

(c) BS-MS7: PAP comparison at 15 GHz.

Figure 4.10.: Comparison between the measured and simulated PADP and PAP of the link BS-MS7 at 15 GHz.

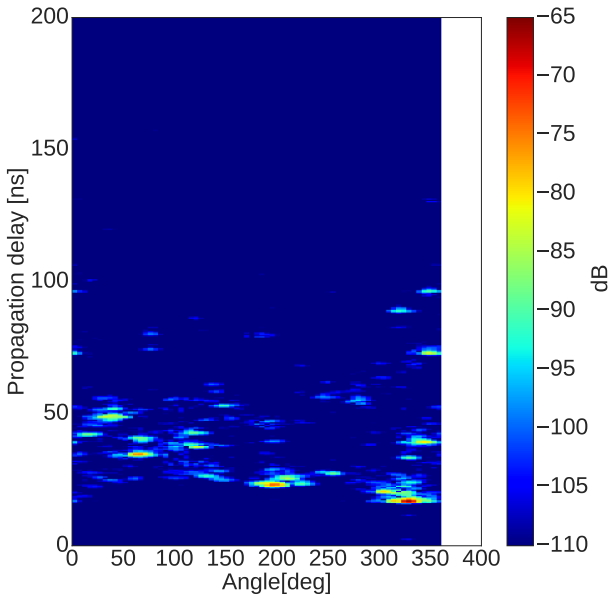

(a) BS-MS7: measured PADP at 28 GHz.

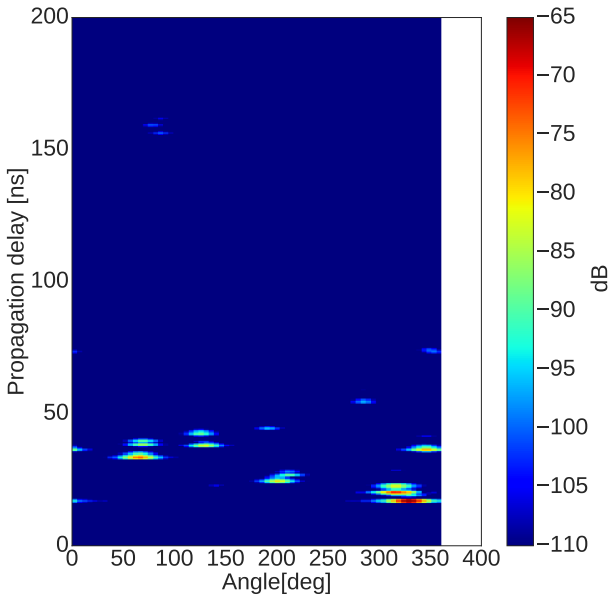

(b) BS-MS7: simulated PADP at 28 GHz.

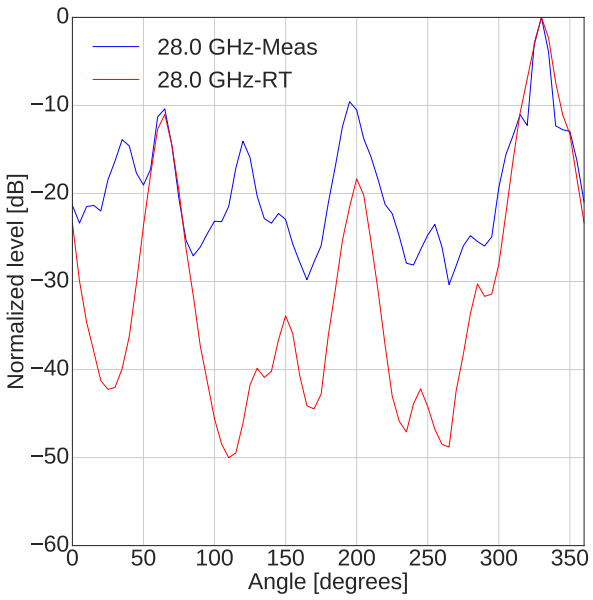

(c) BS-MS7: PAP comparison at 28 GHz.

Figure 4.11.: Comparison between the measured and simulated PADP and PAP of the link BS-MS7 at 28 GHz.

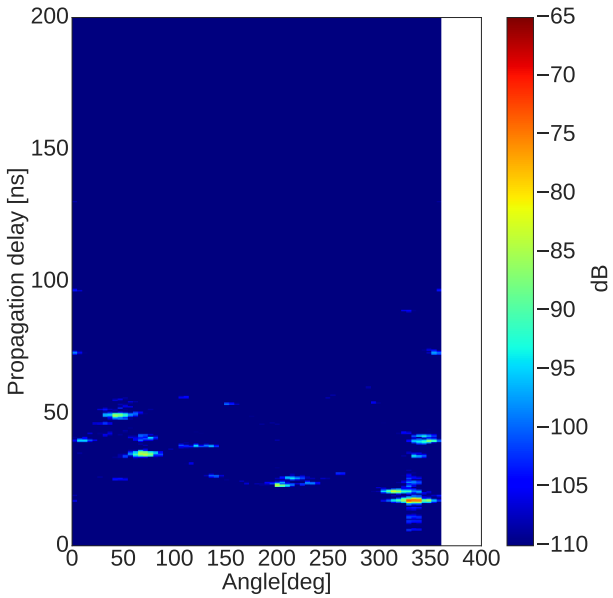

(a) BS-MS7: measured PADP at 83 GHz.

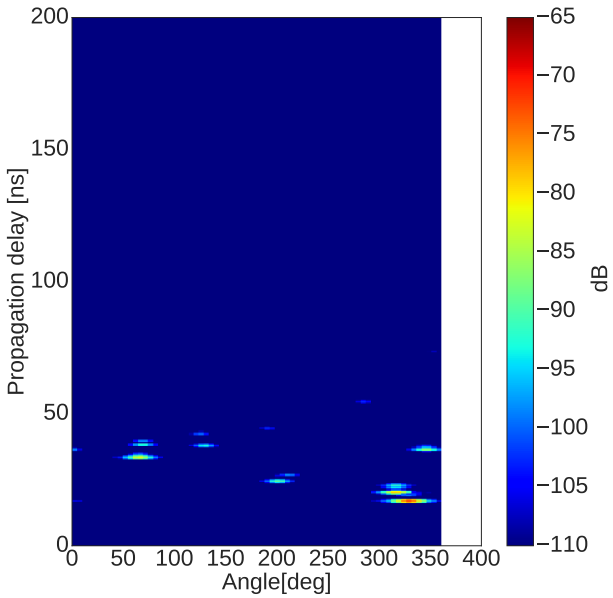

(b) BS-MS7: simulated PADP at 83 GHz.

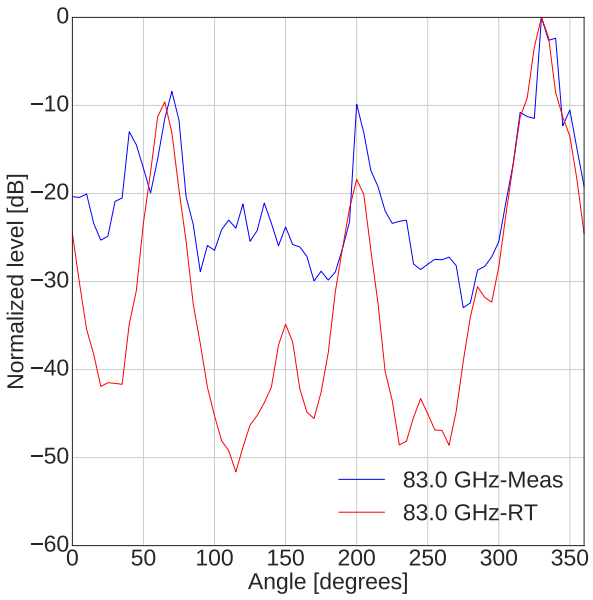

(c) BS-MS7: PAP comparison at 83 GHz.

Figure 4.12.: Comparison between the measured and simulated PADP and PAP of link BS-MS7 at 83 GHz.

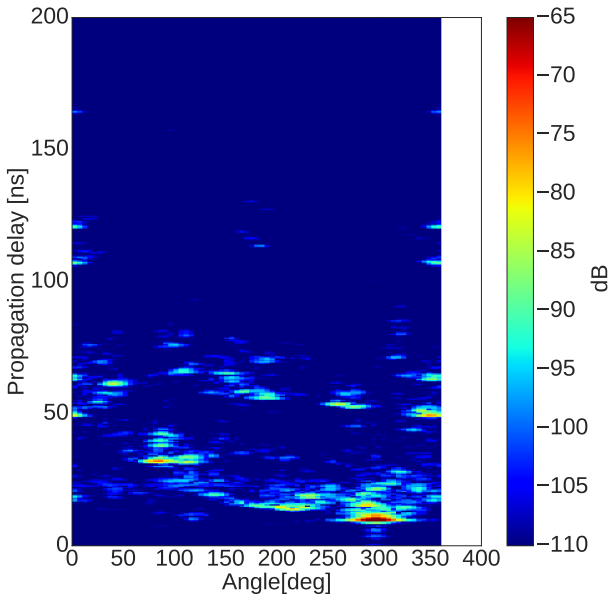

(a) BS-MS1: measured PADP at 15 GHz.

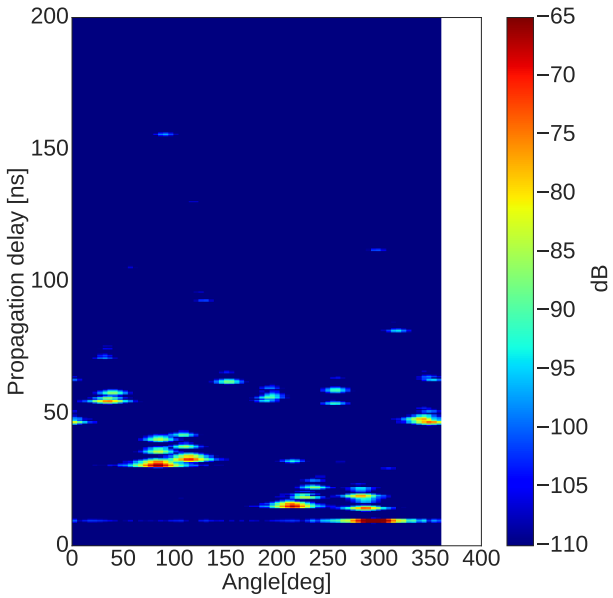

(b) BS-MS1: simulated PADP at 15 GHz.

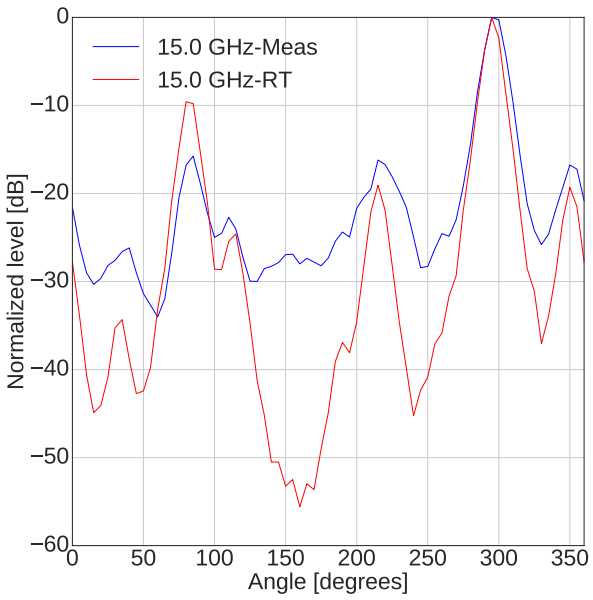

(c) BS-MS1: PAP comparison at 15 GHz.

Figure 4.13.: Comparison between the measured and simulated PADP and PAP of the link BS-MS1 at 15 GHz.

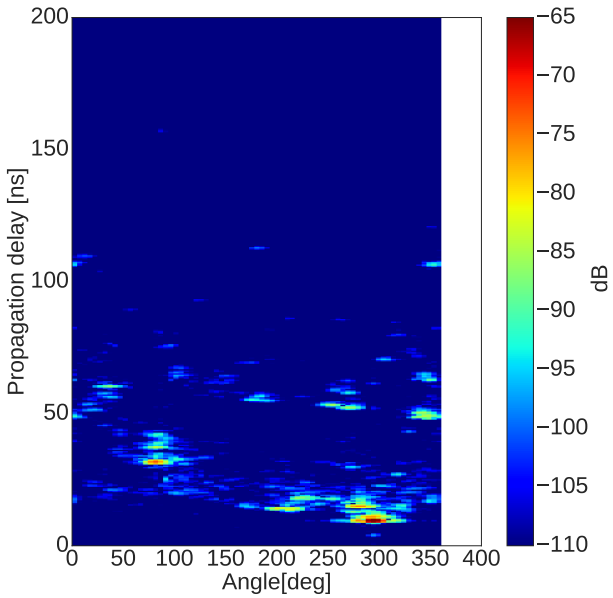

(a) BS-MS1: measured PADP at 28 GHz.

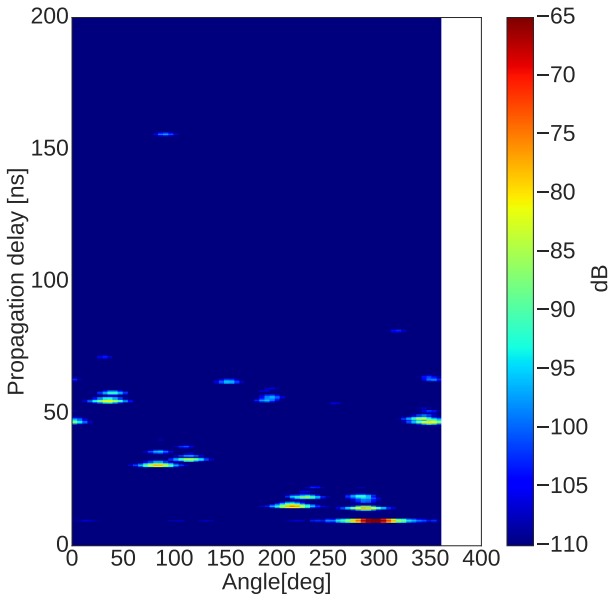

(b) BS-MS1: simulated PADP at 28 GHz.

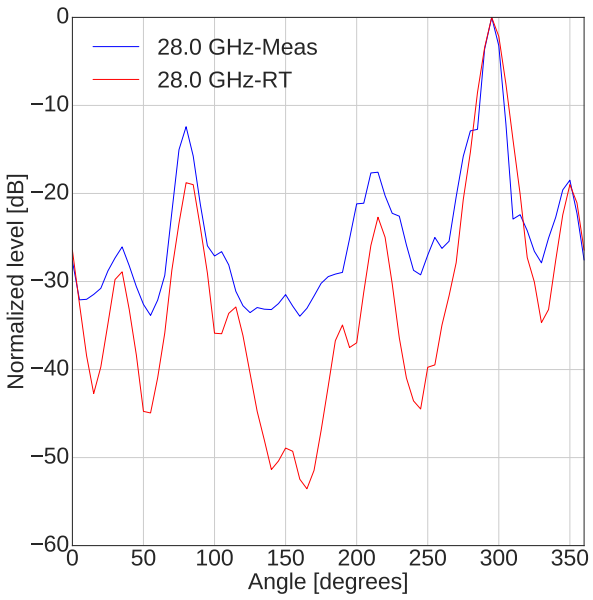

(c) BS-MS1: PAP comparison at 28 GHz.

Figure 4.14.: Multi-frequency InH comparison between the measured and simulated PADP and PAP of the link BS-MS1 at 28 GHz.

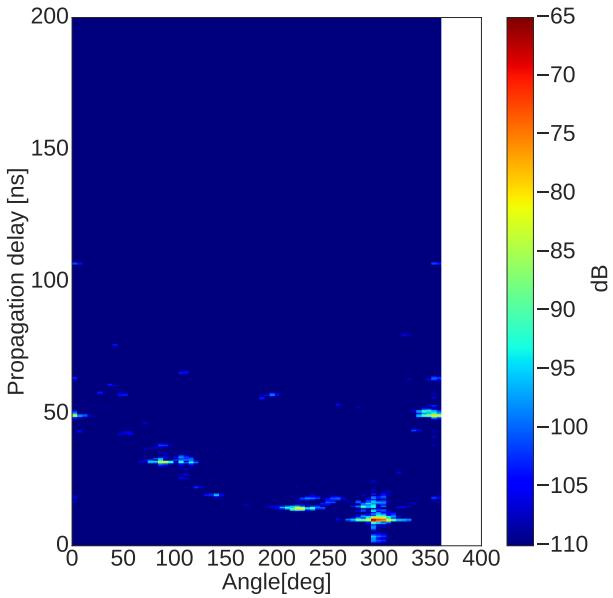

(a) BS-MS1: measured PADP at 83 GHz.

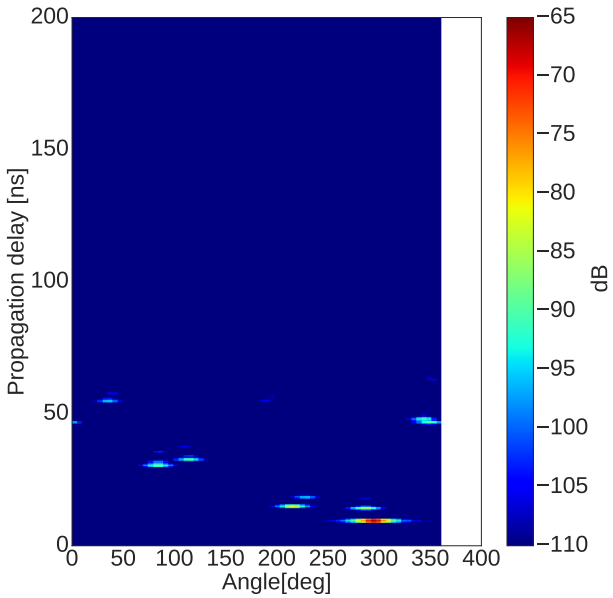

(b) BS-MS1: simulated PADP at 83 GHz.

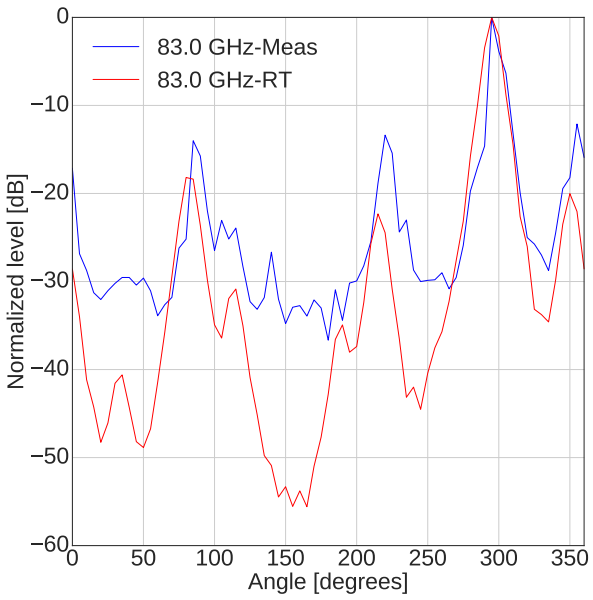

(c) BS-MS1: PAP comparison at 83 GHz.

Figure 4.15.: Multi-frequency InH comparison between the measured and simulated PADP and PAP of the link BS-MS1 at 83 GHz.

Focusing on the PADP metric, we can notice that the significant components observed in the measured data are quite well predicted by the RT at the three frequency bands while considering only LOS and SR mechanisms. However, some paths are over-estimated by the RT or sometimes are not predicted indicating probably a lack of an accurate description of the environment[6] and a non-optimization of material properties.

Similarly, the comparison w.r.t the PAP shows acceptable level of agreement at the three frequency bands as agreed in Fig. 4.10c, Fig. 4.11c, Fig. 4.12c, Fig. 4.13c, Fig. 4.14c and Fig. 4.15c.

4.3. RT vs $Meas.3$

4.3.1. RT: UMi Environment Description

In the RT simulator, building walls in the UMi environment are considered as rectangular flat and modeled as concrete while the window of the building B is assumed double glasses. The ground floor, the small electrical box, and the parking bike box are assumed to be concrete. The publicity-board located near the window of the building B with a height of 3 m is considered as a flat rectangular shape made of window glass. Other small metallic objects such as lamp-posts, road-signs, cars, basketball-signs and other urban furniture that were distributed around the measurement site are not taken account in the RT. Table 4.3 summarizes the material properties associated to the modeled UMi environment. As in the conference room, the electrical properties in the UMi environment are following the ITU-R P.2040-1.

	ϵ	σ_c [S/m]	Thick. [m]
wall	5.31	0.547	0.07
floor	5.31	0.547	0.1
window	6.27	0.274	0.01

Table 4.3.: Considered material properties of the UMi environment in the RT simulator.

4.3.2. UMi Simulation

Fig. 4.16 shows screen-shot examples of the RT performed in the UMi. The diffraction is turned off and the simulation time was less than 20 seconds. Fig. 4.16a displays the view of the 3D rays while Fig. 4.16b shows the 2D rays view.

[6] Table, chairs and other small objects are not described in the RT.

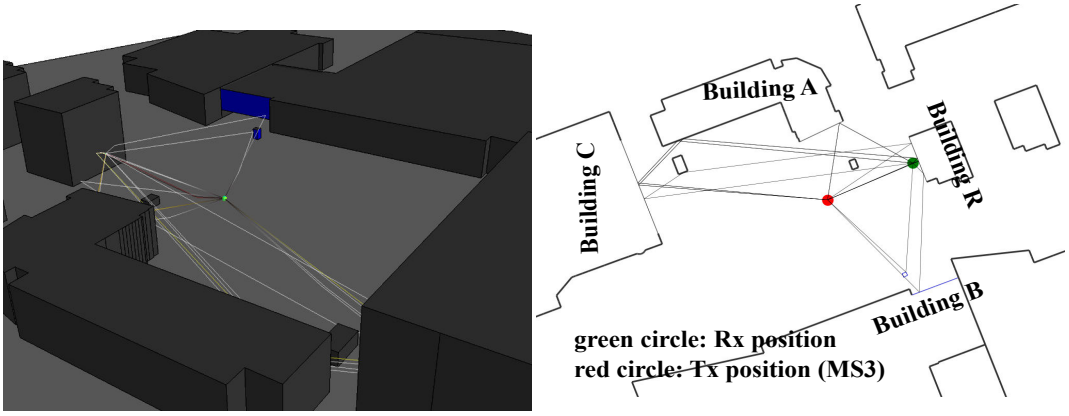

(a) 3D rays view of the UMi. (b) 2D rays view of the UMi.

Figure 4.16.: Screen-shots of the RT performed for the link BS-MS3.

The measured and the predicted PADP, PDP and PAP of links BS-MS3 and BS-MS10, chosen as an example, are shown in Fig. 4.17 and Fig. 4.18 respectively. Table 4.4 reports a summary of the major identified paths of the both links.

First, Fig. 4.17a and Fig. 4.17b display the measured and the simulated PADP for the link BS-MS3 while Fig. 4.17d compares the measured and the simulated PDPs. Only three paths are observed to be dominant in both measured and simulated data w.r.t the PADP and the PDP metrics. Path #1 is a combination of the LOS path and the GR path that appears 2 ns after the LOS component as reported in Table 4.4a. Path #2 is identified as a combination of the 1^{st} order SR over the wall of the building A and its GR and path #3 is the 1^{st} order SR over the publicity-board located near the window of the building B.

Second, Fig. 4.18a, Fig. 4.18b show respectively the PADP of the measured and simulated data of the link BS-MS10 while Fig. 4.18c compares the measured and the simulated PDPs. Only two paths are found to be significant for this link. Path #1 is identified as a combination of the LOS and a 1^{st} order SR over the wall of the building A. Both paths are close in delay and angle domain and presenting a strong level of power as summarized in Table 4.4b. Path #2 that appears around 426 ns in delay and presenting a strong level of power is identified as a 1^{st} order SR over the window of the building B.

In both BS-MS3 and BS-MS10 links, the RT was able to reproduce the significant PMs observed during the measurements. The spatial structure of the measured PADP and the shape of the measured PDPs are quite well retrieved. Moreover, the identified paths and their power level values reported in Table 4.4 show a reasonable level of agreement between the measurement and the simulation. Furthermore, the shape of the PAPs (Fig. 4.17c and Fig. 4.18d), dominated by the LOS component, is observed to be quite similar in both measurement and simulation.

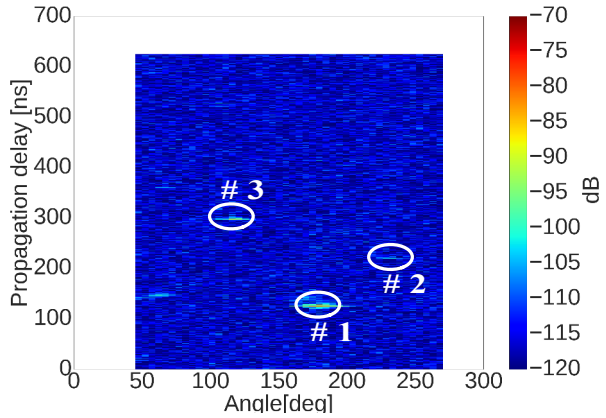

(a) BS-MS3: measured PADP at 32.6 GHz.

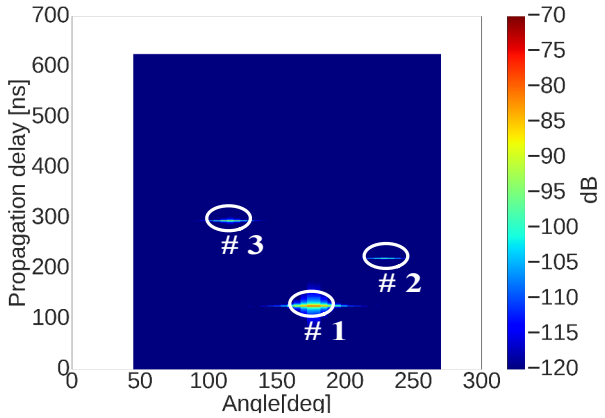

(b) BS-MS3: simulated PADP at 32.6 GHz.

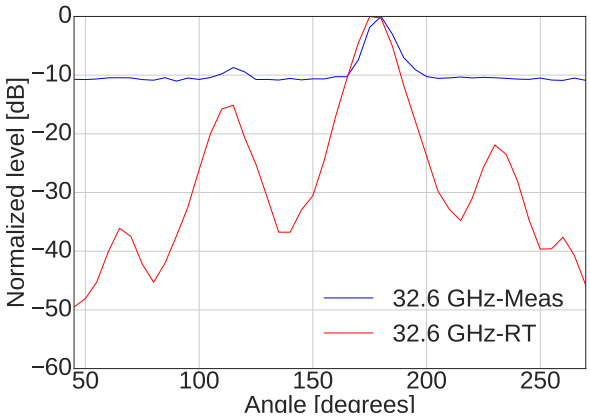

(c) BS-MS3: PAP comparison at 32.6 GHz.

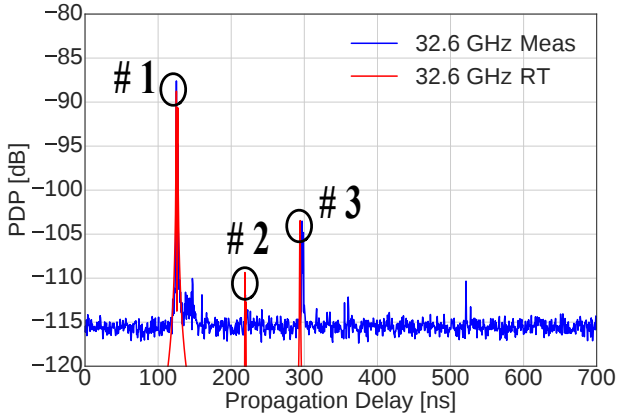

(d) BS-MS3: PDP comparison at 32.6 GHz.

Figure 4.17.: UMi: Comparison between the measured and simulated PADP, PDP and PAP of the link BS-MS3.

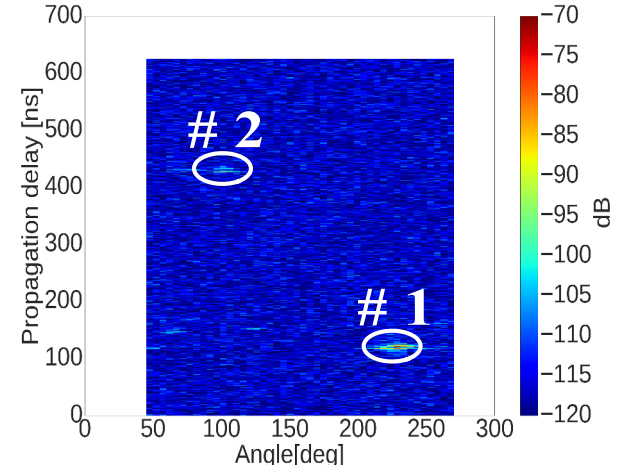

(a) BS-MS10: measured PADP at 32.6 GHz.

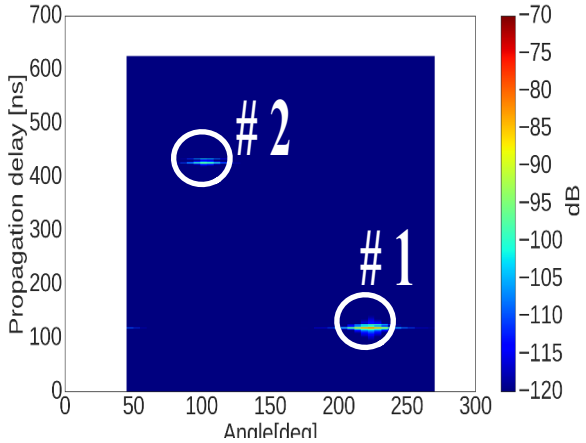

(b) BS-MS10: simulated PADP at 32.6 GHz.

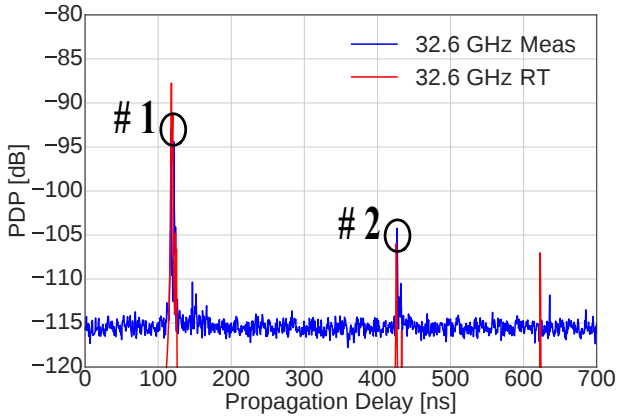

(c) BS-MS10: PDP comparison at 32.6 GHz.

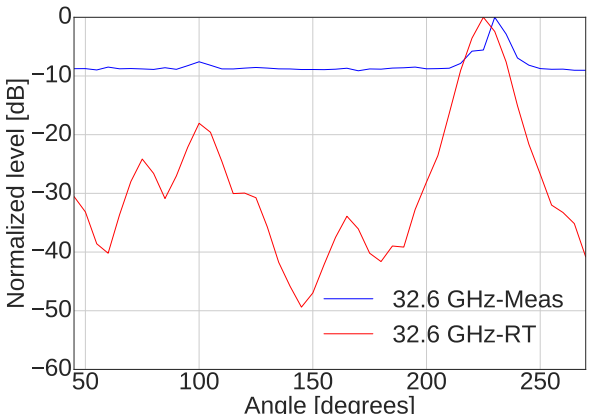

(d) BS-MS10: PDP comparison at 32.6 GHz.

Figure 4.18.: UMi: Comparison between the measured and simulated PADP, PDP and PAP of the link BS-MS10.

#	#1	#2	#3
Paths	[LOS;GR]	1^{st}SR	2^{nd}SR
P_{meas} [dB]	$[-74.6; -82.1]$	-101	-89.3
P_{RT} [dB]	$[-76.52; -81.8]$	-96.4	-90.5
τ_{meas}[ns]	[125; 127]	220	297
τ_{RT}[ns]	125; 127]	219	294
ϕ_{meas}[◦]	[180; 180]	231	115
ϕ_{RT}[◦]	[180; 180]	230	115

(a) Link BS-MS3

#	#1	#2
Paths	[LOS;1^{st}SR]	1^{st}SR
P_{meas} [dB]	$[-78.6; -81]$	-92.5
P_{RT} [dB]	$[-74.9; -81.5]$	-93.3
τ_{meas}[ns]	[117; 121.5]	427
τ_{RT}[ns]	[118.5; 120.5]	426
ϕ_{meas}[◦]	[226; 226]	100
ϕ_{RT}[◦]	[225; 225]	100

(b) Link BS-MS10

Table 4.4.: Paths prediction from the RT w.r.t the PADP.

However, we observed that the RT miss or over-estimates some paths as reported in Appendix A where a comparison between the RT and the UMi measurement is provided for the all links. The observed over-estimation may suggest to perform an optimization of material properties in order to have a good fit w.r.t the measured data. Furthermore, the missed paths might be attributed to the rough description of the environment and the non-stationary of the UMi environment since the measurements were conducted during working hours.

Worthy mentioning that from Table 4.4, a difference w.r.t the LOS level power can be noticed between the measured and the simulated data. This effect will be discussed in the next section.

4.3.3. UMi: Antenna Gains

In order to understand the difference observed between the measured and simulated data w.r.t the power level of the LOS, let analysis the antenna gain from the measured data. Fig. 4.19 presents the histogram of the combined MS-BS antennas gains of all link locations. The antenna gains are derived by subtracting the power of the LOS peak of the PADP to the FSPL. Basically, two sub-set of antennas gain values are observed: the sub-set 1 with the red histograms are constituted by links BS-MS2, BS-MS5, BS-MS9, BS-MS10 and BS-MS12 presenting a maximum combined antenna gains varying from 14.23 to 16.41 dB and the sub-set 2 represented by the green histograms showing antenna gains varying from 19.36 to 22.68 dB and constituted by links BS-MS1, BS-MS3, BS-MS4, BS-MS6, BS-MS7, BS-MS8, BS-MS11 and BS-MS13. Since the theoretical value of the combined antenna gains is 21 dB at 27.5 GHz, a variation of the observed antenna gains needs to be analyzed in detail.

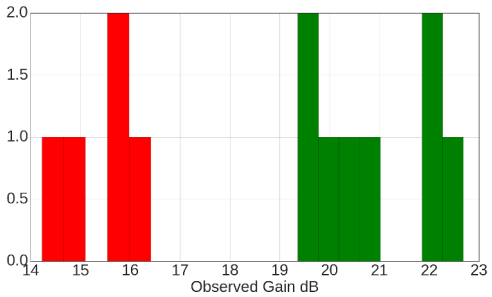

Figure 4.19.: Histogram of the combined antennas gain obtained from the FSPL and the LOS peak.

Hypothesis 1: non bore-sight Antennas

We assume that the large variation of the antenna gains is originated from the miss of the bore-sight antenna[7]. Accordingly to the measurement setup where a rotational step

[7]The maximum of the horn antenna is not aligned with the biconical antenna.

of 5° was applied and considering a HPBW of 5° in azimuth, a loss of 3 dB from the total antenna gain can be obtained in a worst case and therefore this hypothesis does not explain the values observed in the sub-set 1.

Hypothesis 2: Shadowing

The value of the sub-set 1 showing a decrease of antenna gains reaching 6.77 dB might be attributed to the UMi shadowing effect. Since we addressed an UMi environment where MS positions were surrounded with as well as the measurement campaigns were conducted during working hours, the auscultation due static objects, people walking near the MS antenna or moving cars in the environment may happen and such moving scatterers might obstruct the LOS link and therefore explaining the observed difference.

4.3.3.1. $Meas.3$: LSP Analysis

The analysis of the LSPs of the $Meas.3$ as well as the comparison against the RT tool is given in Fig. 4.20. Worthy notice that the same parameters used in section 3.3.5.3 for detecting the peaks were used in this section (i.e. $\Delta = 5$ ns and $th^{cst} = 5$ dB). Further, the DS, AAS and the omni-directional PL were computed from Eq. 2.26, Eq. 2.29 and Eq. 2.28 discussed in chapter2.

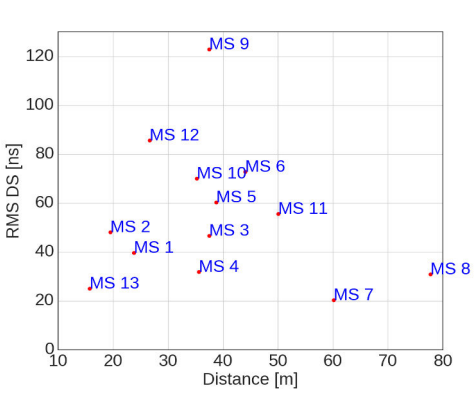

(a) *DS* of meas.3 derived from the fine peak search.

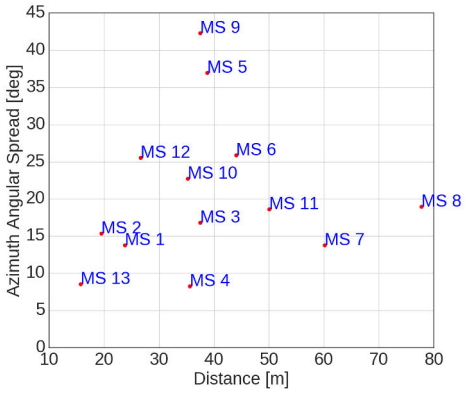

(b) *AAS* of meas.3 derived from the fine peak search.

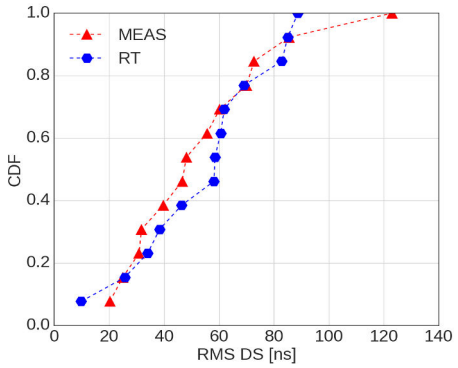

(c) Comparison between the measured and the simulated *DS* at 32.6 GHz.

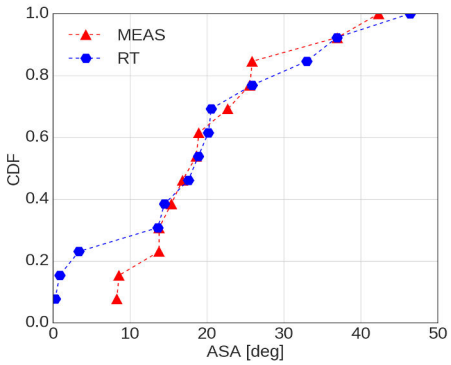

(d) Comparison between the measured and the simulated *AAS* at 32.6 GHz.

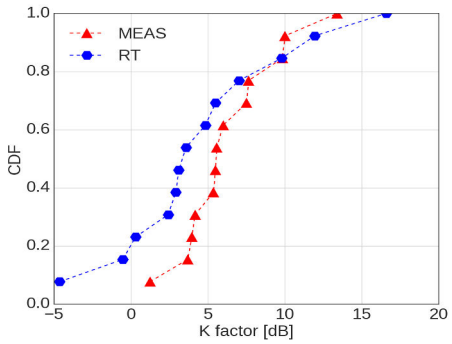

(e) Comparison between the measured and the simulated *KF* at 32.6 GHz.

Figure 4.20.: UMi: LSPs comparison.

The *DS* and the *AAS* of *Meas.*3 are depicted in Fig. 4.20a and Fig. 4.20b respectively. Both the *DS* and *AAS* are found to be quite small with spread values ranging from 20.3 ns to 122.9 ns for the *DS* and from 8.28° to 44.32° for the *AAS*. A larger spread is

attributed to a radio channel propagation where the significant amount of energy comes from many directions and not only a specific direction (e.g the LOS direction). As shown in Fig. 4.20a and Fig. 4.20b, the MS9 is observed to present a higher delay and azimuth spread mainly due to the strong 1^{st} order SR from the window of the building B. Furthermore, a slight increase of the DS and the AAS is noticed when the BS-MS link distance increases. The observed phenomenon can be attributed to the considered UMi scenario that includes an open square and surrounded buildings and as the distance of the MS increases, the AAS increases.

The cumulative distribution function (CDF) of the simulated and measured DS and AAS are given in Fig. 4.20c and Fig. 4.20d. We can observed that 90% of the DS values fall below 80 ns while 90% of the AAS fall below 33° in both the measured and the predicted data. In addition, the range of the DS and AAS found in both measurement and simulation are in line with the typical values that have been reported in the literature in UMi mm-wave [11, 111]. Fig. 4.20e depicts the CDF of the KF for the measurement and the simulation. Generally, a higher KF is noticed and 90% of the measured and simulated KF fall below 10 dB. The statistical parameters are given in Table 4.5. The table summarizes the statistical parameters of the measured and predicted LSPs and compared to those shown in the 3GPP [15] applicable to mm-wave radio frequencies and covering the UMi-street canyon with a BS height of 10 m. In general, a quite good agreement can be observed for the three cases.

Table 4.5.: Summary of the UMi LSPs comparison between at $f_c = 32.6$ GHz.

		LOS UMi	
Spec.	*Meas.3*	RT	3GPP
DS (s)			
μ(log10([s]))	−7.3	−7.3	−7.5
σ(log10([s]))	0.21	0.25	0.38
ASA (∘)			
μ(log10([°]))	1.26	1.03	1.13
σ(log10([°]))	0.2	0.6	0.41
KF (dB)			
μ(KF[dB])	6.4	4.8	9
σ(KF[dB])	3	5.3	5

4.4. Summary

This chapter was mainly dedicated to the presentation of the RT tool and its evaluation through the measured data obtained in $Meas.2$ and $Meas.3$. Using a graph-based modeling approach makes the RT fast and robust in the evaluation of the rays for different indoor and outdoor environments. Moreover, the implementation of the sectoral horn an-

tenna aperture used in the measurements is presented and validated through simulation. The multi-frequency comparison between the measured and the simulated data in the InH conference room is provided in this chapter. It was demonstrated that the RT was able to predict the dominant paths of the InH conference room at the three frequency bands in LOS conditions. The PADP and the PAP were chosen as metric comparisons and a reasonable level of agreement was noticed. Furthermore, the RT was used to interpret the measured data w.r.t the physical UMi propagation environment. The RT was able to predict the significant path contributions of the 32.6 GHz UMi channel in LOS conditions with an acceptable level of agreement while only assuming LOS and SR mechanisms. Moreover, the LSPs between the measurement and the prediction were studied and a satisfactory agreement was observed.

Chapter 5

General Conclusion

5.1. Summary

The mm-wave cellular technology is coming along with the upcoming 5G standard and it is expected to change radically performances of communication and localization systems. This evolution is largely becoming possible due to the reduction of the wavelength making viable the utilization of antenna arrays at both sides of the link. In the 5G context, high data rate and low latency can be achieved by using antenna technologies combined with advanced signal processing allowing to create a very stable channel with large coherence time and low fading. Nevertheless, the mm-wave technology is facing to several challenges as the cell size reduce and consequently propagation conditions may change in a large amount from one site to another. Since cellular mm-wave technology can be considered as a site-specific technology, the local context in terms of scatterers and time variability of the channel creating blockage from human or vehicles for instance is going to be very different from one place to another and hence will require large adaptivity from the network and the mobile. Therefore, it would be interested for operators, equipment vendors and academics to have simulation tools which take into account those large varieties of situations. And one of the purposes of this work was to push forward the development of such an open source simulation tool mostly by providing a comprehensive database of measurements in several contexts and to calibrate and tune the simulator tool.

This work is a new contribution to a better knowledge of the cm- and mm-waves radio channels in various representative indoor and outdoor scenarios. Different scientific purposes were studied addressing research questions related to the mm-wave radio channel characterization and its prediction by the use of an open source site-specific for link and system simulation tool. The work accomplished in this thesis is described in three main chapters (Chapter 2-4) and discussed subsequently as follows. The current state of the art regarding the existing and the ongoing channel modeling studies for mm-wave

applications has been presented first. The review revealed the necessity to have consistent framework related to measurements database. In order to tackle this challenge, significant efforts were made in this work by conducting cm- and mm-wave measurement campaigns covering various and realistic propagation scenarios.

The main motivations for conducting measurements were to study the time variability and the scattering environment effect of the mm-wave radio channel. Furthermore, the measured dataset was used as a basis for evaluating the performance of the RT tool. A total of four measurement campaigns performed at 15, 28, 32 and 83 GHz and conducted in an office room, library environment, conference room, campus area and UMi scenarios were presented in this thesis.

*Meas.*0 and *Meas.*1 were dedicated to study the dynamic mm-wave channel at 28 GHz in three environments: one in outdoor scenario (campus area) and two in indoor (office room and library) respectively. The mobility aspect was addressed by moving the MS mounted on a trolley while the BS was in a fixed position. Different routes were covered including LOS, OLOS and NLOS conditions. A biconical antenna was considered at the MS side while a horn antenna was used at the BS side. Both of them were designed in vertical polarization.
*Meas.*2 and *Meas.*3 were conducted to investigate the scattered environments in cm- and mm-wave bands and to evaluate the RT tool developed in our laboratory. In contrast to the measurement procedure described in *Meas.*0 and *Meas.*1, both MS and BS antennas were in a fixed position. The BS antenna was equipped with a horn antenna designed in a vertical position and rotating in the azimuthal plane while a biconical antenna designed in vertical polarization was considered at the MS side.
*Meas.*2 was performed in a conference room and three frequency bands identified by the WRC-15 were addressed: 15, 28 and 83 GHz. Twenty MS positions per frequency band with a MS distance separation of 50 cm were chosen to emulate a trajectory covering both LOS and NLOS situations.
*Meas.*3 was carried-out at 32.6 GHz in an UMi scenario. The chosen measurement site presents key similarity with the generic Madrid-grid specified in the METIS project with the presence of buildings with different height level as well the presence of an open square and a regularity of width street separation. The BS was placed at a height of 6 m while covering $\frac{2}{3}$ plane sectorization. Sixteen MSs locations with a height of 1.65 m representing a pedestrian level were distributed on the measurement site in LOS and NLOS conditions as it can be in a real small-cell deployment scenario.

The data gathered during the measurements are then analyzed.

- First, the analysis of the mobile measurement data extracted from the campus area revealed a measurement error attributed to a bad isolation of connectors.
- The dissemination of the measurement performed in the office room and library environments has shown the time-variant structure of the channel. In the direct route configuration (i.e. I1-R11 and I2-R21), the variation of the MPCs origin-

ated from multiple SR mechanisms have been observed to be spatially consistent and presenting almost the same slope. What is more, a direct path was found to exist in the OLOS situation w.r.t the transmission mechanism via books in the library environment at 28 GHz. In such a configuration, it would be interesting to investigate such a phenomenon in other frequency bands. In addition, measurements highlighted the dominance of the reverberation effect in the small office room compared to the library environment. Furthermore, a statistical study regarding different LSPs extracted from the office room and the library measurements at 28 GHz was provided and compared with those already produced in the literature.

- Second, the dissemination of $Meas.2$ revealed the consistency of the radio channel as the frequency is varying and the MS is moving.
- Third, the processing of the UMi measured data demonstrated the presence of only a few strong contributors in the 32.6 GHz UMi environment. Furthermore, a method to illustrate the effect of the scatterers in the UMi environment was proposed. The method assumes a single bounce approach which is simplest but makes sense in mm-wave and the idea was to apply a geometrical transformation which establishes an one-to-one mapping between the measured data and the map. The proposed `back-projection` method demonstrated that the energy in the UMi environment comes from essentially walls and window buildings through a 1^{st} order SR. Furthermore, it was found that urban furniture such as publicity-board was delivering energy as well as metallic object distributed in the environment such as lamp-posts and road-signs.

The second part of this work was dedicated to the presentation of the RT tool and its evaluation through a comparison against the measured data. The RT tool developed in our laboratory is based on a graph-based description of the radio channel aiming to reproduce relevant channel properties while covering various indoor and outdoor environments. For comparison purposes, the RT simulator was compared to $Meas.2$ and $Meas.3$. First, a comparison between the measured and the predicted data in the conference room environment at 15, 28 and 83 GHz in LOS condition was presented. Accordingly to the PADP metric, the InH conference room radio channel propagation was almost predicted by the RT tool at the three frequency bands while only considering LOS and SR mechanisms. Furthermore, the comparison between the measured and the predicted PAP has shown an acceptable level of agreement.
Second, the use of a RT in UMi scenario has demonstrated the ability to predict the significant components by only assuming the LOS and SR mechanisms and a rough description of the environment. Moreover, a comparison in terms of LSPs between the measured and the simulated data in UMi scenario has shown a reasonable level of agreement.

In general, the RT tool was able to predict the mm-wave InH and UMi radio channels in LOS condition with a reasonable computation time while considering only the LOS and the SR mechanism and assuming a rough description of the environment. This

potentially indicates that the structure of the channel model in mm-wave is going to be simple and easily predicted by simple site-specific tools.

5.2. Perspectives

This thesis brought a contribution to the challenge of the mm-wave radio channel characterization on a sanity check of the site-specific simulation by covering a large set of measurement campaigns performed in various realistic propagation scenarios. The data which has been gathered thanks to the Aalto university channel sounder, should be post-processed more. The current work presented in this thesis only scratches all the possible useful insights which can be extracted from those data. Several scientific questions and new tools and models have to be built and in the following some recommendations for further studies are provided:

- Continue to exploit measurements data presented in this thesis. Since efforts were made to provide a database measurement data in several representative scenarios and covering different mm-wave bands, measurements data are not fully exploited.
- The several comparisons which have been made with the ray tracing simulation is quite good at the time, but still the identification of the scatterers which are involved in a given propagation scene can bring a lot of information about the characteristics of a material which has to be chosen.
- The UMi measurement which has been done during this thesis suggests that relatively small and smooth surfaces can bring a lot of energy to the receiver almost without attenuation. The UMi scenario should be reproduced along a route with a broad aperture in order to capture the time duration of those *flash* and their lifetime in both measurement and simulation.
- Improving and extending the RT tool. For the indoor situation it would be interesting to incorporate the effect of the reverberation in the RT tool since this effect has been clearly observed and deserving to be accounted for in the channel models. In addition, the current version of the RT tool does not support the I2O scenario. Furthermore, it would be useful to use the RT for investigating the spatial consistency of the mm-waves channel.
- In this thesis we have reproduced as closely as possible the measurement protocol with the RT tool, so to reproduce in simulation the measured data. This approach should be extended in case of antenna arrays at both sides of the link instead of using omni-directional and rotating horn antenna.
- To introduce the mobility and the effect of blockage in the RT tool which are important especially when considering mobile user tracking algorithm.
- To leverage the RT tool for supporting RF planning and coverage simulation in mm-wave outdoor use cases.

Appendix A

Espoo UMi measurements

This appendix provides an exhaustive representation of the measured and simulated UMi LOS spatio-temporal characteristics at 32.6 GHz. The measured and the predicted data are jointly represented. For the shown simulations, the diffraction was activated. Each figure presents several elements. The top figure illustrates the layout and the rays color coded w.r.t their power levels. The colored matrix is the image plot of the PADP for the calibrated measurement data (on the left) and the PADP obtained with the RT (on the right). On the left of each PADP is the associated PDP obtained with the formulation Eq.2.19. On the PDP curves are plotted as a reference the FSPL bounded by two curves highlighting the observed variability in the cumulative antenna gain value which is not constant from one acquisition to another. When the PDP crosses the FSPL curve, a red dot line is plotted. This is a way to identify the strong reflective contributors. On the bottom, there is the PAP obtained with Eq. 2.19. The dotted line denotes the noise floor. As a general observation the general structure of the PADP is globally pretty well recovered. Nevertheless a careful examination allows identifying the missing scatterers as well as the overestimated contributions.

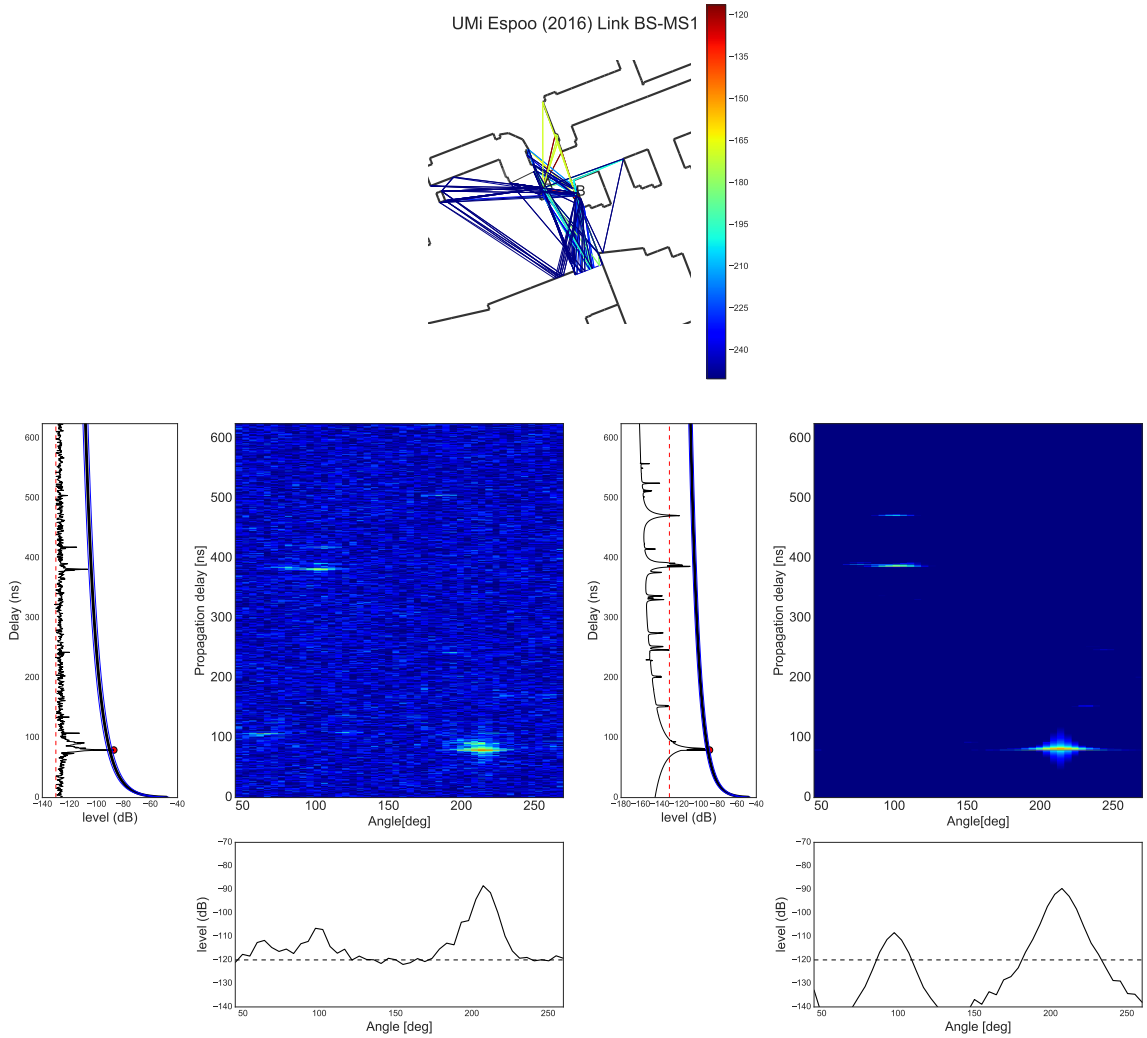

Figure A.1.: 32.6 GHz UMi Espoo: BS-MS 1 - PDP (left) PADP (middle) PAP (bottom) for measurement (left) and RT simulation (right)

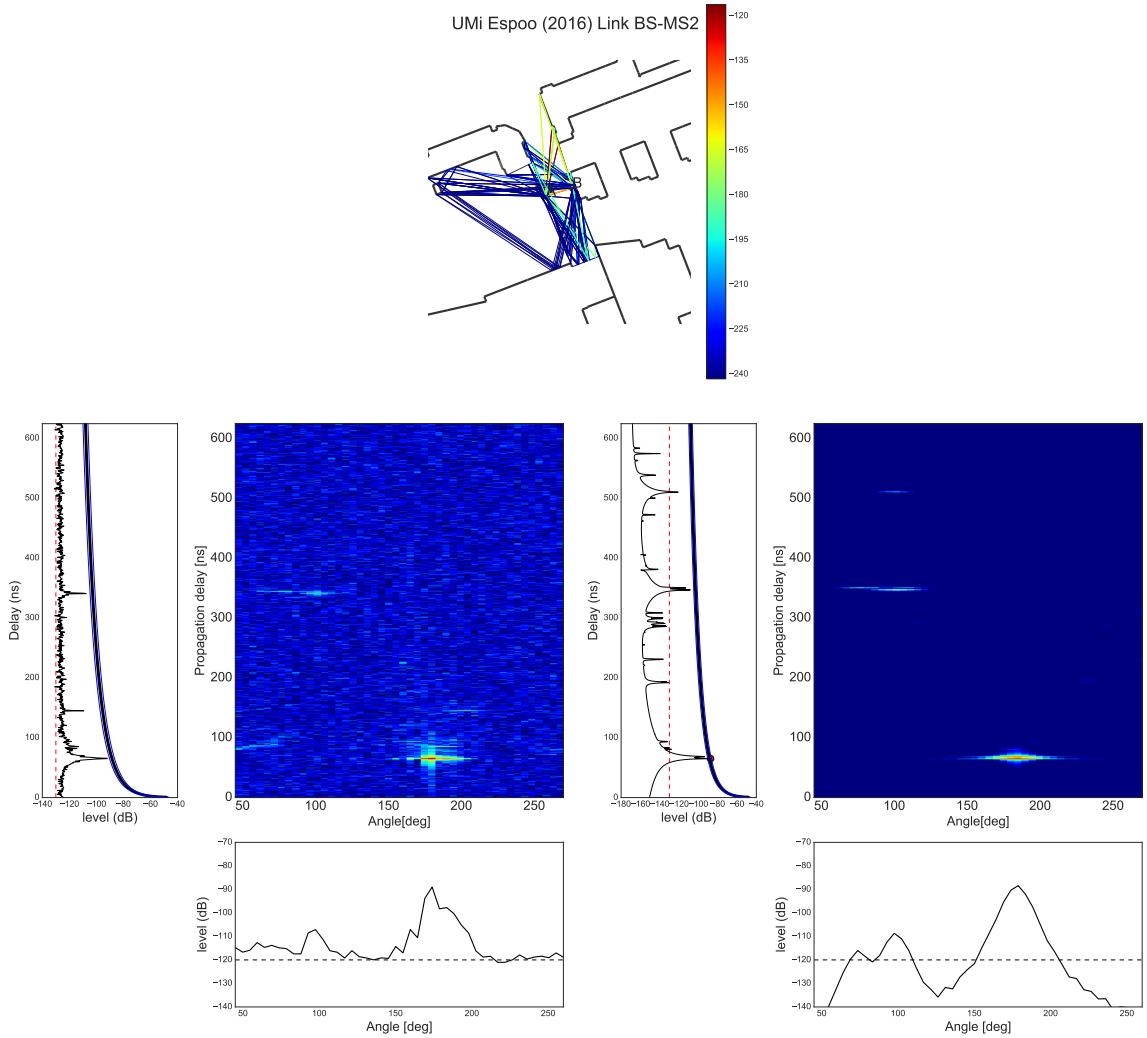

Figure A.2.: 32.6 GHz UMi Espoo: BS-MS 2 PDP (left) PADP (middle) PAP (bottom) for measurement (left) and RT simulation (right)

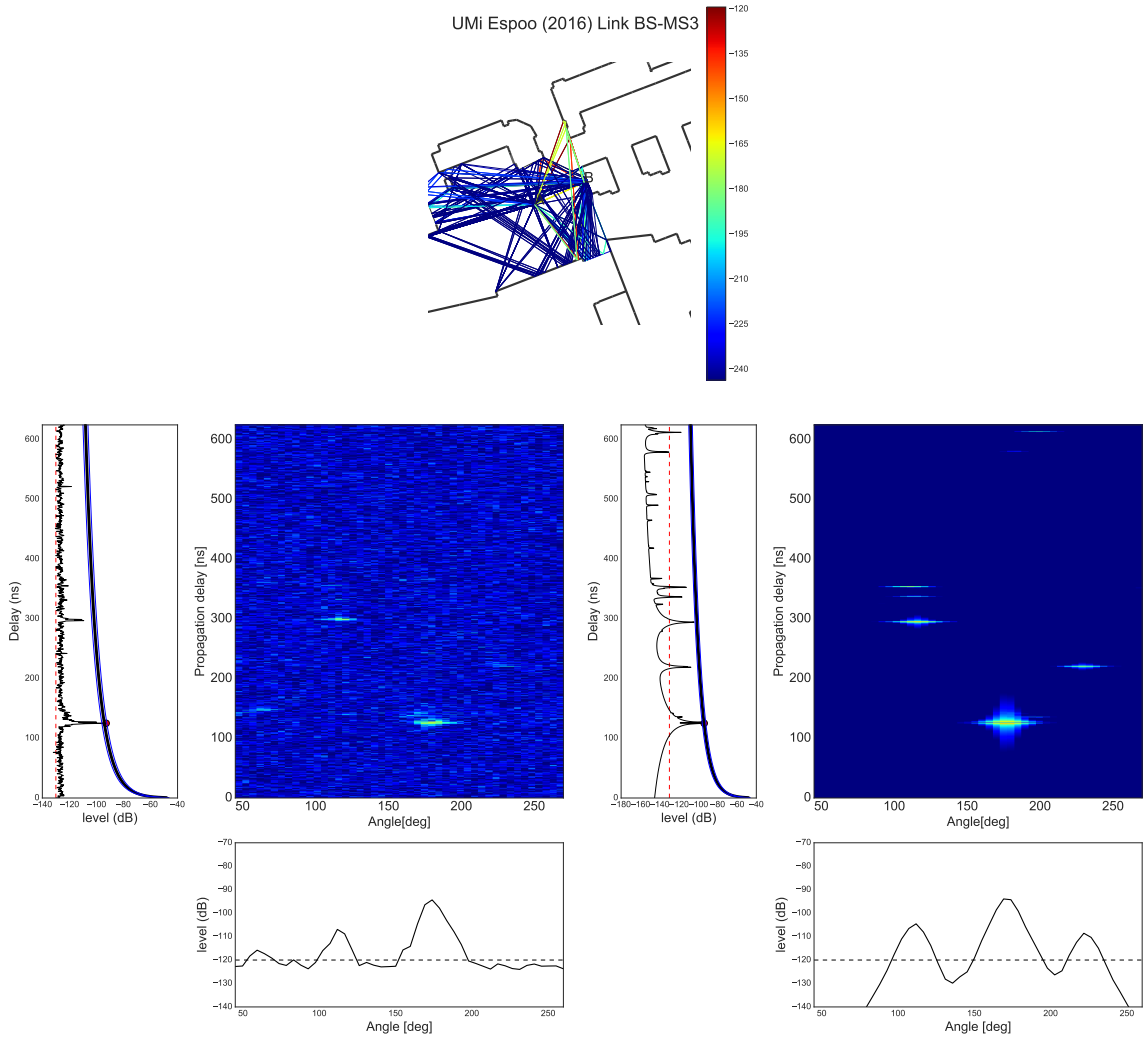

Figure A.3.: 32.6 GHz UMi Espoo: BS-MS 3 PDP (left) PADP (middle) PAP (bottom) for measurement (left) and RT simulation (right)

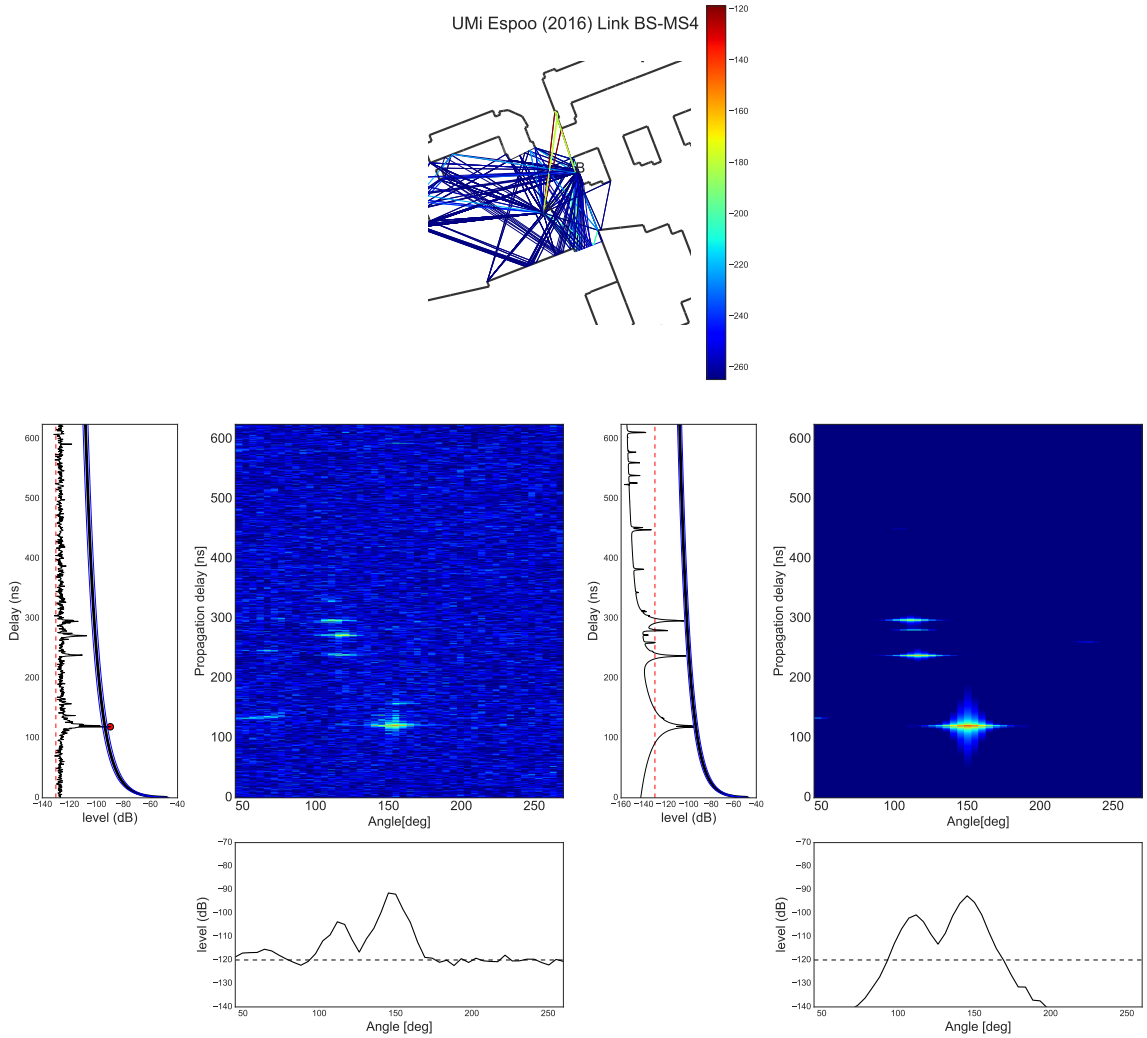

Figure A.4.: 32.6 GHz UMi Espoo: BS-MS 4 PDP (left) PADP (middle) PAP (bottom) for measurement (left) and RT simulation (right)

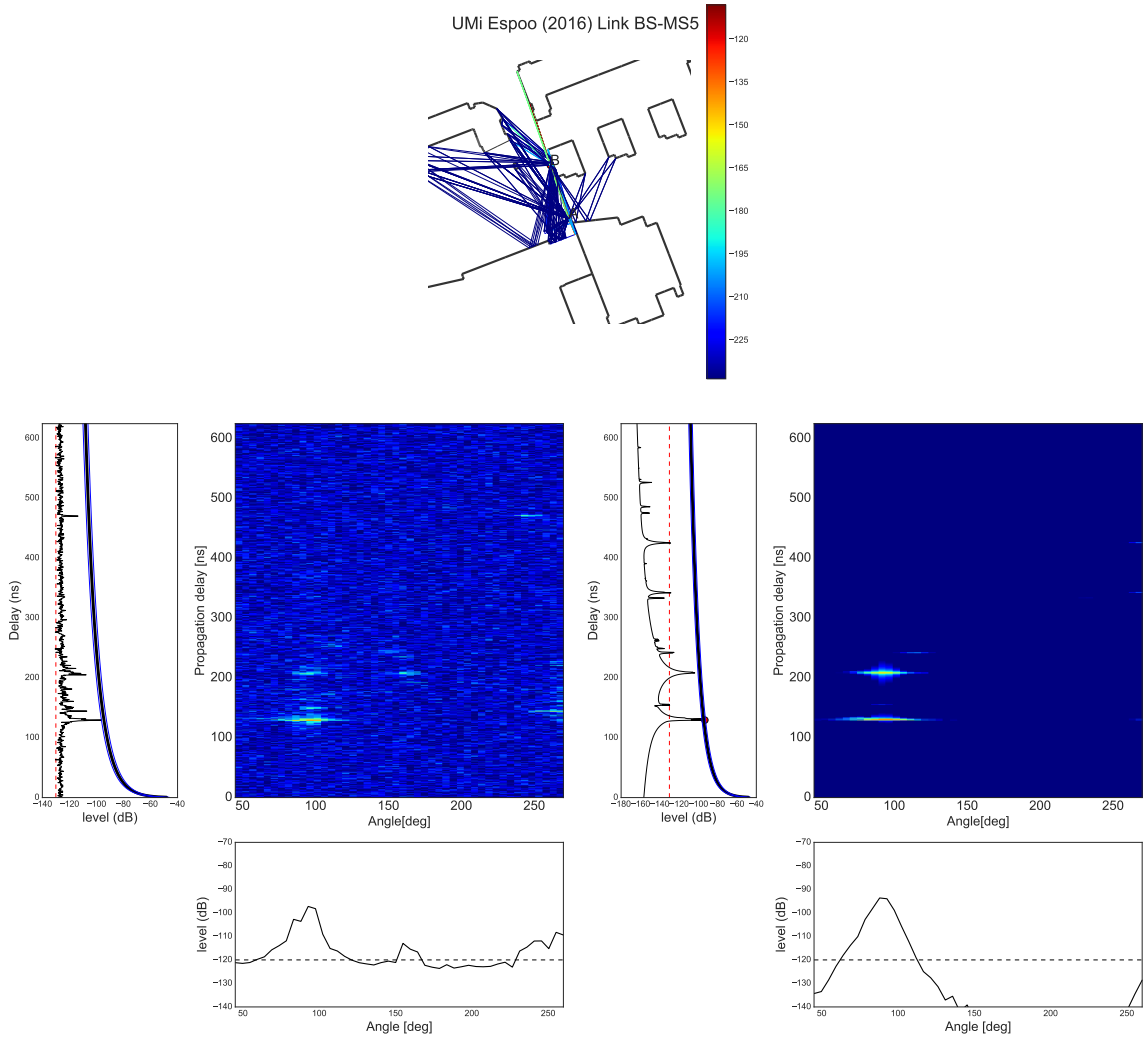

Figure A.5.: 32.6 GHz UMi Espoo: BS-MS 5 PDP (left) PADP (middle) PAP (bottom) for measurement (left) and RT simulation (right)

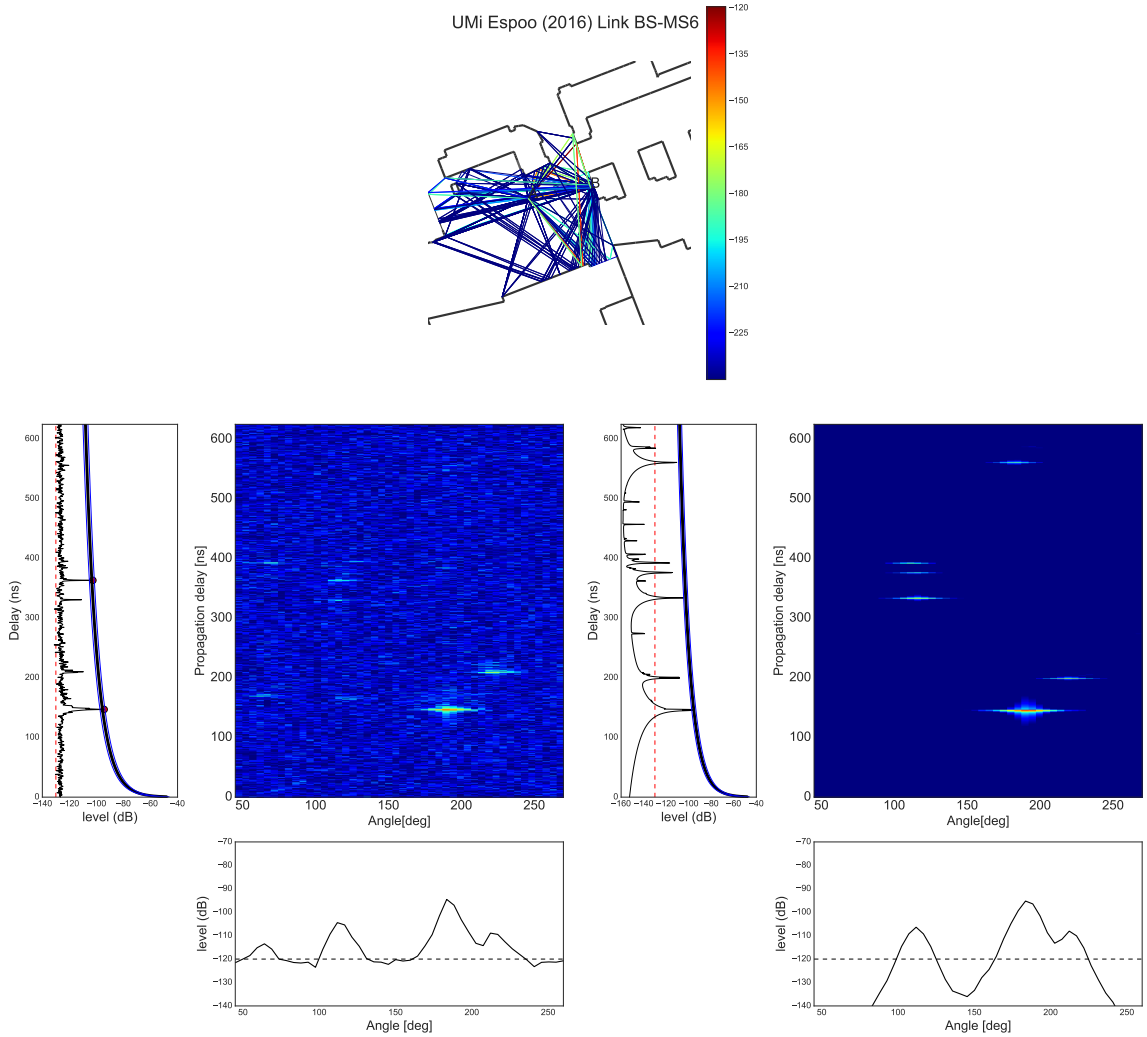

Figure A.6.: 32.6 GHz UMi Espoo: BS-MS 6 PDP (left) PADP (middle) PAP (bottom) for measurement (left) and RT simulation (right)

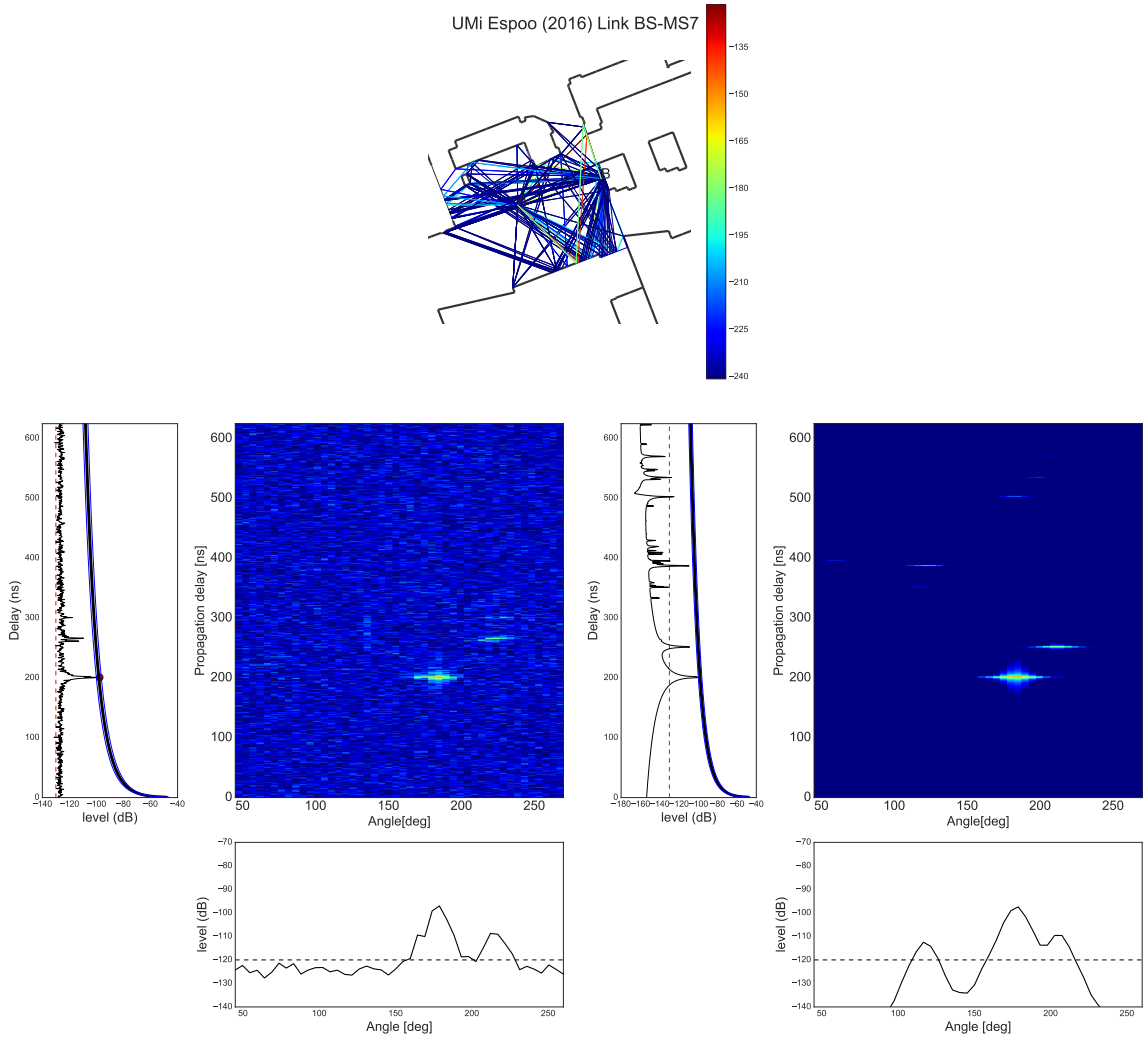

Figure A.7.: 32.6 GHz UMi Espoo: BS-MS 7 PDP (left) PADP (middle) PAP (bottom) for measurement (left) and RT simulation (right)

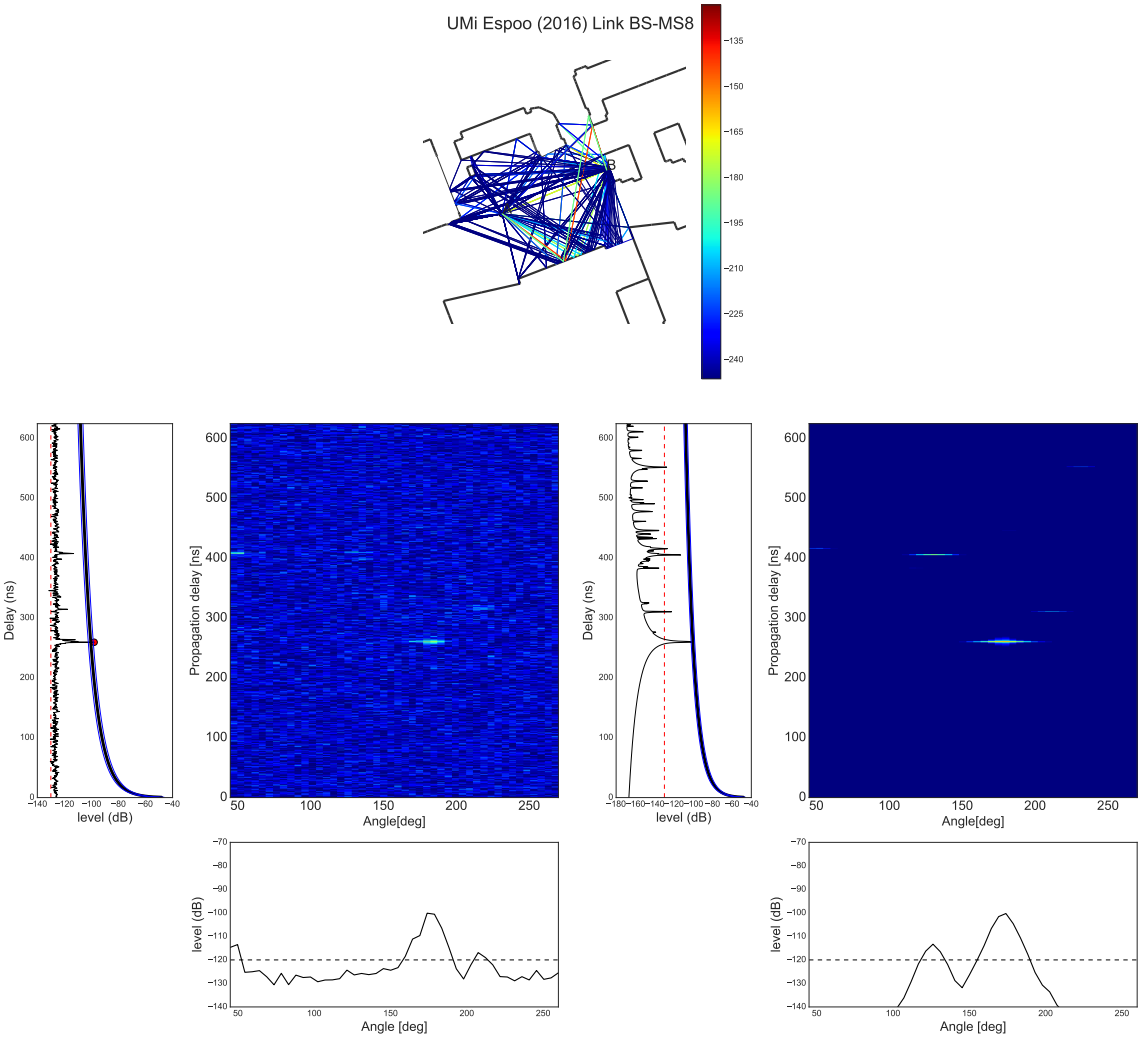

Figure A.8.: 32.6 GHz UMi Espoo: BS-MS 8 PDP (left) PADP (middle) PAP (bottom) for measurement (left) and RT simulation (right)

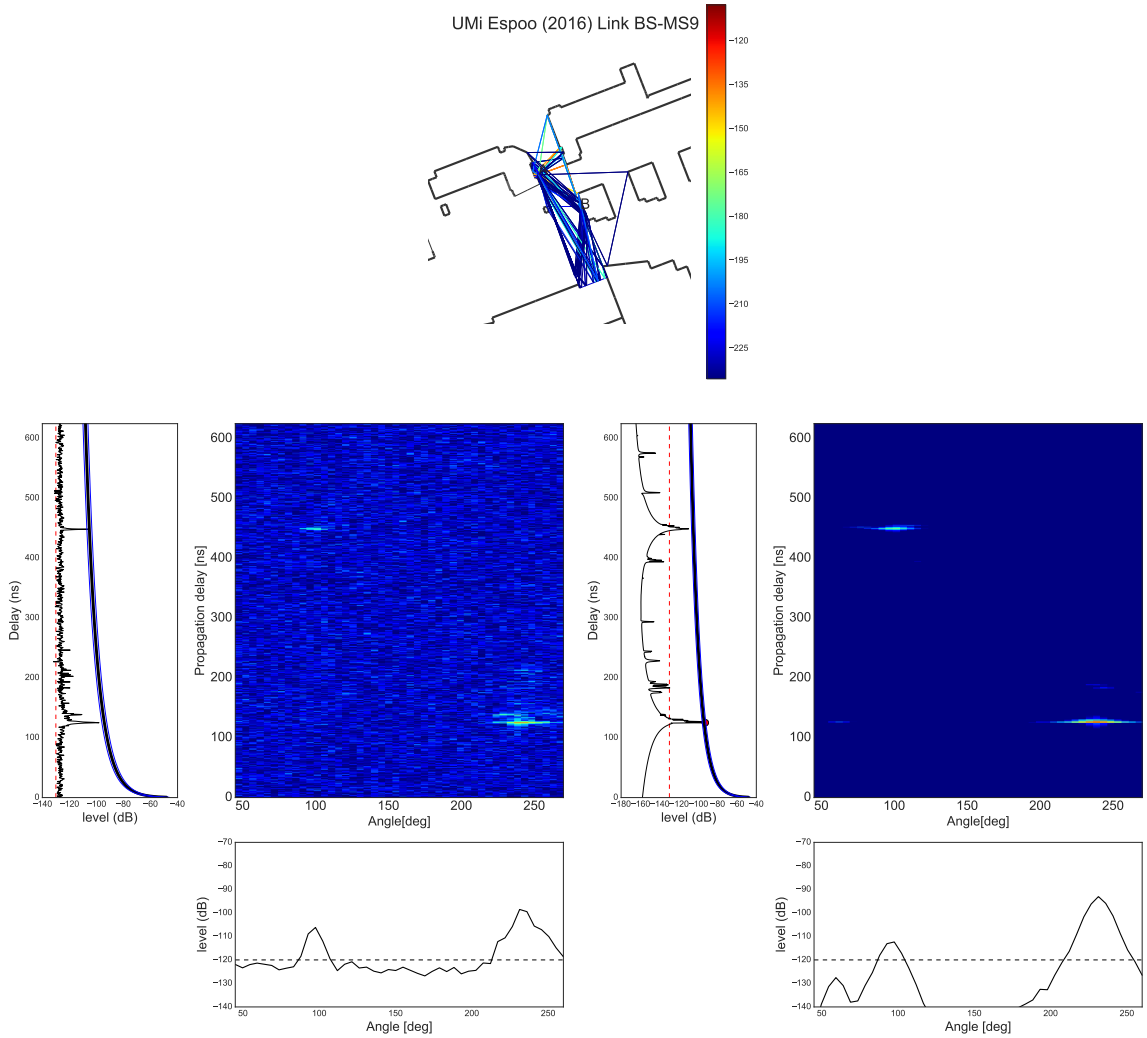

Figure A.9.: 32.6 GHz UMi Espoo: BS-MS 9 PDP (left) PADP (middle) PAP (bottom) for measurement (left) and RT simulation (right)

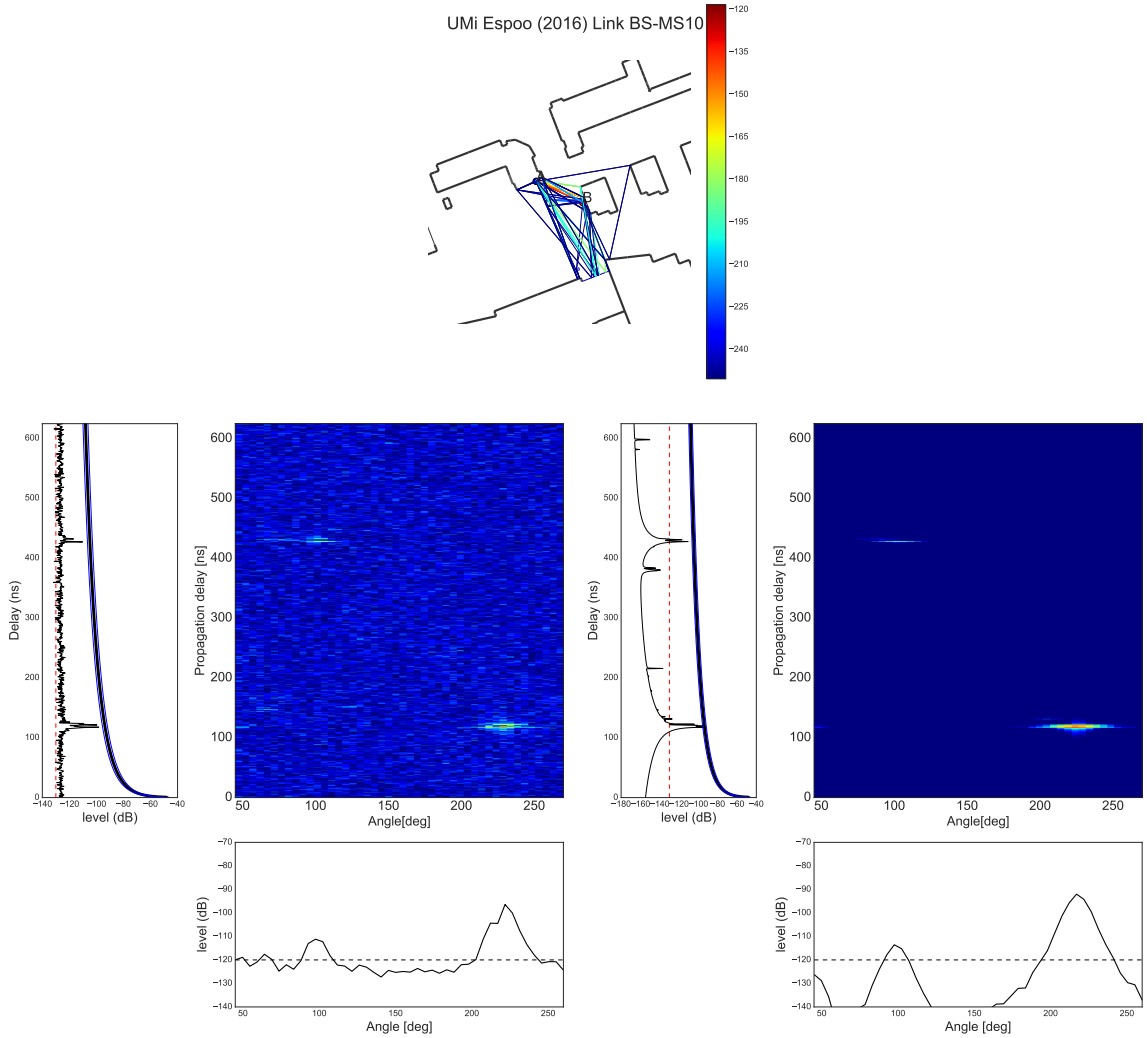

Figure A.10.: 32.6 GHz UMi Espoo: BS-MS 10 PDP (left) PADP (middle) PAP (bottom) for measurement (left) and RT simulation (right)

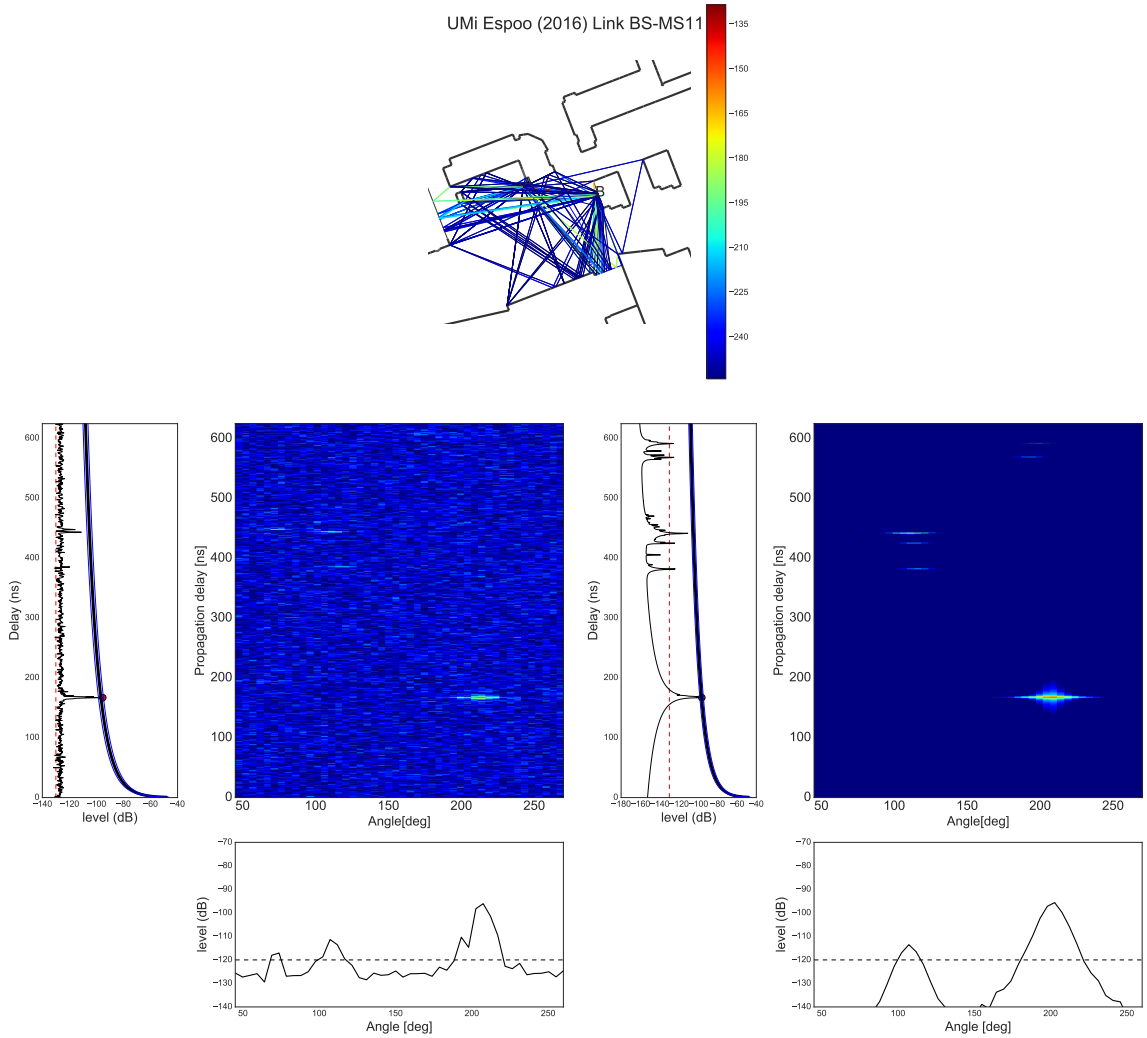

Figure A.11.: 32.6 GHz UMi Espoo: BS-MS 11 PDP (left) PADP (middle) PAP (bottom) for measurement (left) and RT simulation (right)

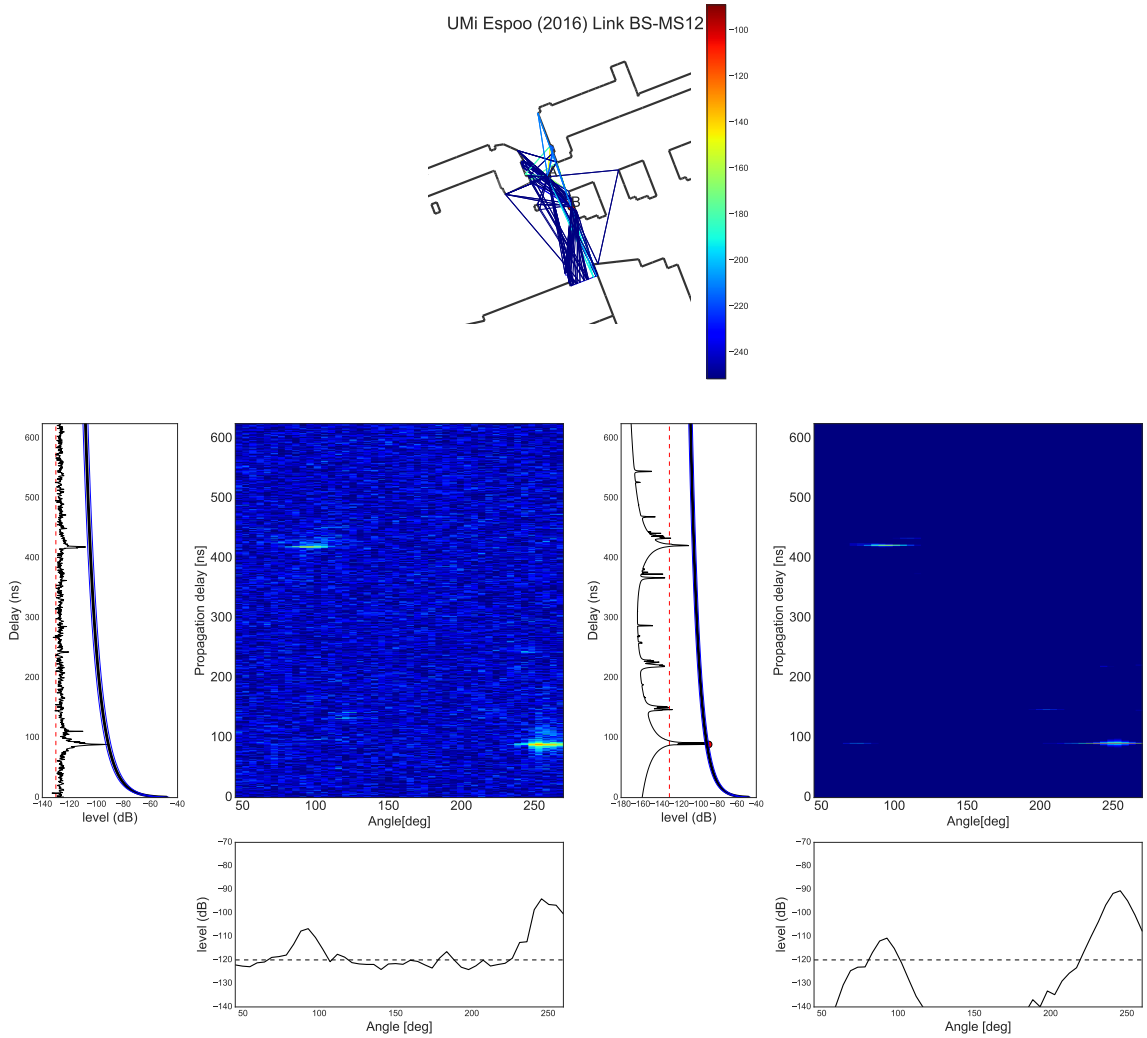

Figure A.12.: 32.6 GHz UMi Espoo: BS-MS 12 PDP (left) PADP (middle) PAP (bottom) for measurement (left) and RT simulation (right)

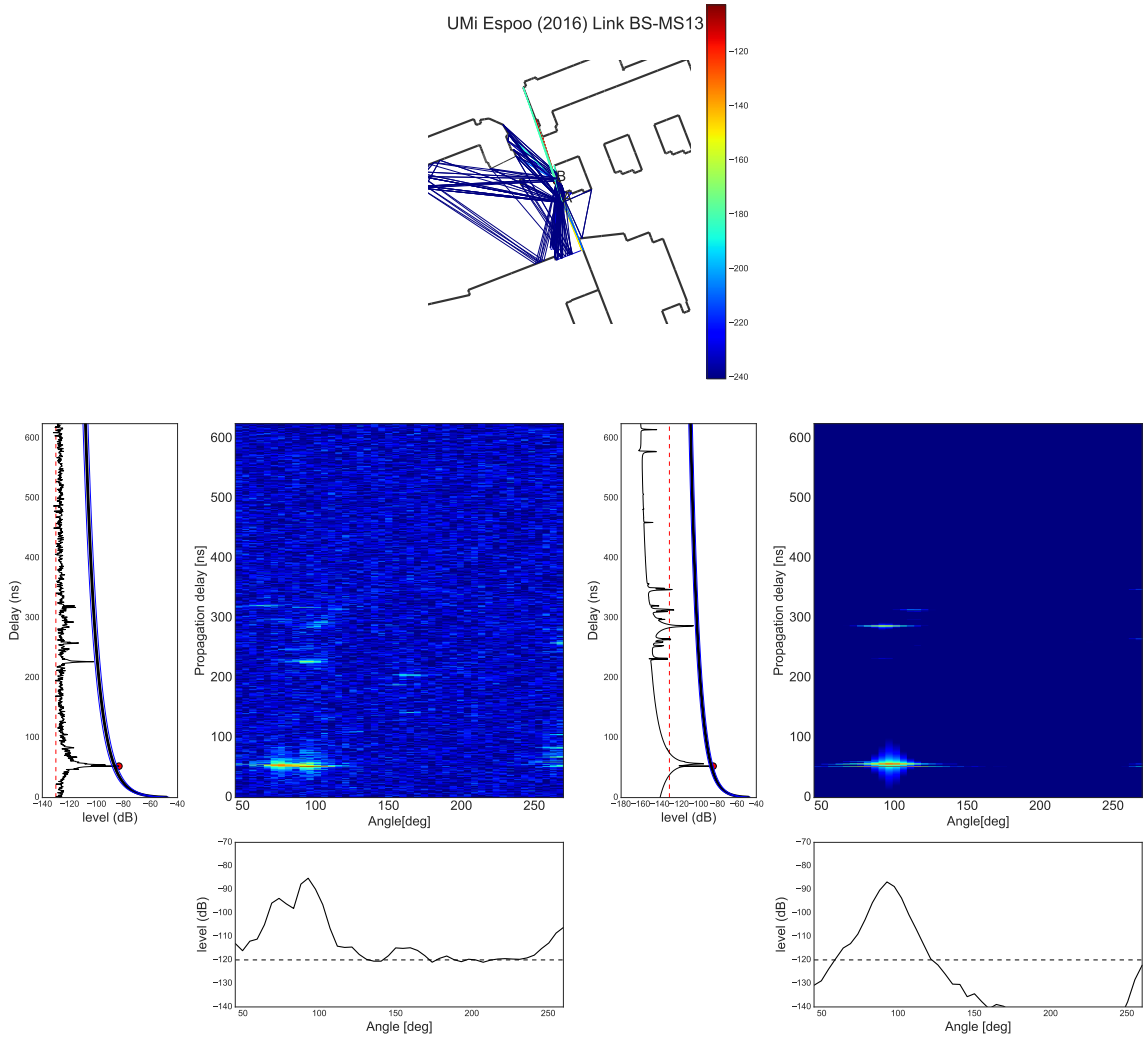

Figure A.13.: 32.6 GHz UMi Espoo: BS-MS 13 PDP (left) PADP (middle) PAP (bottom) for measurement (left) and RT simulation (right)

Appendix B

Path `back-projection`

This appendix provides an exhausive representation of the `back-projection` method applied to the measured UMi LOS scenarios. The MS locations are represented in green stars while the BS location is in a blue square. Some lamp-posts, represented in green diedre, are considered in the layout. Furthermore, some photos are associated to the results for analysis convenient.
Generally, the `back-projection` method highlights the effect of the scattering environment where the ground, building window, building wall and publicity-board are contributing significantly. Furthermore, urban furniture distributed on the measurement site such as metallic lamp-posts and road-signs are found to bring non negligible energy.

(a)

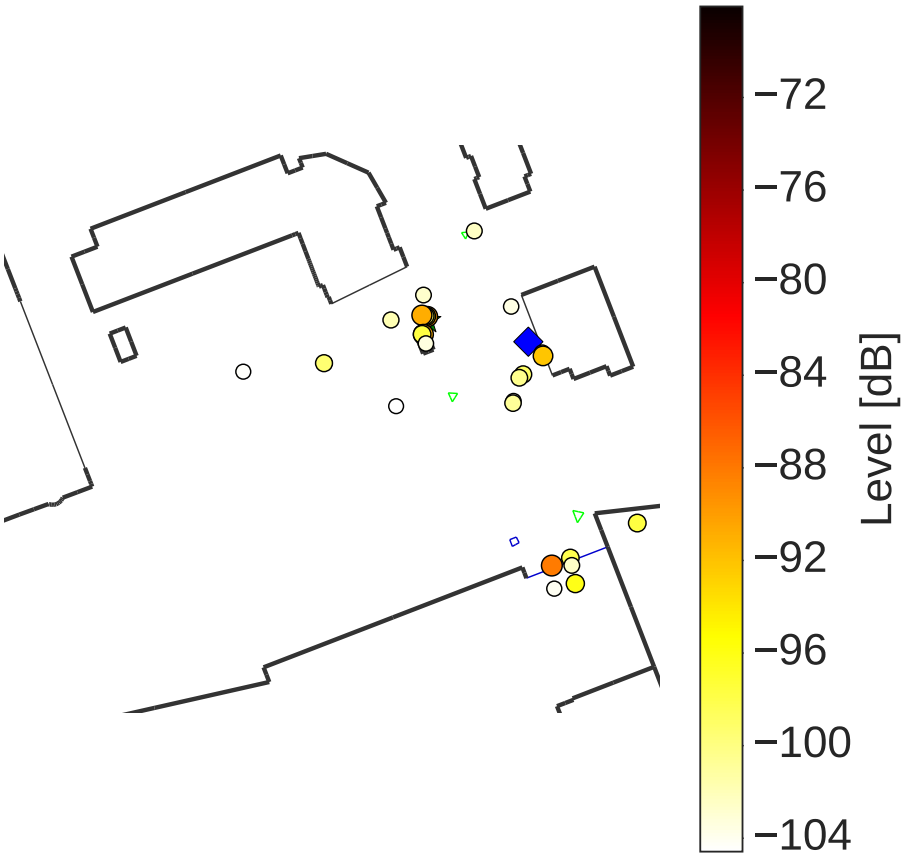

(b)

Figure B.1.: 32.6 GHz UMi Espoo: path `back-projection` applied to the link BS-MS 1. Some metallic road-signs were located near the MS1 position as it can be seen in Fig. 3.16.b and stated in Table 3.7.

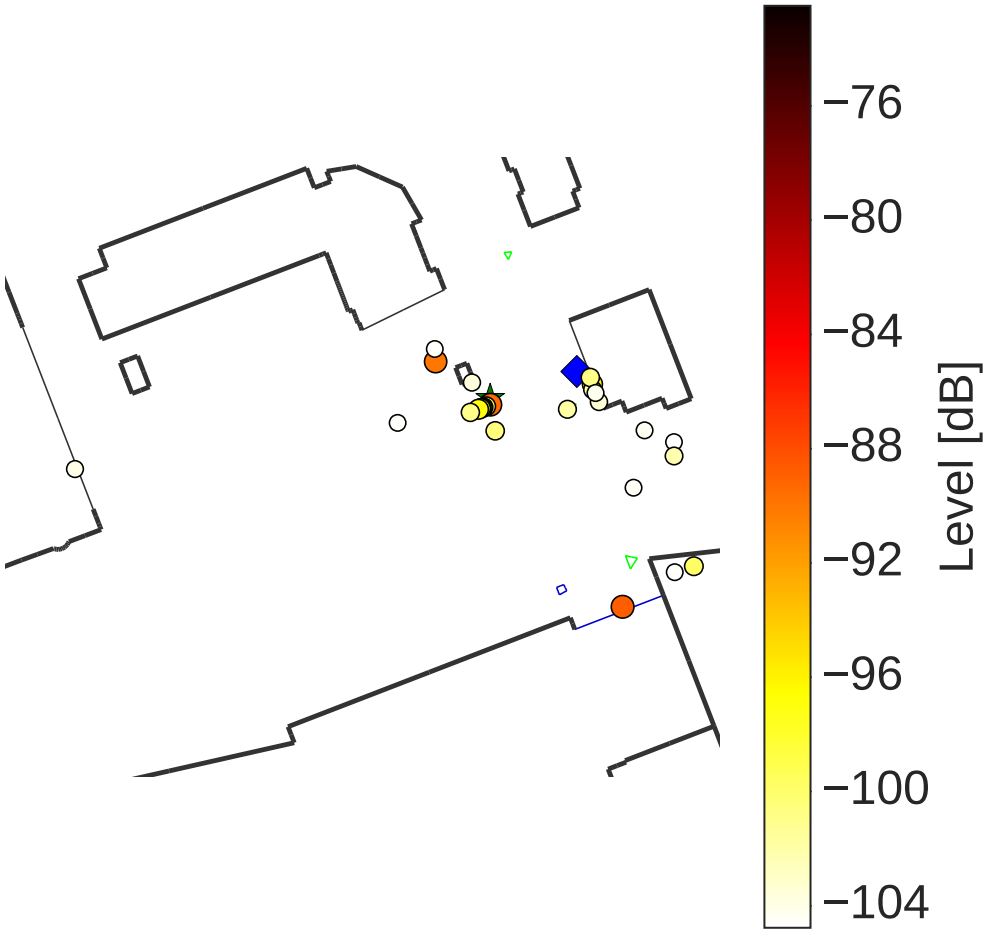

Figure B.2.: 32.6 GHz UMi Espoo: path `back-projection` applied to the link BS-MS 2. Notice that one lamp-post was located near the BS while another one was located near MS 2.

(a)

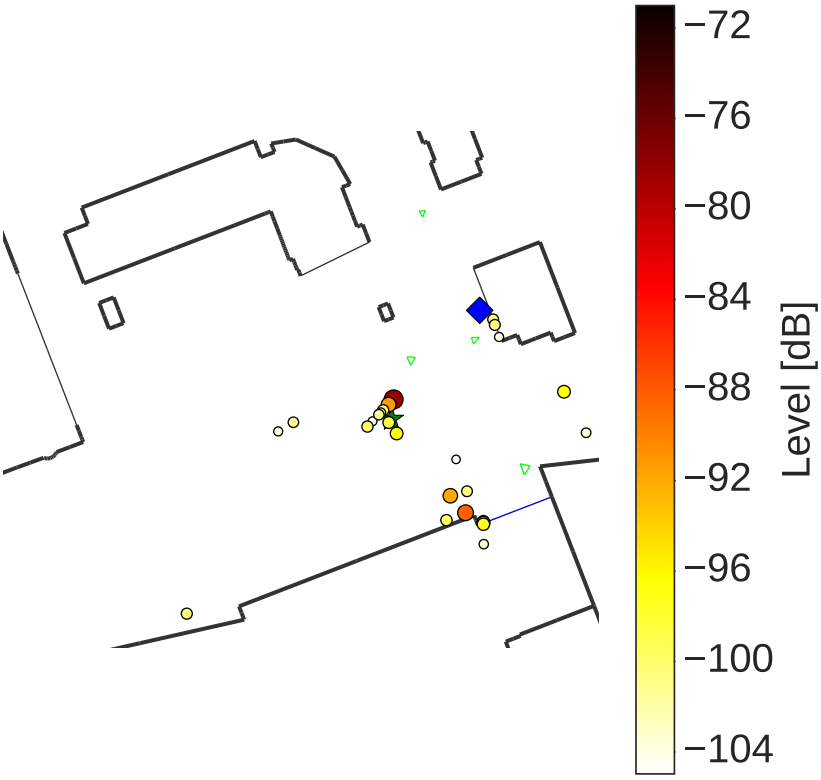

(b)

Figure B.3.: 32.6 GHz UMi Espoo: path `back-projection` applied to the link BS-MS 4. As seen in (a), the MS was surrounded by cars, lamp-posts, bushes, road-signs.

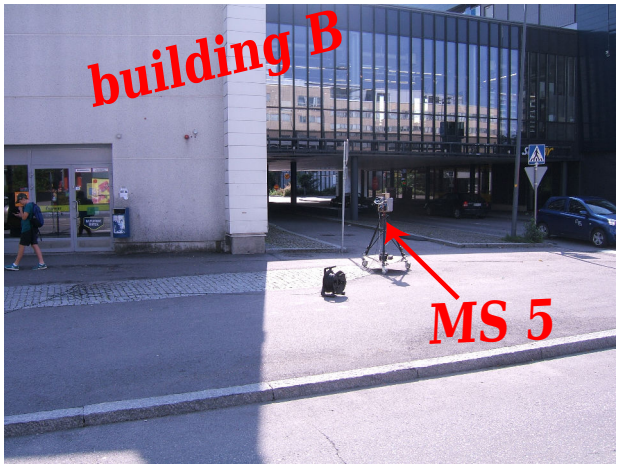

(a)

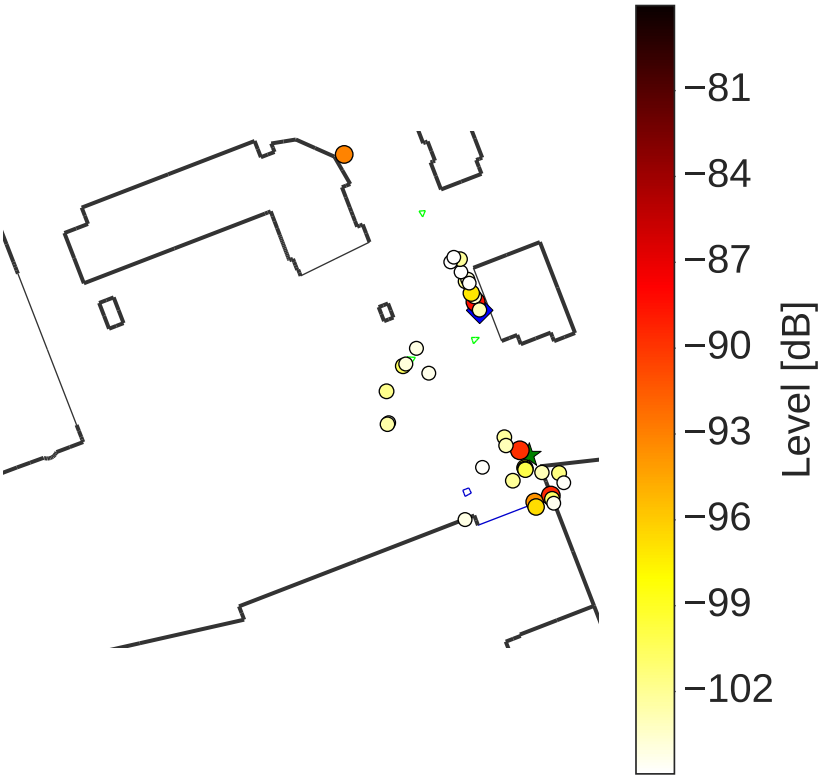

(b)

Figure B.4.: 32.6 GHz UMi Espoo: path `back-projection` applied to the link BS-MS 5. Road-signs and lamp-posts were located near the MS as illustrated in (a).

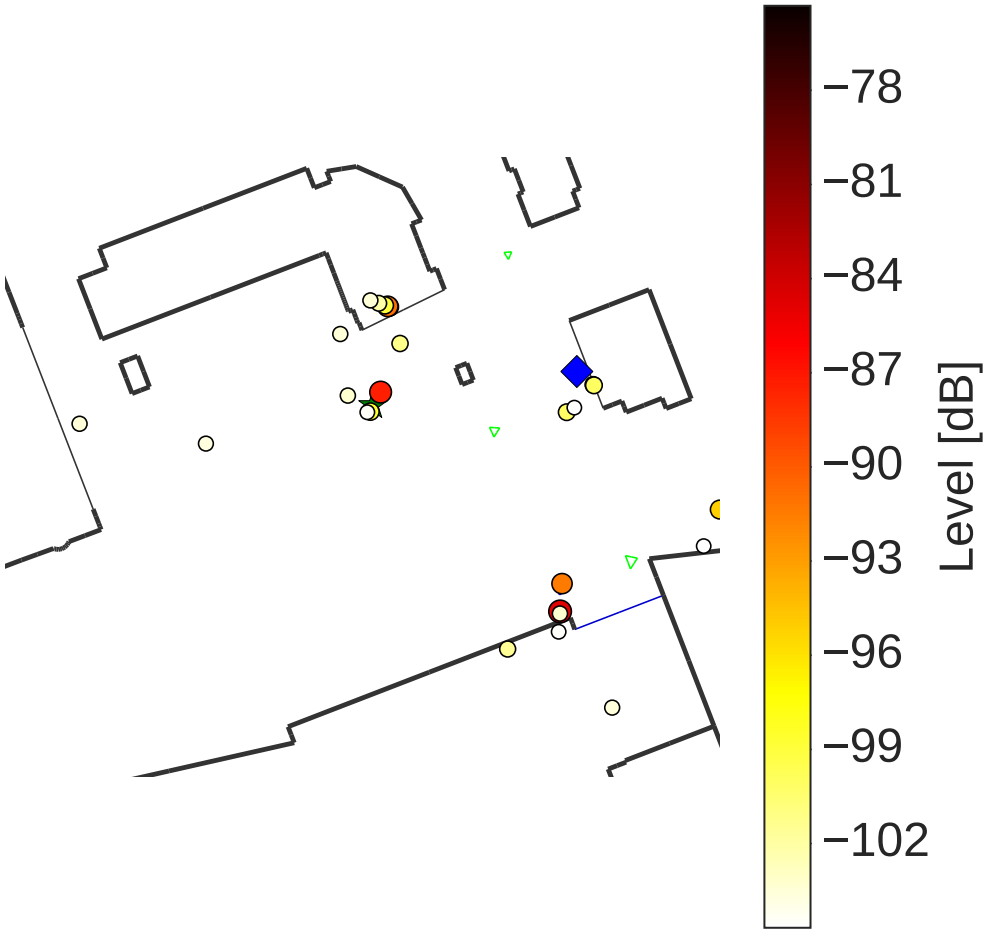

Figure B.5.: 32.6 GHz UMi Espoo: path `back-projection` applied to the link BS-MS 6

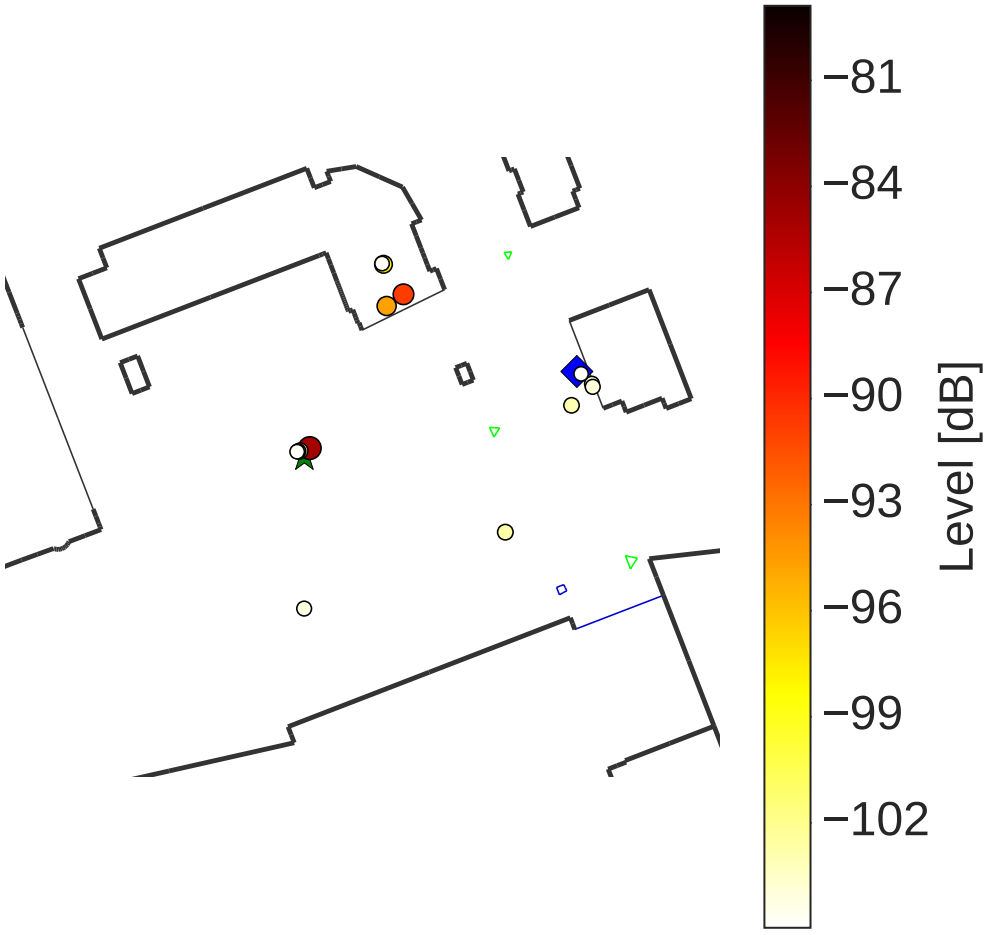

Figure B.6.: 32.6 GHz UMi Espoo: path `back-projection` applied to the link BS-MS 7

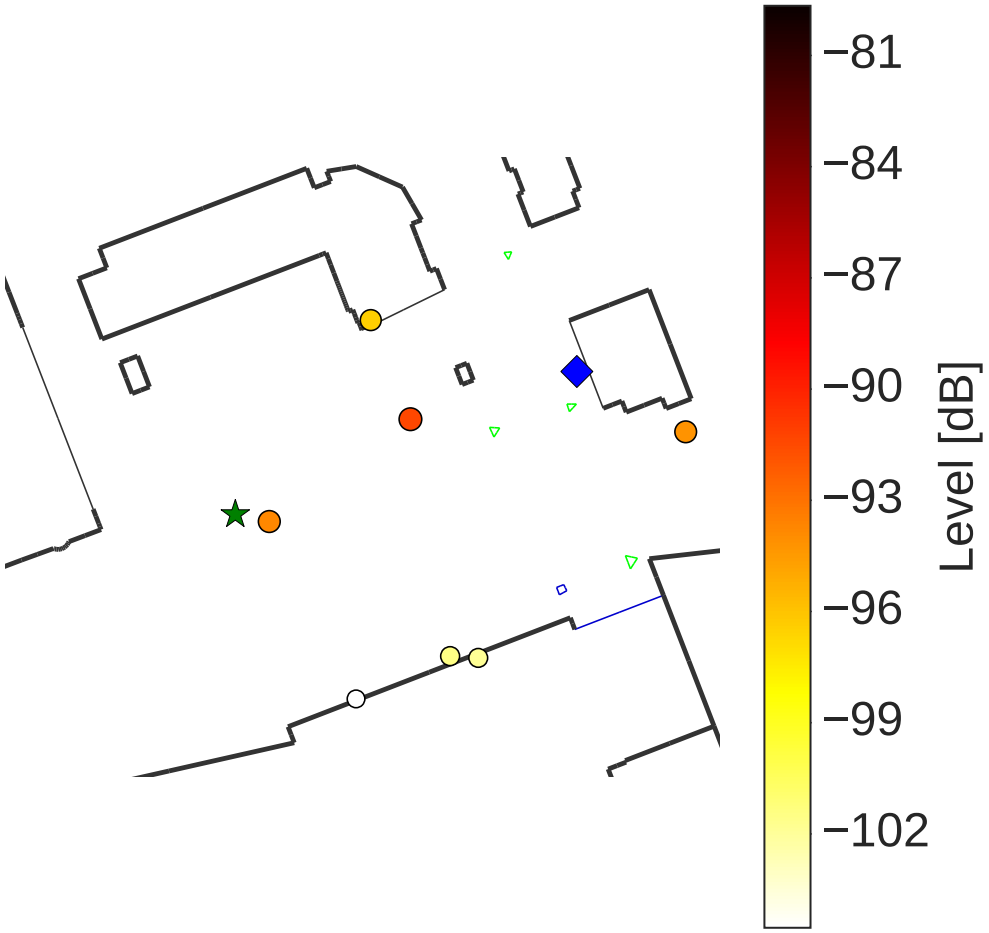

Figure B.7.: 32.6 GHz UMi Espoo: path `back-projection` applied to the link BS-MS 8

(a)

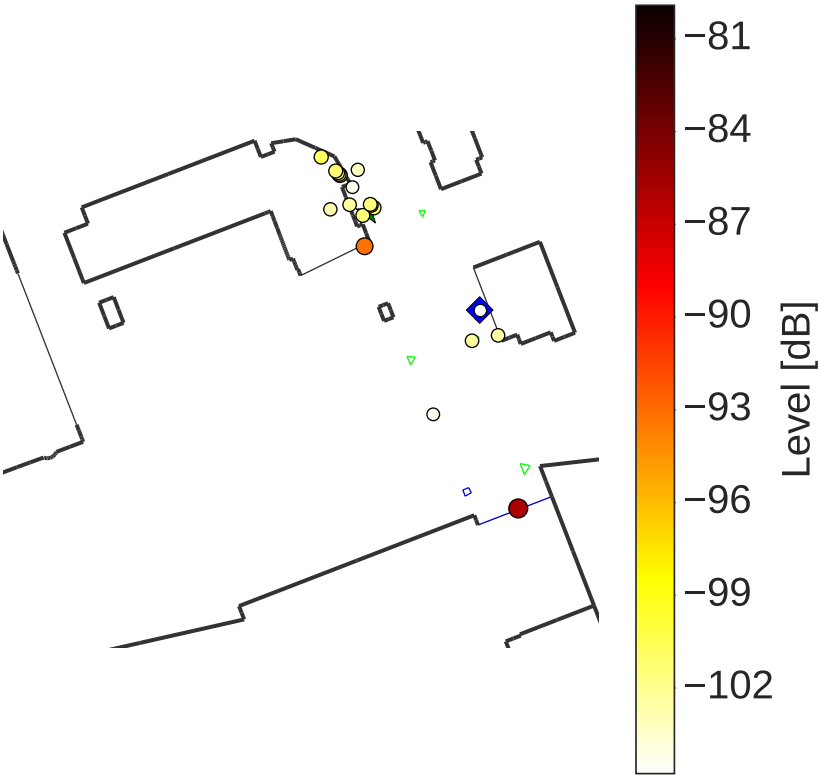

(b)

Figure B.8.: 32.6 GHz UMi Espoo: path `back-projection` applied to the link BS-MS 9 (b) and the associated photo of the MS location (a).

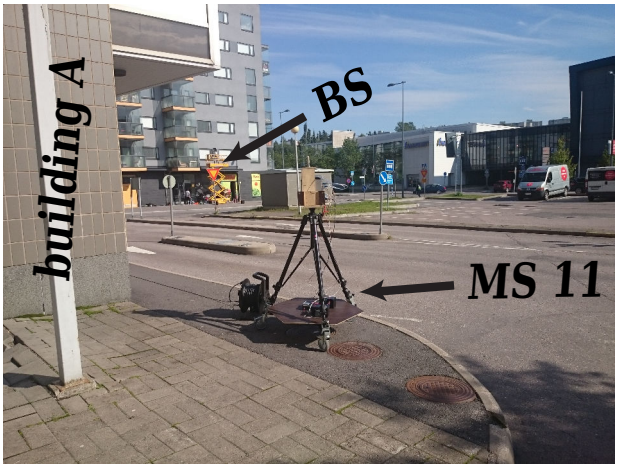

(a)

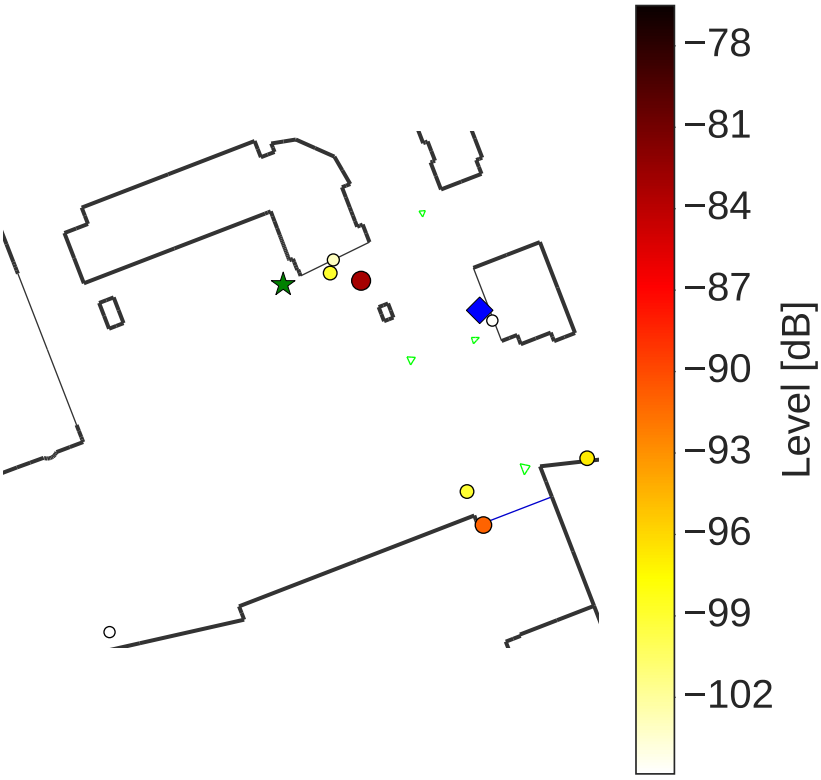

(b)

Figure B.9.: 32.6 GHz UMi Espoo: path `back-projection` applied to the link BS-MS 11 (b) and the associated photo of the MS location (a).

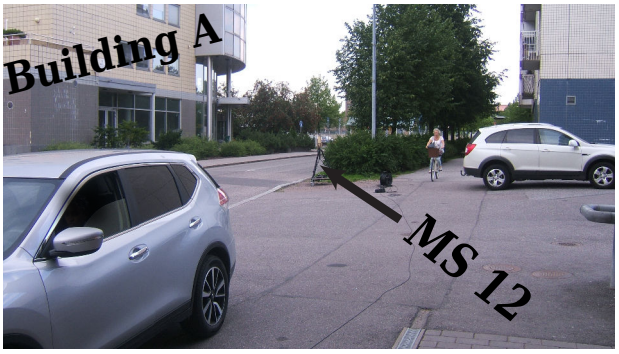

(a)

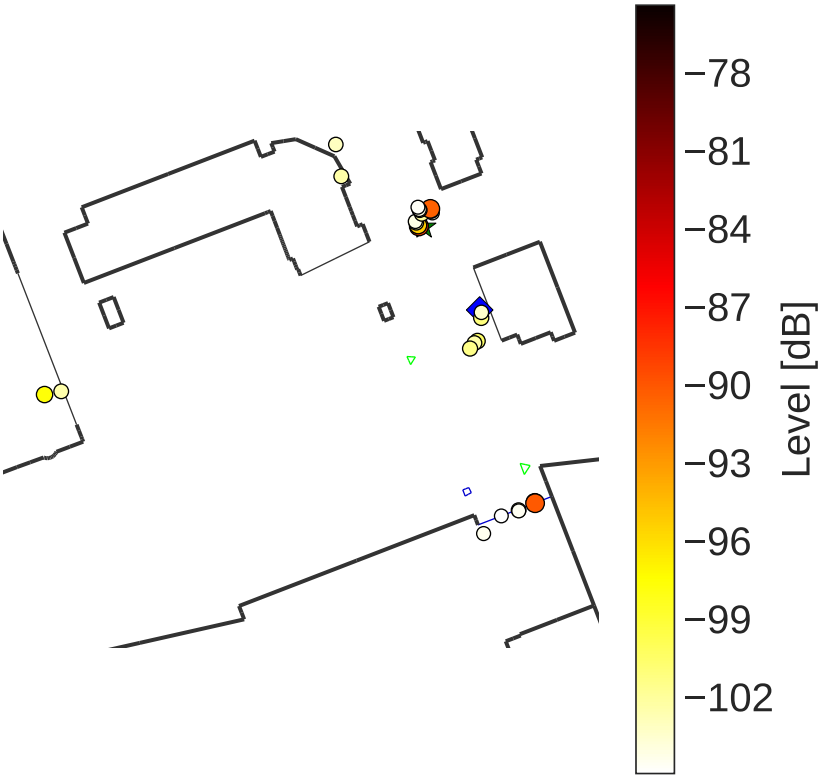

(b)

Figure B.10.: 32.6 GHz UMi Espoo: path `back-projection` applied to the link BS-MS 12. As shown in (a), some bushes, cars and lamp-posts were near the MS location.

(a)

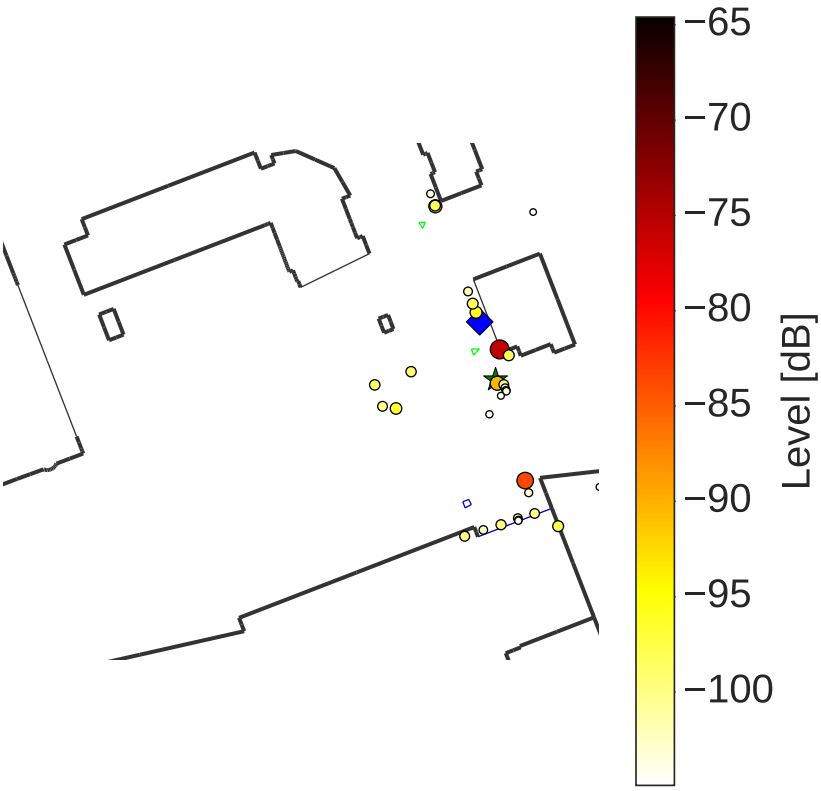

(b)

Figure B.11.: 32.6 GHz UMi Espoo: path `back-projection` applied to the link BS-MS13. The photo in (a) shows the presence of some road-signs and other metallic objects.

Personal Contributions

[BVNHHU17] M. D. Balde, J. Vehmas, S. L. H. Nguyen, K. Haneda, H. Houas and B. Uguen. A 32 GHz urban micro cell measurement campaign for 5G candidate spectrum region. 11th European Conference on Antennas and Propagation (EUCAP), March 2017, Paris, France.

[BABLU16] M. D. Balde, S. Avrillon, C. Brousseau, D. Lemur, and B. Uguen. Spatial scanner channel sounder for space diversity studies. 10th European Conference on Antennas and Propagation (EUCAP), April 2016, Davos, Switzerland

[BKUHN] M. D. Balde, A. Karttunen, B. Uguen, K. Haneda, and S. L. H. Nguyen. Time Varying Multi-path Components at 28 GHz from Mobile Channel Sounding. CA15104 TD(17) 04067, Technical Meeting, IRACON, May 2017, Lund, Sweden.

[BU17] M. D. Balde, and B. Uguen. MU-MIMO Performances Analysis from Aggregated Measurement Channel in Indoor Environment. CA15104 TD(16) 01063, Technical Meeting, IRACON, June 2016, Lille, France.

Paper [BVNHHU17] and Paper [BABLU16] are presented in an international conference with peer reviews while Paper [BKUHN] and Paper [BU17] were presented during the IRACON meetings.

A 32 GHz urban microcellular measurement campaign is presented in Paper [BVNHHU17]. A path loss model in line-of-sight (LOS) for the fifth-generation (5G) candidate frequency band 31.8-33.4 GHz is provided, and different key channel metrics such as omnidirectional path loss, angular and delay spreads and Rician K-factor are investigated. The investigation shows that no significant difference between the 28 GHz and 32 GHz frequency bands w.r.t the studied metrics.

Paper [BABLU16] (not addressed in this thesis) presents a versatile spatial scanner Vector Network Analyser (VNA) channel sounder for indoor and outdoor scenarios exploiting a four axis positioner and optical transposition devices which allow a large separation between Tx and Rx antennas. This channel sounder can be used over several frequency bands of interest for the development of future multi antenna systems. The spatial channel sounder allows to acquire a large number of static channel matrices through a properly sampled region of space in order to retrieve the time-varying behaviour of the MIMO channel. A measurement run of a 4×8 MIMO channel acquired along a 0.7 m vertical translation are presented here in order to illustrate the capabilities of the sounder.

TD [BKUHN] discusses the time-variant multi-path components (MPCs) observed during a wideband measurement campaign performed at 28 GHz in two realistic indoor environments.

TD [BU17] (not addressed in this thesis) explores the performances of a synthetic Indoor MU-MIMO. The measurements were performed in an office environment covering a frequency band from 1.8 GHz to 2.2 GHz while antennas were folded dipole designed in vertical polarization. Data were acquired by a Vector Network Analyzer (VNA) based channel sounder associated to a four axes scanner. An uniform (1×8) linear array (ULA) was placed at four different heights to emulate 8, 16, 24 and 32 virtual antenna arrays at the transmitter side while an ULA of four antennas are considered at the receiver side. Various measurements were addressed at three different NLOS configurations. An analysis of the the spectral MU-MIMO channel matrices are provided.

Bibliography

[1] 2016-2021 White Paper Cisco Visual Networking Index: Global Mobile Data Traffic Forecast Update. https://www.cisco.com/c/en/us/solutions/collateral/service-provider/visual-networking-index-vni/mobile-white-paper-c11-520862.html, 2016.

[2] Ericson: MICROWAVE TOWARDS 2020 Report. https://www.ericsson.com/assets/local/microwave-outlook/documents/microwave-towards-2020-report-2014.pdf, 2014.

[3] W. Roh, J. Y. Seol, J. Park, B. Lee, J. Lee, Y. Kim, J. Cho, K. Cheun, and F. Aryanfar. Millimeter-wave beamforming as an enabling technology for 5g cellular communications: theoretical feasibility and prototype results. IEEE Communications Magazine, 52(2):106–113, February 2014.

[4] Y. Wang, J. Li, L. Huang, Y. Jing, A. Georgakopoulos, and P. Demestichas. 5g mobile: Spectrum broadening to higher-frequency bands to support high data rates. IEEE Vehicular Technology Magazine, 9(3):39–46, Sept 2014.

[5] 5G: ISSUES ARCEP and CHALLENGES. https://www.arcep.fr/uploads/tx_gspublication/Report-5G-issues-challenges-march2017.pdf, March 2017.

[6] 5Gamerica: 5G spectrum recommendations. http://www.5gamericas.org/files/9114/9324/1786/5GA_5G_Spectrum_Recommendations_2017_FINAL.pdf, April 2017.

[7] D. Lockie and D. Peck. High-data-rate millimeter-wave radios. IEEE Microwave Magazine, 10(5):75–83, August 2009.

[8] F. Gutierrez Jr., T. S. Rappaport, and J. Murdock. Millimeter-wave cmos antennas and rfic parameter extraction for vehicular applications. In 2010 IEEE 72nd Vehicular Technology Conference - Fall, pages 1–6, Sept 2010.

[9] A. Molish. Wireless Communications, 2nd Edition, Book. Wiley, 2010.

[10] RECOMMENDATION ITU-R P.838-3. Weather applications and products enabled through vehicle infrastructure integration (vii). `https://www.itu.int/dms_pubrec/itu-r/rec/p/R-REC-P.838-3-200503-I!!PDF-E.pdf`, 2005.

[11] T. S. Rappaport, S. Sun, R. Mayzus, H. Zhao, Y. Azar, K. Wang, G. N. Wong, J. K. Schulz, M. Samimi, and F. Gutierrez. Millimeter wave mobile communications for 5g cellular: It will work! IEEE Access, 1:335–349, 2013.

[12] Recommendation itu-r p.2040-1 effects of building materials and structures on radiowave propagation above about 100 mhz. `http://www.itu.int/rec/R-REC-P.2040-1-201507-I`, July 2015.

[13] C. W. I. Pistorius D. A. Mcnamara and J. A. G. Malherbe. Introduction to the Uniform Geometrical Theory of Diffraction. Artech House Publishers, 1990. Artech House Publishers, 1990.

[14] METIS. Deliverable d1.4 metis channel models. `https://www.metis2020.com/wp-content/uploads/METIS_D1.4_v3.pdf`, jul 2015.

[15] 3GPP. Technical specification group radio access network; study on channel model for frequencies from 0.5 to 100 ghz. `http://www.3gpp.org/DynaReport/38-series.htm`, 2016.

[16] J. E. Berg. A recursive method for street microcell path loss calculations. In Proceedings of 6th International Symposium on Personal, Indoor and Mobile Radio Communications, volume 1, pages 140–143 vol.1, Sep 1995.

[17] Jonas Medbo Pekka Kyosti. A channel model for 5g evaluations. 2015.

[18] Hao Xu, V. Kukshya, and T. S. Rappaport. Spatial and temporal characteristics of 60-ghz indoor channels. IEEE Journal on Selected Areas in Communications, 20(3):620–630, Apr 2002.

[19] A. Maltsev, R. Maslennikov, A. Sevastyanov, A. Khoryaev, and A. Lomayev. Experimental investigations of 60 ghz wlan systems in office environment. IEEE Journal on Selected Areas in Communications, 27(8):1488–1499, October 2009.

[20] J. Lu, D. Steinbach, P. Cabrol, P. Pietraski, and R. V. Pragada. Propagation characterization of an office building in the 60 ghz band. In The 8th European Conference on Antennas and Propagation (EuCAP 2014), pages 809–813, April 2014.

[21] T. S. Rappaport, F. Gutierrez, E. Ben-Dor, J. N. Murdock, Y. Qiao, and J. I. Tamir. Broadband millimeter-wave propagation measurements and models using adaptive-beam antennas for outdoor urban cellular communications. IEEE Transactions on Antennas and Propagation, 61(4):1850–1859, April 2013.

[22] J. Poutanen, J. Salmi, K. Haneda, V. M. Kolmonen, F. Tufvesson, and P. Vainikainen. Propagation characteristics of dense multipath components. IEEE Antennas and Wireless Propagation Letters, 9:791–794, 2010.

[23] T. Pedersen, G. Steinbock, and B. H. Fleury. Modeling of reverberant radio channels using propagation graphs. IEEE Transactions on Antennas and Propagation, 60(12):5978–5988, Dec 2012.

[24] C. A. L. Diakhate, J. M. Conrat, J. C. Cousin, and A. Sibille. Millimeter-wave outdoor-to-indoor channel measurements at 3, 10, 17 and 60 ghz. In 2017 11th European Conference on Antennas and Propagation (EUCAP), pages 1798–1802, March 2017.

[25] 3GPP16 R1 161688. Measurements of path and penetration losses at multiple carrier frequencies. `http://www.3gpp.org/ftp/TSG_RAN/WG1_RL1/TSGR1_AH/LTE_ChM_1603/Docs/`, mar 2016.

[26] mmMAGIC. D2.2 measurement results and final mmmagic channel models. Technical report, Millimetre - Wave Based Mobile Radio Access Network for Fifth Generation Integrated Communications (mmMAGIC), may 2017.

[27] H. Zhao, R. Mayzus, S. Sun, M. Samimi, J. K. Schulz, Y. Azar, K. Wang, G. N. Wong, F. Gutierrez, and T. S. Rappaport. 28 ghz millimeter wave cellular communication measurements for reflection and penetration loss in and around buildings in new york city. In 2013 IEEE International Conference on Communications (ICC), pages 5163–5167, June 2013.

[28] Jacqueline Ryan, George R. MacCartney Jr., and Theodore S. Rappaport. Indoor office wideband penetration loss measurements at 73 ghz. CoRR, abs/1703.08030, 2017.

[29] Jr. R. C. Daniels T. S. Rappaport, R. W. Heath and J. N. Murdock. Millimeter Wave Wireless Communications. Pearson/Prentice Hall, 2015.

[30] G. R. MacCartney, M. K. Samimi, and T. S. Rappaport. Exploiting directionality for millimeter-wave wireless system improvement. In 2015 IEEE International Conference on Communications (ICC), pages 2416–2422, June 2015.

[31] M. K. Samimi, G. R. MacCartney, S. Sun, and T. S. Rappaport. 28 ghz millimeter-wave ultrawideband small-scale fading models in wireless channels. In 2016 IEEE 83rd Vehicular Technology Conference (VTC Spring), pages 1–6, May 2016.

[32] Wei Fan, Ines Carton, Jesper Ø. Nielsen, Kim Olesen, and Gert F. Pedersen. Measured wideband characteristics of indoor channels at centimetric and millimetric bands. EURASIP Journal on Wireless Communications and Networking, 2016(1):58, Feb 2016.

[33] I. Rodriguez, H. C. Nguyen, T. B. Sorensen, J. Elling, J. A. Holm, P. Mogensen, and B. Vejlgaard. Analysis of 38 ghz mmwave propagation characteristics of urban scenarios. In Proceedings of European Wireless 2015; 21th European Wireless Conference, pages 1–8, May 2015.

[34] T. S. Rappaport, G. R. MacCartney, M. K. Samimi, and S. Sun. Wideband millimeter-wave propagation measurements and channel models for future wireless communication system design. IEEE Transactions on Communications, 63(9):3029–3056, Sept 2015.

[35] Moray Rumney. Testing 5g: Time to throw away the cables. Microwave Journal, nov 2016.

[36] K. Haneda, J. Jarvelainen, A. Karttunen, M. Kyro, and J. Putkonen. A statistical spatio-temporal radio channel model for large indoor environments at 60 and 70 ghz. IEEE Transactions on Antennas and Propagation, 63(6):2694–2704, June 2015.

[37] J. S. Lu, P. Cabrol, D. Steinbach, and R. V. Pragada. Measurement and characterization of various outdoor 60 ghz diffracted and scattered paths. In MILCOM 2013 - 2013 IEEE Military Communications Conference, pages 1238–1243, Nov 2013.

[38] M. Kyro, K. Haneda, J. Simola, K. i. Takizawa, H. Hagiwara, and P. Vainikainen. Statistical channel models for 60 ghz radio propagation in hospital environments. IEEE Transactions on Antennas and Propagation, 60(3):1569–1577, March 2012.

[39] C. Gustafson, K. Haneda, S. Wyne, and F. Tufvesson. On mm-wave multipath clustering and channel modeling. IEEE Transactions on Antennas and Propagation, 62(3):1445–1455, March 2014.

[40] M. K. Samimi and T. S. Rappaport. 3-d millimeter-wave statistical channel model for 5g wireless system design. IEEE Transactions on Microwave Theory and Techniques, 64(7):2207–2225, July 2016.

[41] J. Karedal, F. Tufvesson, N. Czink, A. Paier, C. Dumard, T. Zemen, C. F. Mecklenbrauker, and A. F. Molisch. A geometry-based stochastic mimo model for vehicle-to-vehicle communications. IEEE Transactions on Wireless Communications, 8(7):3646–3657, July 2009.

[42] T. Pedersen and B. H. Fleury. Radio channel modelling using stochastic propagation graphs. In 2007 IEEE International Conference on Communications, pages 2733–2738, June 2007.

[43] L. Tian, V. Degli-Esposti, E. M. Vitucci, and X. Yin. Semi-deterministic radio channel modeling based on graph theory and ray-tracing. IEEE Transactions on Antennas and Propagation, 64(6):2475–2486, June 2016.

[44] J. Zhang, C. Tao, L. Liu, and R. Sun. A study on channel modeling in tunnel scenario based on propagation-graph theory. In 2016 IEEE 83rd Vehicular Technology Conference (VTC Spring), pages 1–5, May 2016.

[45] J. Chen, X. Yin, L. Tian, and M. D. Kim. Millimeter-wave channel modeling based on a unified propagation graph theory. IEEE Communications Letters, 21(2):246–249, Feb 2017.

[46] G. Steinbock, A. Karstensen, P. Kyosti, and A. Hekkala. A 5g hybrid channel model considering rays and geometric stochastic propagation graph. In 2016 IEEE 27th Annual International Symposium on Personal, Indoor, and Mobile Radio Communications (PIMRC), pages 1–6, Sept 2016.

[47] N. Cardona. Cooperative Radio Communications for Green Smart Environments. River Publishers series in communications. River Publishers, 2016.

[48] Sebastien Reynaud, Rodolphe Vauzelle, Alain Reineix, and Christophe Guiffaut. A hybrid fdtd/utd radiowave propagation modeling: Application to indoor channel simulations. Microwave and Optical Technology Letters, 49(6):1312–1320, 2007.

[49] R. Chandra and A. J. Johansson. An analytical link-loss model for on-body propagation around the body based on elliptical approximation of the torso with arms' influence included. IEEE Antennas and Wireless Propagation Letters, 12:528–531, 2013.

[50] R. Chandra and A. J. Johansson. A link loss model for the on-body propagation channel for binaural hearing aids. IEEE Transactions on Antennas and Propagation, 61(12):6180–6190, Dec 2013.

[51] U. T. Virk, K. Haneda, V. M. Kolmonen, J. F. Wagen, and P. Vainikainen. Full-wave characterization of indoor office environment for accurate coverage analysis. In 2013 International Conference on Electromagnetics in Advanced Applications (ICEAA), pages 1197–1200, Sept 2013.

[52] Google earth web. `https://earth.google.com/web`.

[53] OSM: Open Street Map. `https://josm.openstreetmap.de/`.

[54] S. Baek, Y. Chang, S. Hur, J. Hwang, and B. Kim. 3-dimensional large-scale channel model for urban environments in mmwave frequency. In 2015 IEEE International Conference on Communication Workshop (ICCW), pages 1220–1225, June 2015.

[55] S. Hur, S. Baek, B. Kim, Y. Chang, A. F. Molisch, T. S. Rappaport, K. Haneda, and J. Park. Proposal on millimeter-wave channel modeling for 5g cellular system. IEEE Journal of Selected Topics in Signal Processing, 10(3):454–469, April 2016.

[56] Franco Fuschini, Enrico M. Vitucci, Marina Barbiroli, Gabriele Falciasecca, and Vittorio Degli-Esposti. Ray tracing propagation modeling for future small-cell and indoor applications: A review of current techniques. Radio Science, 50(6):469–485, 2015. 2015RS005659.

[57] N. Amiot, M. Laaraiedh, and B. Uguen. Pylayers: An open source dynamic simulator for indoor propagation and localization. In 2013 IEEE International Conference on Communications Workshops (ICC), pages 84–88, June 2013.

[58] G. Steinbock, M. Gan, P. Meissner, E. Leitinger, K. Witrisal, T. Zemen, and T. Pedersen. Hybrid model for reverberant indoor radio channels using rays and graphs. IEEE Transactions on Antennas and Propagation, 64(9):4036–4048, Sept 2016.

[59] M. Peter, W. Keusgen, and R. Felbecker. Measurement and ray-tracing simulation of the 60 ghz indoor broadband channel: Model accuracy and parameterization. In The Second European Conference on Antennas and Propagation, EuCAP 2007, pages 1–8, Nov 2007.

[60] J. Jamsa, M. Luimula, S. Pieska, V. Brax, O. Saukko, and P. Verronen. Indoor positioning with laser scanned models in the metal industry. In 2010 Ubiquitous Positioning Indoor Navigation and Location Based Service, pages 1–9, Oct 2010.

[61] J. Jarvelainen and K. Haneda. Sixty gigahertz indoor radio wave propagation prediction method based on full scattering model. Radio Science, 49(4):293–305, April 2014.

[62] J. Jarvelainen, K. Haneda, and A. Karttunen. Indoor propagation channel simulations at 60 ghz using point cloud data. IEEE Transactions on Antennas and Propagation, 64(10):4457–4467, Oct 2016.

[63] U. T. Virk, J. F. Wagen, and K. Haneda. Simulating specular reflections for point cloud geometrical database of the environment. In 2015 Loughborough Antennas Propagation Conference (LAPC), pages 1–5, Nov 2015.

[64] J. Jarvelainen, M. Kurkela, and K. Haneda. Impacts of room structure models on the accuracy of 60 ghz indoor radio propagation prediction. IEEE Antennas and Wireless Propagation Letters, 14:1137–1140, 2015.

[65] 3GPP. 3rd generation partnership project; technical specification group radio access network; spatial channel model ahg (combined ad-hoc from 3gpp and 3gpp2). `ftp://www.3gpp.org/tsg_ran/WG1_RL1/3GPP_3GPP2_SCM/ConfCall-8-20021121/SCM-077-SCM%20Text%20v2.0.pdf`, 2002.

[66] D. S. Baum, J. Hansen, and J. Salo. An interim channel model for beyond-3g systems: extending the 3gpp spatial channel model (scm). In 2005 IEEE 61st Vehicular Technology Conference, volume 5, pages 3132–3136 Vol. 5, May 2005.

[67] 3GPP. 3rd generation partnership project; technical specification group radio access network; study on channel model for frequency spectrum above 6 ghz (release 14), v14.2.0, tech. rep., 2016.

[68] WINNER. Final report on link level and system level channel models deliverable 5.4 v1.4. `http://projects.celtic-initiative.org/winner+/DeliverableDocuments/D5.4.pdf`, 2005.

[69] WINNER. Winner ii channel models, deliverable 1.1.2 v1.2. `https://cept.org/files/8339/winner2%20-%20final%20report.pdf`, 2010.

[70] WINNER. Winner+ final channel models, deliverable 5.3. `http://projects.celtic-initiative.org/winner+/WINNER+%20Deliverables/D5.3_v1.0.pdf`, 2010.

[71] Afif Osseiran, Veljko Stankovic, Eduard Jorswieck, Thorsten Wild, Martin Fuchs, and Magnus Olsson. A mimo framework for 4g systems: Winner concept and results. In 2007 IEEE 8th Workshop on Signal Processing Advances in Wireless Communications, pages 1–5, June 2007.

[72] Tommi Jämsä, Juha Meinilä, Pekka Kyösti, Daniel S. Baum, Hassan El-Sallabi, Terhi Rautiainen, Christian Schneider, Marko Milojevic, and Per Zetterberg. Overview of WINNER channel modelling activities. In Proc. Wirless World Research Forum Meeting 15, December 2005.

[73] S. Payami and F. Tufvesson. Channel measurements and analysis for very large array systems at 2.6 ghz. In 2012 6th European Conference on Antennas and Propagation (EUCAP), pages 433–437, March 2012.

[74] Pekka Kyosti Vuokko Nurmela, Tommi Jamsa. Channel modelling for device-to-device scenarios. td(13)08009, technical report, ghent-belgium. `https://www.metis2020.com/wp-content/uploads/publications/COST_IC1004_2013_Nurmela_etal_ChannelModellingForD2DScenarios.pdf`, 2013.

[75] L. Liu, C. Oestges, J. Poutanen, K. Haneda, P. Vainikainen, F. Quitin, F. Tufvesson, and P. D. Doncker. The cost 2100 mimo channel model. IEEE Wireless Communications, 19(6):92–99, December 2012.

[76] J. Poutanen, K. Haneda, Lingfeng Liu, C. Oestges, F. Tufvesson, and P. Vainikainen. Parameterization of the cost 2100 mimo channel model in indoor scenarios. In Proceedings of the 5th European Conference on Antennas and Propagation (EUCAP), pages 3606–3610, April 2011.

[77] M. Zhu, G. Eriksson, and F. Tufvesson. The cost 2100 channel model: Parameterization and validation based on outdoor mimo measurements at 300 mhz. IEEE Transactions on Wireless Communications, 12(2):888–897, February 2013.

[78] J. Medbo, P. Kyosti, K. Kusume, L. Raschkowski, K. Haneda, T. Jamsa, V. Nurmela, A. Roivainen, and J. Meinila. Radio propagation modeling for 5g mobile and wireless communications. IEEE Communications Magazine, 54(6):144–151, June 2016.

[79] I. Carton, Wei Fan, P. Kyosti, and G. F. Pedersen. Validation of 5g metis map-based channel model at mmwave bands in indoor scenarios. In 2016 10th European Conference on Antennas and Propagation (EuCAP), pages 1–5, April 2016.

[80] Ngochao Tran Nobutaka Tetsuro Imai, Koshiro Kitao. Radio propagation for 5g. technical reports, docomo. `https://www.nttdocomo.co.jp/english/binary/pdf/corporate/technology/rd/technical_journal/bn/vol17_4/vol17_4_005en.pdf`, 2016.

[81] MIWEBA. D5 .1 channel modeling and characterization. `http://www.miweba.eu/wp-content/uploads/2014/07/MiWEBA_D5.1_v1.011.pdf`, jun 2014.

[82] Goktepe B Keusgen W Sakaguchi K. Peter M, Weiler RJ. Channel measurement and modeling for 5g urban microcellular scenarios. In Sensors, August 2016.

[83] R. J. Weiler, M. Peter, W. Keusgen, A. Kortke, and M. Wisotzki. Millimeter-wave channel sounding of outdoor ground reflections. In 2015 IEEE Radio and Wireless Symposium (RWS), pages 95–97, Jan 2015.

[84] W. Keusgen, R. J. Weiler, M. Peter, M. Wisotzki, and B. Goktepe. Propagation measurements and simulations for millimeter-wave mobile access in a busy urban environment. In 2014 39th International Conference on Infrared, Millimeter, and Terahertz waves (IRMMW-THz), pages 1–3, Sept 2014.

[85] Ieee standard for information technology–telecommunications and information exchange between systems–local and metropolitan area networks–specific requirements-part 11: Wireless lan medium access control (mac) and physical layer (phy) specifications amendment 3: Enhancements for very high throughput in the 60 ghz band. IEEE Std 802.11ad-2012 (Amendment to IEEE Std 802.11-2012, as amended by IEEE Std 802.11ae-2012 and IEEE Std 802.11aa-2012), pages 1–628, Dec 2012.

[86] A. Maltsev, R. Maslennikov, A. Sevastyanov, A. Lomayev, and A. Khoryaev. Statistical channel model for 60 ghz wlan systems in conference room environment. In Proceedings of the Fourth European Conference on Antennas and Propagation, pages 1–5, April 2010.

[87] S. Salous, V. Degli Esposti, F. Fuschini, R. S. Thomae, R. Mueller, D. Dupleich, K. Haneda, J. M. Molina Garcia-Pardo, J. Pascual Garcia, D. P. Gaillot, S. Hur, and M. Nekovee. Millimeter-wave propagation: Characterization and modeling toward fifth-generation systems. [wireless corner]. IEEE Antennas and Propagation Magazine, 58(6):115–127, Dec 2016.

[88] Shu Sun, George R. MacCartney Jr., and Theodore S. Rappaport. A novel millimeter-wave channel simulator and applications for 5g wireless communications. CoRR, abs/1703.08232, 2017.

[89] S. Sun, T. S. Rappaport, S. Rangan, T. A. Thomas, A. Ghosh, I. Z. Kovacs, I. Rodriguez, O. Koymen, A. Partyka, and J. Jarvelainen. Propagation path loss models for 5g urban micro- and macro-cellular scenarios. In 2016 IEEE 83rd Vehicular Technology Conference (VTC Spring), pages 1–6, May 2016.

[90] S. Sun, T. S. Rappaport, T. A. Thomas, A. Ghosh, H. C. Nguyen, I. Z. KovÃącs, I. Rodriguez, O. Koymen, and A. Partyka. Investigation of prediction accuracy, sensitivity, and parameter stability of large-scale propagation path loss models for 5g wireless communications. IEEE Transactions on Vehicular Technology, 65(5):2843–2860, May 2016.

[91] G. R. MacCartney, Junhong Zhang, Shuai Nie, and T. S. Rappaport. Path loss models for 5g millimeter wave propagation channels in urban microcells. In 2013 IEEE Global Communications Conference (GLOBECOM), pages 3948–3953, Dec 2013.

[92] G. R. Maccartney, T. S. Rappaport, M. K. Samimi, and S. Sun. Millimeter-wave omnidirectional path loss data for small cell 5g channel modeling. IEEE Access, 3:1573–1580, 2015.

[93] G. R. Maccartney, T. S. Rappaport, S. Sun, and S. Deng. Indoor office wideband millimeter-wave propagation measurements and channel models at 28 and 73 ghz for ultra-dense 5g wireless networks. IEEE Access, 3:2388–2424, 2015.

[94] T. A. Thomas, M. Rybakowski, S. Sun, T. S. Rappaport, H. Nguyen, I. Z. Kovacs, and I. Rodriguez. A prediction study of path loss models from 2-73.5 ghz in an urban-macro environment. In 2016 IEEE 83rd Vehicular Technology Conference (VTC Spring), pages 1–5, May 2016.

[95] S. Jaeckel, L. Raschkowski, K. Borner, and L. Thiele. Quadriga: A 3-d multi-cell channel model with time evolution for enabling virtual field trials. IEEE Transactions on Antennas and Propagation, 62(6):3242–3256, June 2014.

[96] K. Haneda, M. Peter, J. Medbo, M. Beach, R. d'Errico, S. Wu, and J. M. Conrat. Radio channel sounding campaigns in eu h2020 mmmagic project for 5g channel modeling. In 2016 International Symposium on Antennas and Propagation (ISAP), pages 596–597, Oct 2016.

[97] Sophocles J. Orfanidis. Wireless Communications, 2nd Edition, Wiley. 2011.

[98] A. Bamba, F. Mani, and R. D'Errico. E-band millimeter wave indoor channel characterization. In 2016 IEEE 27th Annual International Symposium on Personal, Indoor, and Mobile Radio Communications (PIMRC), pages 1–6, Sept 2016.

[99] K. Haneda, J. Zhang, L. Tan, G. Liu, Y. Zheng, H. Asplund, J. Li, Y. Wang, D. Steer, C. Li, T. Balercia, S. Lee, Y. Kim, A. Ghosh, T. Thomas, T. Nakamura, Y. Kakishima, T. Imai, H. Papadopoulos, T. S. Rappaport, G. R. MacCartney, M. K. Samimi, S. Sun, O. Koymen, S. Hur, J. Park, C. Zhang, E. Mellios, A. F. Molisch, S. S. Ghassamzadeh, and A. Ghosh. 5g 3gpp-like channel models for outdoor urban microcellular and macrocellular environments. In 2016 IEEE 83rd Vehicular Technology Conference (VTC Spring), pages 1–7, May 2016.

[100] A. Karttunen, J. Jarvelainen, A. Khatun, and K. Haneda. Radio propagation measurements and winner ii parameterization for a shopping mall at 60 ghz. In 2015 IEEE 81st Vehicular Technology Conference (VTC Spring), pages 1–5, May 2015.

[101] J. Ko, K. Lee, Y. J. Cho, S. Oh, S. Hur, N. G. Kang, J. Park, D. J. Park, and D. H. Cho. A feasibility study and spatial-temporal characteristics analysis for 28 ghz outdoor wireless channel modelling. IET Communications, 10(17):2352–2362, 2016.

[102] K. Haneda, S. L. H. Nguyen, J. Jarvelainen, and J. Putkonen. Estimating the omni-directional pathloss from directional channel sounding. In 2016 10th European Conference on Antennas and Propagation (EuCAP), pages 1–5, April 2016.

[103] Andrea Goldsmith and AnaÃŕs Nin. Wireless communications, 2005.

[104] RSPG. Studies on frequency - related matters for international mobile telecommunications identification including possible additional allocations to the mobile services on a primary basis in portion(s) of the frequency range between 24.25 and 86 ghz for the future development of international mobile telecommunications for 2020 and beyond. `http://rspg-spectrum.eu/2016/06/`, jun 2016.

[105] FCC. Federal communications commission washington, d.c. 20554. `https://apps.fcc.gov/edocs_public/attachmatch/FCC-15-138A1.pdf`, jun 2016.

[106] GSMA. Korea views on 5g spectrum. `http://www.gsma.com/spectrum/wp-content/uploads/2016/08/MSIP_Korean-views-on-5G-spectrum_Kyungmee_160621.pdf`, jun 2016.

[107] T. S. Rappaport, E. Ben-Dor, J. N. Murdock, and Y. Qiao. 38 ghz and 60 ghz angle-dependent propagation for cellular amp; peer-to-peer wireless communications. In 2012 IEEE International Conference on Communications (ICC), pages 4568–4573, June 2012.

[108] Z. Zhong, X. Wu, J. Qu, and X. Yin. Mimo channel measurement and characterization for 26ghz wave in outdoor scenarios. In 2016 IEEE 83rd Vehicular Technology Conference (VTC Spring), pages 1–5, May 2016.

[109] Q. Wang, S. Li, X. Zhao, M. Wang, and S. Sun. Wideband millimeter-wave channel characterization based on los measurements in an open office at 26ghz. In 2016 IEEE 83rd Vehicular Technology Conference (VTC Spring), pages 1–5, May 2016.

[110] M. R. Akdeniz, Y. Liu, M. K. Samimi, S. Sun, S. Rangan, T. S. Rappaport, and E. Erkip. Millimeter wave channel modeling and cellular capacity evaluation. IEEE Journal on Selected Areas in Communications, 32(6):1164–1179, June 2014.

[111] X. Zhao, S. Li, Q. Wang, M. Wang, S. Sun, and W. Hong. Channel measurements, modeling, simulation and validation at 32 ghz in outdoor microcells for 5g radio systems. IEEE Access, 5:1062–1072, 2017.

[112] B. Uguen, N. Amiot, and M. Laaraiedh. Exploiting the graph description of indoor layout for ray persistency modeling in moving channel. In 2012 6th European Conference on Antennas and Propagation (EUCAP), pages 30–34, March 2012.

[113] Nicolas AMIOT. Design of a Simulation Platform Joining Site Specific Radio Propagation and Human Mobility for Localization Applications. PhD thesis, University of Rennes1, dec 2013.

[114] OpenStreetMap contributors. Planet dump retrieved from https://planet.osm.org . `https://www.openstreetmap.org`, 2017.

[115] Sophocles J. Orfanidis. Electromagnetic Waves and Antennas. 2002.

[116] R. G. Kouyoumjian and P. H. Pathak. A uniform geometrical theory of diffraction for an edge in a perfectly conducting surface. Proceedings of the IEEE, 62(11):1448–1461, Nov 1974.

[117] Constantine A. Balanis. Antenna Theory: Analysis and Design, third edition. Wiley-, 1982.

Résumé en Français

Contexte

Dans le domaine des communications radio mobiles, les performances d'un système de communication sont très dépendantes du canal de transmission qui est composé du canal de propagation et des antennes. Le canal de propagation est un objet régit par les lois de l'électromagnétisme incorporant naturellement des personnes, immeubles, voitures, arbres, mobiliers et autres objets. Les antennes sont des entitées physiques rayonnantes qui convertissent les champs électromagnétiques en signaux exploitables pour la communication et par lesquelles le canal de propagation est vu. Une connaissance du canal de transmission dans ses diverses dimensions est très importante pour la modélisation des systèmes ainsi que l'évaluation de leurs performances. Dans la perspective du développement de la future génération radio cellulaire connue sous l'acronyme 5G, des débits de l'ordre du gigabit par secondes sont visés avec des liaisons fiables et des communications avec des latences très réduites comparées aux systèmes actuellement déployés comme par exemple la 3G ou la 4G. De plus, des applications telles que les voitures autonomes, la réalité virtuelle et la réalité augmentée qui requièrent des débits significatives avec une exigence accrue en temps de latences sont attendues par la 5G. En outre, les enjeux de la 5G ne se limitent pas seulement à une augmentation du débit du point de vue utilisateur mais va bien au delà de ces enjeux primaires avec une volonté de proposer une infrastructure hétérogène pouvant satisfaire les nouveaux besoins liés à la communication des objets dite connectés (IoT) apparus récemment, augmentant ainsi considérablement le trafic des données.
Ces forts enjeux attendus ne peuvent être satisfaites par les systèmes actuellement déployés tel que la 4G par exemple. Une des solutions pour atteindre des transmission hauts débits est d'explorer les bandes de fréquences dites millimétriques (fréquence allant de 30 GHz à 300 GHz). L'emploi des bandes millimétriques à l'avantage d'une part de faire face à une saturation du spectre de fréquence que connaissent les bandes en dessous de 6 GHz et d'autre part de pouvoir offrir des bandes passantes qui sont de l'ordre du GHz et dont certaines sont disponibles sans licence payante.

Les ondes millimétriques ont longtemps été utilisées dans des applications de type satellites, radar automobiles, imagerie, entre autre mais une utilisation des ces ondes dans le domaine des communications cellulaires du point de vue du lien d'accès en est à ses prémices. La notion de couverture et de dimensionnement du réseau cellulaire sont importantes dans un contexte de déploiement cellulaire et sont intrinsèquement liés au canal de propagation qui atténuent fortement le signal évoluant dans ces bandes de fréquences due à la petite taille de la longueur d'onde. D'autre part, l'utilisation des composantes électroniques fonctionnant dans les bandes millimétriques reste très gourmande en énergie et très couteuse. Cependant, cette précédente vision n'inclue pas les récentes avancées majeures dans le domaine de l'électronique avec une maturité

des technologies CMOS caractérisée par des composants à bas coût et consommant peu d'énergie. Par ailleurs, les fortes pertes dont souffrent les ondes millimétriques peuvent être en partie compensées par l'utilisation d'antennes directives. De plus les bandes en dessous de 6 GHz font face à une saturation du spectre (qui rappelons le est une ressource rare et règlementée) due principalement au déploiement de différents systèmes dans ces bandes (cellulaires, WiFi par exemple). Tout cela fait qu'aujourd'hui les différents acteurs incluant opérateurs, industriels et académiciens à se tourner vers les bandes millimétrique pour le déploiement de la 5G en accès radio. Cependant, l'exploration de nouvelles bandes de fréquences nécessite d'avoir des modèles de canaux de propagation qui soient compatibles avec ces bandes et pouvant satisfaire aux exigences des pré-requis de la 5G. En outre, les principaux modèles de canaux de propagation existants n'adressent pas de façon satisfaisantes toutes les contraintes introduites par le futur emploi des bandes millimétriques en accès radio. L'étude des propriétés du canal de propagation étant une première étape fondamentale pour la proposition des modèles de canaux de propagation, un réel intérêt scientifique réside donc dans la compréhension et la caractérisation des propriétés du canal de propagation en bande millimétriques.

Travaux réalisés

Les travaux réalisés durant ces trois années de thèse visent à s'intégrer dans le développement des canaux de propagation en bandes millimétriques et s'articulent principalement autour de la caractérisation du canal de propagation ainsi que la validation d'un simulateur de canaux radio adapté aux bandes millimétriques. Afin d'apporter des éléments de réponses relatifs aux objectifs sus-mentionnés, nous avons dans cette thèse :

- Contribué à l'étude de la propagation des canaux radioélectriques dans les bandes centimétriques et millimétriques. Cette étude réalisée à l'aide de techniques de sondage par canaux radio couvre un large éventail de scénarios de propagation représentatifs (campus universitaire, bureau, bibliothèque, urbain micro-cell)
- Etudié la variabilité du canal en bande millimétriques ainsi que l'impact des diffuseurs qui se trouvent dans le canal de propagation en milieu urbain. Ce dernier aspect a été rendu possible grâce à une méthode proposée dans cette thèse et dénommée `back-prjection` qui permet de rendre visible les effets des diffuseurs en milieu urbain
- Amélioré et calibré l'outil de simulation développé au sein de notre laboratoire. L'outil de simulation dénommé PyLayers est un outil de tracé de rayons (RT) basé sur un modèle de graphes. Les données de mesures obtenues à partir des campagnes de mesures ont été utilisées comme référence pour le paramétrage de l'outil RT.

Campagnes de mesures: motivations

Le sondage de canal est un procédé par lequel un équipement, composé d'un émetteur et d'un récepteur, est déployé dans un environnement donné afin de capturer les effets

physiques importants émanant du canal de propagation. Il reste l'une des techniques les plus fiables pour comprendre l'impact de l'environnement sur la qualité du signal. D'autre part, cette technique sert de base de comparaison pour de calibrer des outils de simulations déterministes mais aussi pour proposer des modèles de canaux de propagation. Les principales motivations scientifiques qui nous ont menés à conduire ces campagnes de mesures sont résumées ci-dessous :

- L'étude de la variabilité temporelle du canal radio dans les bandes millimétriques. L'aspect de la mobilité a été adressé lors des campagnes de mesures en plaçant l'antenne de réception dans une position fixe tandis que l'antenne d'émission se déplaçait le long d'une trajectoire. Une antenne cornet et une antenne omni-directionelle toutes deux conçues en polarisation verticale ont été utilisées respectivement au niveau du récepteur et l'émetteur.

- L'évaluation des performances de l'outil de ray tracing à travers différentes bandes de fréquences et différents scénarios en conditions de LOS. Ces mesures ont été effectuées dans une configuration où l'émetteur et le récepteur étaient dans une position fixe. Le récepteur, doté d'une antenne cornet conçue en polarisation verticale, a été pivoté dans le plan azimutal tandis qu'une antenne omni-directionnelle, conçue aussi en polarisation verticale, a été utilisée au niveau de l'émetteur.

Campagnes de mesures: sondage de canaux

Quatre campagnes de mesures, effectuées dans différents scénarios représentatifs, ont été menées dans différentes bandes de fréquence identifiées par l'union internationale des télécommunications comme étant des potentiels candidats au déploiement des ondes millimétriques dans la 5G. Ci-dessous, le résumé de ces campagnes de mesures :

- $Meas.0$ est une campagne réalisée dans un environnement de type campus universitaire et $Meas.1$ une campagne réalisée dans un environnement de types bureau et bibliothèque. Ceux sont des mesures en situation de mobilité légère mais réelle (non synthétique) effectuées à 28 GHz. L'antenne réceptrice et émettrice ont été fixée à une hauteur de $1,82$ m. Le scénario de mobilité étant considéré, l'antenne émettrice se déplaçait le long de plusieurs routes couvrant des situations de LOS, OLOS et NLOS. Les données acquises dans de telles configurations sont analysées et soumises aux analyses statistiques usuelles pour ce type de canaux.

- $Meas.2$ est une campagne de mesures intensives effectuées dans trois bandes de fréquences : 15, 28 et 83 GHz. Une antenne cornet, utilisée au niveau du récepteur, a été pivotée sur l'intégralité du plan azimutal tandis qu'une antenne omni-dirrectionelle a été utilisée à l'émission. Ces mesures en multi-fréquences ont été effectuées dans un environnement type salle de conférence et au total 60 liens ont été mesurés dans les trois bandes de fréquences. La disposition des points de mesures permet d'envisager une étude ultérieure sur la mobilité indoor selon une route synthétisée.

- $Meas.3$ est une campagne de mesure réalisée à 32.6 GHz en environnement typique urbain ouvert incluant immeubles, bâtiments, voitures, mobilier urbain (lampadaires, panneaux de signalisation, panneaux de pubicités) etc... La méthodologie de mesure est la même que celle utilisée pour la campagne $Meas.2$. L'antenne réceptrice a été placée à une hauteur de 6 m grâce à une nacelle et couvrant une sectorisation en demi-plan tandis que l'antenne émettrice a été placée à hauteur de hauteur de $1,65$ m représentant le niveau piéton. Ce scénario adressé reste identique à une situation de déploiement réel. Au total, 16 liens dont 13 en LOS et 3 en NLOS situations avec des distances de liaison allant de 15 m à 80 m ont été mesurés.

Pour chaque bande de fréquence, un sondeur de canal utilisant une méthode fréquentielle différente a été utilisé. Pour chaque soundeur, il y'avait d'une part un émetteur constitué d'une antenne omni-directionnelle et relié à un analyseur de réseau via un cable optique permettant de diminuer les fortes pertes liées à la montée en fréquence. D'autre part, il y'avait le récepteur qui était constitué d'une antenne cornet directive. En fonction des objectives de mesures, l'antenne cornet pouvait être monter sur un système de rotation qui permet de capturer le canal de propagation dans toute sa dimension azimutale. Des up- et down-converts ont été utilisés pour tous les sondeurs de canaux à l'exception du sondeur de canal à 15 GHz afin de pouvoir adresser les hautes bandes de fréquences à l'aide d'un multiplieur de fréquence.

Analyse de données : $Meas.0$

L'analyse des données obtenues en $Meas.0$ a montré que les mesures en mobilité effectuées au niveau du campus n'étaient pas exploitables due à une erreur de mesure. La source d'erreur a été attribuée à un problème de serrage au niveau des connecteurs du up-converteur créant ainsi qu'un effet de rebonds. Ces mesures outdoor réalisées en mobilité avec un secteur angulaire selectif illustrent pourtant assez fidèlement le type de canaux qui sera rencontré en pratique dans la 5G avec les systèmes de focalisation sélective sur les utilisateurs ou on aura vraisemblement quelques trajets forts avec un très longue cohérence spatiale autorisant le tracking et la communication haut débit à faible latence. Ce type de mesure devra être reproduit avec des situations de blocage par véhicules et des piétons.

Analyse de données : $Meas.1$

L'analyse des données de mesures obtenues en $Meas.1$ a montrée la cohérence spatiale du canal de propagation à 28 GHz dans les environnements bureau et bibliothèque. La variation des multi-trajets a été observée comme étant spatialement cohérente et principalement obtenues par multiple réflexions à travers les parois des murs. En outre, ces mesures ont permis de mettre en évidence la prédominance de l'effet de réverbération dans l'environnement type bureau par rapport à l'environnement type bibliothèque. De

plus, l'analyse de la corrélation entre les paramètres à grande échelles (LSP) a montrée une dépendance entre les LSPs.

Analyse de données : $Meas.2$

L'analyse des données de mesures obtenue lors des campagnes de mesures effectués en multi-fréquence a permis de voir que la structure du canal est conservée avec la montée en haute fréquence.

Analyse de données : $Meas.3$

Le traitement des données mesurées en environnement urbain a montré que le canal de propagation $32,6$ GHz presente que quelques contributions de trajets importantes. D'autre part, nous avons proposé une méthode qui permet de mettre en évidence l'effet des diffuseurs se trouvant dans le canal de propagation. Cette méthode assumant une simple réflexion sur un diffuseur établit un mapping entre un trajet (caractérisé par un retard, une angle et une amplitude) et la carte de l'environnement de mesure. Elle permet de trouver la position des diffuseurs qui refléchiraient de l'énergie via une simple réflexion. L'application de cette méthode sur les données de mesures a permis d'identifier les sources principales de rétrodiffusion de l'énergie sur l'environnement UMi et il a été observé que les facade d'immeubles, fenêtres d'immeubles et les mobiliers urbain (panneaux de publicité, panneaux de signalisation et lampadaires) délivrent une grande partie de l'énergie par mécanismes de réflexion spéculaire.

Simulateur de propagation déterministe

Un simulateur de propagation déterministe est un outil de simulation basé sur la description de l'environnement et permet de reproduire les réalités du canal de propagation. Concrètement, ce genre d'outil peut permettre par exemple à un opérateur téléphonique de pouvoir prédire la couverture radio de son réseau tout en tenant compte de la réalité des environnements. Le simulateur utilisé dans cette thèse est un simulateur déterministe basé sur le ray tracing (RT) et développé à l'IETR. C'est un outil open source conçu sous le language Python et basé sur une structure originale à base de structure de graphes réduisant la complexité de la recheche des rayons. Il est montré dans ce travail que ce simulateur permet la reproduction réaliste des principaux canaux mesurés. Les antennes utilisées lors des campagnes de mesures ont été implémentées pour l'occasion ainsi que la modélisation des environnements.

RT vs Mesures

Les données de mesures obtenues en $Meas.2$ et $Meas.3$ sont utilisées en guise de comparaison avec le RT et les résultats de comparaisons sont résumés ci-dessous :

- Pour l'environnement type salle de conférence, les résultats de comparaisons des liens en situation de LOS ont démontré que le RT était capable de prédire les trajets

significatives dans les trois bandes de fréquences. De plus, le profile angulaire de puissance et le profile de retard de puissance ont été choisis comme métrique de comparaison et un niveau d'accord acceptable a été obtenu.

- Pour l'environnement urbain, le RT était en mesure de prédire le canal urbain à $32,6$ GHz en situation de LOS avec un niveau d'accord acceptable. En outre, des comparaisons en termes de profile angulaire et retard de puissance et de profile angulaire de puissance ont été effectuées et une certaine adéquation entre la mesure et la simlation a été observée. De plus, une étude en termes de LSPs entre la mesure et la prédiction a été fournie et un accord assez satisfaisant a été noté.

Conclusion

Cette thèse a apportée une contribution au défi de la caractérisation des canaux radios en bandes millimétriques ainsi que la validation d'un outil de simulation déterministe à travers un grand nombre de campagnes de mesures réalisées dans différents scénarios représentatives. Des questions de recherche liées à la caractérisation des canaux radio en bandes millimétriques et sa prédiction à travers un outil de simulation déterministe ont été abordées. Les principales motivations scientifiques étaient d'étudier la variabilité dans le temps et l'effet de l'environnement sur le canal de propagation dans les bandes millimétriques. Les bandes de fréquences adressées ici sont identifiées comme étant importantes par l'UIT. L'exploitation des résultats de mesures ont permis d'apporter des éléments de réponses concernant le canal de propagation en bande millimétrique. Le simulateur de canal déterministe utilisé dans cette thèse incorpore les mécanismes de propagation tels que la transmission, la réflexion spéculaire et la diffraction. Le RT a permis de prédire le canal de propagation dans les bandes millimétriques avec une concordance acceptable vis à vis des données de mesures. Ces résultats démontrent que le canal de propagation en bandes millimétriques a pour avantage d'être prédit avec de simple outil deterministe.

Cependant, le travail proposé dans cette thèse ne fait qu'effleurer toutes les informations utiles qui peuvent être extraites de ces données. Des questions subsistent et ci-dessous quelques recommandations pour d'autres études :

- Continuer à exploiter les données de mesure présentées dans cette thèse, en particulier sur la nature et l'intensité des diffuseurs
- Du point de vue du RT, la prochaine étape pourrait être d'introduire l'aspect de la mobilité ainsi que l'effet de blocage qui reste un effet très important surtout si on considère des algorithmes de tracking de l'utilisateur
- La mesure en UMi qui a été faite suggère que des surfaces relativement petites peuvent apporter beaucoup d'énergie au récepteur avec presque sans atténuation. Le scénario UMi doit être reproduit le long d'un itinéraire afin de capturer la durée de ces forts trajets réfléchis par ces surfaces

- Améliorer et étendre l'outil RT. Pour la situation indoor, il serait intéressant d'incorporer l'effet de la réverbération dans l'outil RT vu que l'outil à la base a été conçue pour supporter ce phénomène. En outre, il serait utile d'utiliser l'outil de RT pour étudier la cohérence spatiale du canal des les bandes millimétriques.

List of Figures

2.1. Specific attenuation due to atmospheric gases from ITU-R P.676-11. . . . 8
2.2. Illustration of the transmission mechanism at the plane surface assuming a single interface. . . . 9
2.3. Illustration of the specular reflection mechanism appearing on a single interface. . . . 10
2.4. Example of a diffraction mechanism over a wedge. . . . 10
2.5. METIS KED blockage model: blockage due to the shadowing effect. . . . 11
2.6. 2D view of the diffuse scattering mechanism illustration appearing over a rough surface. . . . 12

3.1. Mm-wave frequencies identified at by the ITU at the WRC-15. . . . 32
3.2. Block diagram of the mm-wave wideband Aalto's channel sounder (at 28 GHz). . . . 34
3.3. Map of the measurement environment *Meas*.0. Bikes, trees, bushes, and lamp-posts were present in the measurement site but are not represented in the map. . . . 35
3.4. Illustration of the measurement error (*Meas*.0): example of CIR obtained by applying the inverse Fourier transform ($\mathcal{F}^{-1}$) to the of *Meas*.0. . . . 36
3.5. Layouts of the InH environments: On the left (a) the normal office (I1) and the library (I2) on the right (b). . . . 38
3.6. Photos of the measurement site: the normal office in (a) and the library in (b). . . . 38
3.7. Dynamic radio channel of I1-R11 (a) and I1-R12 (b). . . . 39
3.8. Dynamic radio channel of I2-R21, I2-R22, I2-R23 and I2-R24. . . . 40
3.9. Pictures of the biconical and the horn antennas used in *Meas*.2. . . . 44
3.10. Layout map of the conference room. . . . 45
3.11. Photos of the conference room measurement site. . . . 46
3.12. Example of PDPs derived for the links BS-MS1 and BS-MS7. . . . 46
3.13. Evolution of the PDP over the trajectory. . . . 47

3.14. Evolution of the PAP over the trajectory. 48
3.15. Map of the UMi obtained from Open Street Map building (https://osmbuildings.org). Cars, pedestrians, trees, pillars and lamp-posts are not presented here. The blue circles and red squares are MS positions. 49
3.16. Photos of the measurement site of the UMi. In (a), the position of the BS antenna mounted on the lift at a height of 6 m above the ground and located near the building R made mostly by cement block with a rough surface and windows glass. (a), (b) and (c) shows the overview of the investigated measurement. Some positions of the MS antennas are illustrated with the parking area, lamp-posts, road-signs, cars, people, trees, bushes. Building A is made essentially with tiles, while building B is constituted by rough wall and windows glasses are shown in (d). 51
3.17. Illustration of the fine peak search detection applied to the link BS-MS9. The detected peaks are in red dots 52
3.18. Illustration of the sparsity of the 32 GHz: the all LOS links are plotted. . 52
3.19. `back-projection`: single bounce assumption. 53
3.20. `back-projection` applied to link BS-MS10 55
3.21. `back-projection` applied to link BS-MS3 56

4.1. Illustration of $\mathscr{G}_s$ (upper left corner), Diffraction points in outdoor (upper right figure), $\mathscr{G}_t$ (lower left figure) red lines are connection between `convex cycles`, $\mathscr{G}_v$ (lower right figure) encoding visibility between points and segments 62
4.2. Illustration of $\mathscr{G}_i$ from [113]. 63
4.3. Illustration of the γ_{RT}'s determination in the RT tool. The apex of the cone is constructed between the first `segment` (S_1) and the $N-1^{th}$-`segment` (S_{N-1}). 64
4.4. Reflected and transmitted coefficients evaluated by PyLayers at 32.6 GHz. 66
4.5. RT implementation illustration of the diffraction over a metal provided by the RT evaluated at 2.4 and 32.6 GHz. 67
4.6. Illustration of the radiation pattern of the horn antenna implemented in PyLayers. The blue line denotes the azimuth plane while the black line represents the elevation plane. 69
4.7. Azimuth and elevation plane measured at 27.5 GHz by the manufacturer. 69
4.8. Example of the RT simulation performed in InH at 2.4 GHz. Two omni-directional antennas were used. 71
4.9. Screen-shots of the RT performed in the conference room. Only the LOS and the SR mechanisms are turned on. 73
4.10. Comparison between the measured and simulated PADP and PAP of the link BS-MS7 at 15 GHz. 74
4.11. Comparison between the measured and simulated PADP and PAP of the link BS-MS7 at 28 GHz. 75

4.12. Comparison between the measured and simulated PADP and PAP of link BS-MS7 at 83 GHz. 76
4.13. Comparison between the measured and simulated PADP and PAP of the link BS-MS1 at 15 GHz. 77
4.14. Multi-frequency InH comparison between the measured and simulated PADP and PAP of the link BS-MS1 at 28 GHz. 78
4.15. Multi-frequency InH comparison between the measured and simulated PADP and PAP of the link BS-MS1 at 83 GHz. 79
4.16. Screen-shots of the RT performed for the link BS-MS3. 81
4.17. UMi: Comparison between the measured and simulated PADP, PDP and PAP of the link BS-MS3. 82
4.18. UMi: Comparison between the measured and simulated PADP, PDP and PAP of the link BS-MS10. 83
4.19. Histogram of the combined antennas gain obtained from the FSPL and the LOS peak. 84
4.20. UMi: LSPs comparison. 86

A.1. 32.6 GHz UMi Espoo: BS-MS 1 - PDP (left) PADP (middle) PAP (bottom) for measurement (left) and RT simulation (right) 96
A.2. 32.6 GHz UMi Espoo: BS-MS 2 PDP (left) PADP (middle) PAP (bottom) for measurement (left) and RT simulation (right) 97
A.3. 32.6 GHz UMi Espoo: BS-MS 3 PDP (left) PADP (middle) PAP (bottom) for measurement (left) and RT simulation (right) 98
A.4. 32.6 GHz UMi Espoo: BS-MS 4 PDP (left) PADP (middle) PAP (bottom) for measurement (left) and RT simulation (right) 99
A.5. 32.6 GHz UMi Espoo: BS-MS 5 PDP (left) PADP (middle) PAP (bottom) for measurement (left) and RT simulation (right) 100
A.6. 32.6 GHz UMi Espoo: BS-MS 6 PDP (left) PADP (middle) PAP (bottom) for measurement (left) and RT simulation (right) 101
A.7. 32.6 GHz UMi Espoo: BS-MS 7 PDP (left) PADP (middle) PAP (bottom) for measurement (left) and RT simulation (right) 102
A.8. 32.6 GHz UMi Espoo: BS-MS 8 PDP (left) PADP (middle) PAP (bottom) for measurement (left) and RT simulation (right) 103
A.9. 32.6 GHz UMi Espoo: BS-MS 9 PDP (left) PADP (middle) PAP (bottom) for measurement (left) and RT simulation (right) 104
A.10. 32.6 GHz UMi Espoo: BS-MS 10 PDP (left) PADP (middle) PAP (bottom) for measurement (left) and RT simulation (right) 105
A.11. 32.6 GHz UMi Espoo: BS-MS 11 PDP (left) PADP (middle) PAP (bottom) for measurement (left) and RT simulation (right) 106
A.12. 32.6 GHz UMi Espoo: BS-MS 12 PDP (left) PADP (middle) PAP (bottom) for measurement (left) and RT simulation (right) 107
A.13. 32.6 GHz UMi Espoo: BS-MS 13 PDP (left) PADP (middle) PAP (bottom) for measurement (left) and RT simulation (right) 108

B.1. 32.6 GHz UMi Espoo: path `back-projection` applied to the link BS-MS 1. Some metallic road-signs were located near the MS1 position as it can be seen in Fig. 3.16.b and stated in Table 3.7. 111
B.2. 32.6 GHz UMi Espoo: path `back-projection` applied to the link BS-MS 2. Notice that one lamp-post was located near the BS while another one was located near MS 2. 112
B.3. 32.6 GHz UMi Espoo: path `back-projection` applied to the link BS-MS 4. As seen in (a), the MS was surrounded by cars, lamp-posts, bushes, road-signs. 113
B.4. 32.6 GHz UMi Espoo: path `back-projection` applied to the link BS-MS 5. Road-signs and lamp-posts were located near the MS as illustrated in (a). 114
B.5. 32.6 GHz UMi Espoo: path `back-projection` applied to the link BS-MS 6 115
B.6. 32.6 GHz UMi Espoo: path `back-projection` applied to the link BS-MS 7 116
B.7. 32.6 GHz UMi Espoo: path `back-projection` applied to the link BS-MS 8 117
B.8. 32.6 GHz UMi Espoo: path `back-projection` applied to the link BS-MS 9 (b) and the associated photo of the MS location (a). 118
B.9. 32.6 GHz UMi Espoo: path `back-projection` applied to the link BS-MS 11 (b) and the associated photo of the MS location (a). 119
B.10. 32.6 GHz UMi Espoo: path `back-projection` applied to the link BS-MS 12. As shown in (a), some bushes, cars and lamp-posts were near the MS location. 120
B.11. 32.6 GHz UMi Espoo: path `back-projection` applied to the link BS-MS13. The photo in (a) shows the presence of some road-signs and other metallic objects. 121

List of Tables

2.1. Literature survey of mm-wave measurement campaigns addressing PMs studies (transmission (Trans.), specular reflection (SR), diffraction (Diff.) and diffuse scattering (Scat.)). 13

3.1. Overview of the measurement campaigns. 31
3.2. Parameter settings of the channel sounder used in $Meas.0$ 35
3.3. Parameter settings of the 28 GHz channel sounding used in $Meas.1$ 37
3.4. Characteristic of the investigated routes of $Meas.1$. 37
3.5. Summary of the LSPs comparison obtained from I1-R11 and I2-R21 at $f_c = 28.5$ GHz against those reported in the 3GPP channel model [15] applicable into mm-wave radio frequencies and covering the LOS InH office. 41
3.6. Summary of the parameter settings of the mm-wave synthetized omni-directional channel sounders. 43
3.7. Rough description of the MS location in LOS configurations in $Meas.3$. . 50

4.1. Horn dimensions 68
4.2. Considered material properties of the conference room environment in the RT at the three frequency bands. 72
4.3. Considered material properties of the UMi environment in the RT simulator. 80
4.4. Paths prediction from the RT w.r.t the PADP. 83
4.5. Summary of the UMi LSPs comparison between at $f_c = 32.6$ GHz. 87